

**Transverse structure of hadrons from Lattice
QCD using Large-Momentum Effective
Theory**



Dissertation

zur Erlangung des Doktorgrades
der Naturwissenschaften (Dr. rer. nat.)
der Fakultät für Physik
der Universität Regensburg

vorgelegt von

Lisa Walter

aus

Schweinfurt

im Jahr 2024

Promotionsgesuch eingereicht am: 22.10.2024

Die Arbeit wurde angeleitet von: Prof. Dr. Andreas Schäfer

Abstract

Parton distribution functions (PDFs) and transverse momentum dependent parton distribution functions (TMDPDFs) contain information about the internal structure of hadrons and are important for describing high-energy scattering processes. The first Mellin moments of these functions are routinely extracted by combining lattice gauge theory and operator product expansion, while the large-momentum effective theory (LaMET) allows to calculate their full functional form in certain kinematic regions which can also be specified using LaMET. As the formulation of LaMET was a rather recent one, many of its properties and applications still have to be worked out more precisely. To this we contribute using CLS gauge ensembles.

A quark transversity PDF describes the correlation between the transverse polarizations of a hadron and its quark constituents of specific flavor and is barely constrained from experiments due to its chiral-odd nature. In this work, the isovector quark transversity PDF of the proton is calculated for various lattice spacings and pion masses, using proton momenta up to 2.8 GeV. The result is non-perturbatively renormalized in the hybrid scheme and a controlled extrapolation to the continuum and physical pion mass, as well as to infinite momentum, is performed. The final result agrees well with global analyses.

As one of eight leading twist TMDPDFs, the quark Boer-Mulders function describes the coupling between quark spin and quark angular momentum. Therefore, this barely known function is present also for an unpolarized hadron such as the pion. This thesis shows an exploratory study of the quark Boer-Mulders function of the pion, using three different lattice spacings and pion momenta up to 1.84 GeV. Non-perturbative renormalization is performed in the short distance ratio scheme, and the dependence on the impact parameter b_{\perp} is fitted in order to compare the result across different ensembles. A combined extrapolation to infinite momentum and to the continuum is performed for various values of b_{\perp} . It is found that the Boer-Mulders function becomes too small to be determined at $b_{\perp} \approx 0.4 - 0.5\text{fm}$.

Contents

1	Introduction	1
2	Quantum Chromodynamics on the lattice	5
2.1	QCD in the continuum	5
2.2	Concepts of QCD on the lattice	7
2.2.1	Formulation of fermions and gluons on the lattice	8
2.2.2	Discretized version of the QCD action	8
2.2.3	Generation of ensembles with Monte Carlo simulations	11
2.3	Methods in lattice QCD measurements and analysis	13
2.3.1	Propagator calculation	13
2.3.2	Smearing techniques	15
2.3.3	Error estimation	16
2.3.4	Fitting	19
2.4	Gauge ensembles generated by the Coordinated Lattice Simulations effort	20
3	Parton physics using Large-Momentum Effective Theory	21
3.1	Parton distribution function in the continuum	21
3.2	Large-Momentum Effective Theory	24
3.3	Parton distribution function on the lattice using LaMET	24
3.3.1	Validity of the factorization formula	27
3.3.2	Renormalization of quasi-PDFs in the hybrid scheme	28
3.3.3	One-loop matching kernel in the hybrid scheme	30
3.4	Transverse momentum dependent parton distribution function in the continuum	31
3.4.1	Definition of TMDPDFs	31
3.4.2	Rapidity divergence	32
3.4.3	Decomposition of the TMD correlator in terms of TMD-PDFs	35
3.4.4	Previous TMDPDF determinations	37

3.5	Transverse momentum dependent parton distribution function on the lattice using LaMET	38
3.5.1	Definition of quasi-TMDPDFs	38
3.5.2	Renormalization of quasi-TMDPDFs in the short distance ratio scheme	39
3.5.3	Momentum evolution equation for quasi-TMDPDFs	42
3.5.4	Off-light-cone soft function	43
3.5.5	Matching of quasi-TMDPDF to light-cone TMDPDF	44
4	LaMET calculations for the isovector quark transversity PDF of the nucleon	45
4.1	Gauge ensembles and setup	45
4.2	Correlation functions	46
4.2.1	Two-point correlation function	46
4.2.2	Three-point correlation function	50
4.3	Extraction of the ground state matrix element	54
4.4	Nucleon isovector tensor charge	56
4.5	Renormalization in the hybrid scheme	57
4.6	Extrapolation for large quasi-LF distances	62
4.7	Light-cone proton isovector quark transversity distribution	64
4.7.1	Dependence on momentum, pion mass and lattice spacing	64
4.7.2	Combined infinite momentum, physical pion mass and continuum extrapolation	66
4.7.3	Final result and comparison with JAM	67
5	LaMET calculations for the isovector quark Boer-Mulders function of the pion	71
5.1	Gauge ensembles and setup	71
5.2	Correlation functions	72
5.2.1	Two-point correlation function	73
5.2.2	Three-point correlation function	78
5.3	Extraction of the ground state matrix element	80
5.4	Renormalization in the short distance ratio scheme	85
5.4.1	Fit of the rectangular Wilson loop	86
5.4.2	Dependence of the subtracted quasi-TMDPDF on L	86
5.4.3	Calculation of renormalization factors	88
5.5	Extrapolation for large quasi-LF distances	90
5.6	Fourier transformation to momentum space	92
5.7	Light-cone quark Boer-Mulders function of the pion	93
5.7.1	Reduced soft function and Collins-Soper kernel	93
5.7.2	Results before and after matching to the light-cone	95

5.7.3	Momentum dependence	95
5.7.4	Estimation of systematic uncertainties	99
5.7.5	Fit of the b_{\perp} -dependence	100
5.7.6	Lattice spacing dependence	103
5.7.7	Combined infinite momentum and continuum extrapolation	103
6	Conclusion and Outlook	109
	References	113
	Acknowledgements	125

Chapter 1

Introduction

The universe as it is visible to us consists of atoms, whose cores are made from protons and neutrons. In the 1960s, Murray Gell-Mann and George Zweig proposed the idea that protons and neutrons are not in fact elementary particles, but are built from constituents called quarks [1, 2]. This idea gained popularity over the following years and was substantiated in the late 1960s, as by scattering electrons off protons experimental proof for protons consisting of smaller constituents was found [3]. A model where these components are called partons was developed by Richard P. Feynman [4] and by James Bjorken and Emmanuel Paschos [5] within the following year. Until the early 1970s, quantum chromodynamics (QCD) was developed as a non-abelian gauge theory to describe the quarks carrying color charge and interacting through the strong force mediated by so-called gluons [6]. Quarks are classified by flavor, and quarks of six different flavors (up, down, charm, strange, top, bottom) have been discovered by now. Quarks form colorless bound states, known as hadrons, where states with a (valence) quark and antiquark are called mesons and states with three quarks are called baryons.

There are two broadly applicable techniques to perform QCD calculations: At large virtualities, the strong coupling constant α_s is small and perturbative methods can be applied. However, perturbative QCD has limits and, for example, the internal structure of hadrons is of non-perturbative nature, since the characteristic virtualities are only of the order of the strong interaction scale Λ_{QCD} . The second approach, lattice QCD, uses four-dimensional Euclidean space-time lattices [7] to discretize QCD and estimate observables as expectation values of operators with Monte Carlo methods. Time has to be imaginary to enable lattice QCD simulations, and thus it is not possible to directly calculate physical time dependence.

Within QCD, the hadronic structure is characterized by a variety of distribution functions, as shown in fig. 1.1. The simplest of those functions are

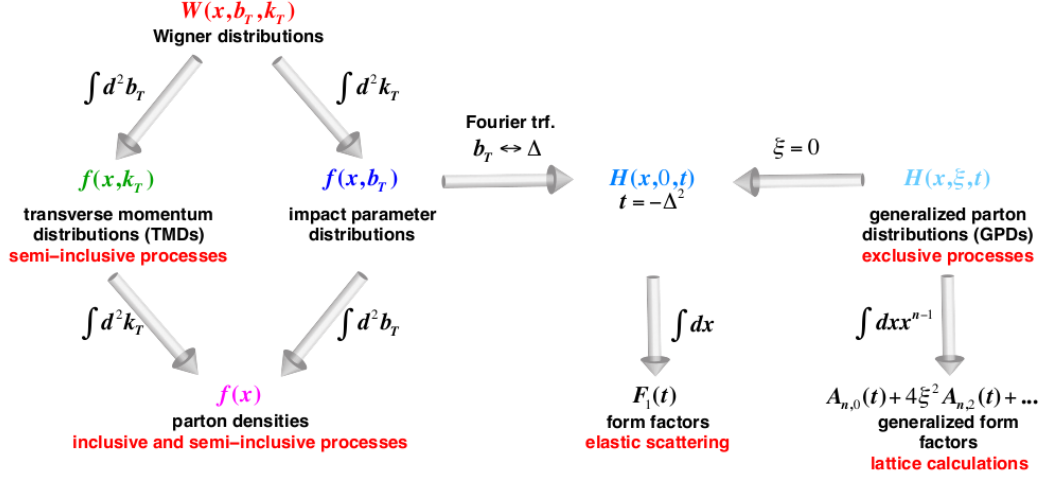


Figure 1.1: Various functions that describe the distribution of partons inside a hadron. The figure is taken from [8].

the parton densities, also called parton distribution functions (PDFs). They are interpreted as probabilities of finding a parton (i.e. a quark or a gluon) inside a hadron, with the parton carrying a fraction x of the hadronic momentum. Since PDFs only consider parton momenta collinear to the hadron's momentum, a natural generalization is given by transverse momentum dependent parton distribution functions (TMDPDFs) [9, 10, 11, 12, 13, 14], which also account for transverse momentum components of the partons (k_T in fig. 1.1), or the impact parameter (b_T in fig. 1.1), which is the Fourier conjugate to the transverse momentum component. In fig. 1.1, and often also in the literature, TMDPDFs are referred to as TMDs, an abbreviation which will not be used in this thesis in order to avoid confusion with other transverse momentum dependent functions as for example transverse momentum dependent wave functions (TMDWFs) [15, 16, 17] or transverse momentum dependent fragmentation functions (TMDFs) [9, 18, 19]. The variability in nomenclature already indicates the wide range of the field of transverse hadron structure and the fact that their investigation is still in a pioneering stage.

High-energy colliders such as the Large Hadron Collider (LHC) at CERN or the Electron-Ion Collider (EIC) [8, 20, 21] at BNL have been built, respectively are planned to be built, where one of the goals is to gain information about the aforementioned distribution functions. In general, PDFs can be obtained with deep inelastic scattering (DIS) [3, 22], an inclusive process where a lepton, for example an electron, scatters off a hadron, and only the scattered lepton is observed, see fig. 1.2a. Information about TMDPDFs can

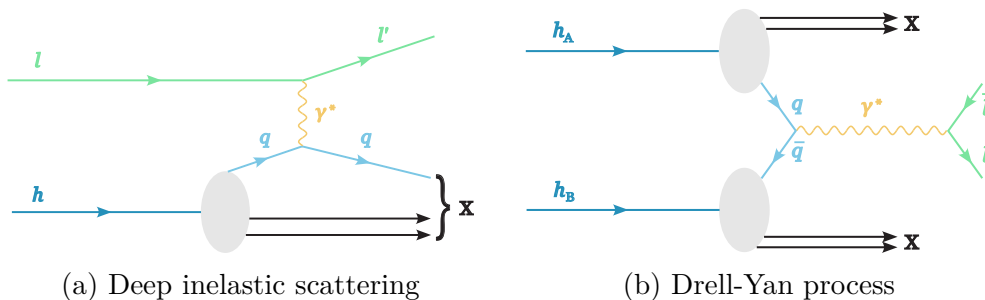


Figure 1.2: (a): Illustration of deep inelastic scattering. A lepton l scatters off a constituent quark q of the hadron h through the exchange of a virtual photon γ^* . The hadronic final state X is unobserved. (b): Illustration of a Drell-Yan process. The hadrons h_A and h_B collide and a quark q and antiquark \bar{q} annihilate, creating a pair of lepton l and antilepton \bar{l} via the exchange of a virtual photon γ^* . The hadronic final states X are unobserved.

only be found with semi-inclusive DIS (SIDIS), where the process is the same as for DIS, but the final state of the hadron is also partially observed, or with the Drell-Yan (DY) process. In DY, two hadrons collide and a quark and antiquark annihilate, creating a lepton-antilepton pair through the exchange of a virtual photon, see fig. 1.2b.

In recent years, technical advances have been made which enable using polarized beams and or targets in experiments [23, 20, 21], opening up possibilities to study also the spin structure of hadrons. Examples for distribution functions concerning in particular the transverse spin structure are the transversity PDF [24, 25] and the Boer-Mulders function [26]. The transversity PDF can be interpreted as the probability to find a transversely polarized parton with momentum fraction x in a transversely polarized hadron. The Boer-Mulders function is a TMDPDF which is also present for an unpolarized hadron as it describes the coupling between the spin and angular momentum of the parton. Both functions are especially difficult to extract from experiments and, therefore, poorly known, see sections 3.1 and 3.4.4, making it even more important to gain knowledge about those distributions from first principles with lattice QCD.

There are two main approaches to performing lattice QCD calculations: On the one hand, it is possible to calculate well-known quantities such as Mellin moments of PDFs [27, 28, 29, 30] and TMDPDFs [31, 32, 33, 34, 35] and aim to improve the accuracy by increased statistics and better control of systematic uncertainties. While these moments can be calculated on the lattice since they only contain local operators, calculating distribution functions directly with conventional lattice QCD methods is not possible since

they involve time dependent correlators. More precisely, a lattice has a much reduced symmetry group compared to continuous space time. Therefore, one has to model PDFs etc. by just a few parameters of which typically at most three or four can be determined. This modeling introduces ambiguities which one would rather like to avoid. On the other hand, there are attempts to extend the current range of calculable quantities by simulating the time dependence of parton observables in alternative ways. A method that has been successfully applied in multiple calculations in the last years [36, 37, 38, 39, 40, 41, 42] is large-momentum effective theory (LaMET) [43, 44] where matrix elements of operators non-local in space are calculated on the lattice for a hadron with large momentum and related to the needed matrix elements non-local in time by perturbative QCD in the continuum.

The second approach is of course significantly more difficult than the first one, but it offers the opportunity to calculate observables which are otherwise not accessible through lattice QCD and also potentially not obtainable from experiments. In this thesis, the LaMET framework is used to investigate the isovector quark transversity PDF in the proton, as well as the quark Boer-Mulders function in the pion, which both belong to the less known distribution functions when compared to the other PDFs and TMDPDFs at leading twist (dimension - spin).

The structure of this thesis is as follows: Basic principles of QCD in the continuum and on the lattice, as well as methods to estimate observables and their uncertainties in lattice QCD calculations are introduced in chapter 2. Chapter 3 establishes LaMET as a framework to perform calculations of parton physics. PDFs and TMDPDFs are defined in sections 3.1 and 3.4, respectively. LaMET in general is presented in section 3.2, and sections 3.3 and 3.5 focus on the theoretical details of calculating PDFs and TMDPDFs with LaMET. Those details include for example the discussion of divergences and renormalization, as well as the matching to physical light-cone quantities. The technical details and results of the isovector quark transversity PDF calculation for the proton with LaMET are presented in chapter 4. The project is performed within the Lattice Parton Collaboration (LPC) and has been published in [42]. The author of this thesis is one of the main authors of the publication. Chapter 5 shows the analysis and results of the LaMET study of the quark Boer-Mulders function in the pion, which is also performed in collaboration with LPC. In chapter 6, both projects are summarized and an outlook for possible future calculations is given.

Chapter 2

Quantum Chromodynamics on the lattice

The underlying theory for exploring the internal structure of hadrons in this thesis is quantum chromodynamics. A short, non-comprehensive introduction to QCD in the continuum is given in section 2.1. The discretization of QCD on a four-dimensional space-time lattice is discussed in section 2.2. The implementation of fermions and gluons in subsection 2.2.1 is followed by a derivation of the discrete QCD action used in this work in subsection 2.2.2. Gauge ensemble generation with Monte Carlo simulations is covered in subsection 2.2.3, including a short discussion of twisted-mass reweighting and the choice of boundary conditions. Methods that are commonly used in lattice QCD measurements and data analysis are presented in section 2.3. Section 2.4 introduces the gauge ensembles used in this thesis, which are generated by the Coordinated Lattice Simulations effort.

2.1 QCD in the continuum

Quantum chromodynamics (QCD) is the quantum gauge field theory which describes the strong interaction. The gauge theory is non-abelian and its underlying symmetry group is $SU(3)$.

Strong interaction takes place between massive spin- $\frac{1}{2}$ fermions called quarks and massless spin-1 bosons called gluons. A quark with flavor f , space-time position x , Dirac index α and color index c is described by the Dirac 4-spinor $\psi^f(x)_{\alpha,c}$, with possible Dirac and color indices being $\alpha = 1, 2, 3, 4$ and $c = 1, 2, 3$. This leads to a quark field $\psi^f(x)$ having 12 independent components. Color and spinor indices are not considered in this notation, and will be suppressed in the used notation.

The six possible flavors of quarks are up, down, charm, strange, top and bottom. In this list, the flavors are sorted from lightest to heaviest, where in calculations usually only the lightest quark flavors are included, leading for example to a number of flavors of $N_f = 3$, which is often written as $N_f = 2 + 1$ in the case of equal up and down quark masses.

A gluon at space-time point x with color indices c and d and $c, d = 1, 2, 3$ is described by the vector gauge field $A_\mu(x)_{cd}$ with Euclidean Lorentz-index $\mu = 1, 2, 3, 4$. Again, the color indices will be omitted in the following description.

The action of quantum chromodynamics in continuum space-time is given by

$$S_{\text{QCD}}(\psi, \bar{\psi}, A_\mu) = \sum_f \int d^4x \bar{\psi}^f(x) \left(i\gamma^\mu D_\mu(x) - m^f \right) \psi^f(x) - \frac{1}{2g^2} \int d^4x \text{tr} [F_{\mu\nu}(x)F_{\mu\nu}(x)], \quad (2.1)$$

where the first line of (2.1) constitutes the fermionic part with quark fields ψ and $\bar{\psi} = \psi^\dagger \gamma_4$. It contains a sum over all quarks with flavor f and mass m^f as well as the covariant derivative:

$$D_\mu(x) = \partial_\mu + iA_\mu(x). \quad (2.2)$$

The fermionic part of the action is invariant under the transformations

$$\begin{aligned} \psi(x) &\rightarrow \psi'(x) = \Omega(x)\psi(x) \\ \bar{\psi}(x) &\rightarrow \bar{\psi}'(x) = \bar{\psi}(x)\Omega(x)^\dagger, \end{aligned} \quad (2.3)$$

where $\Omega(x)$ are unitary matrices which fulfill $\Omega(x)^\dagger = \Omega(x)^{-1}$ and have unit determinant. In QCD, those complex matrices are the SU(3) matrices with dimension 3×3 . Note that the fermion field $\psi(x)$ and $D_\mu(x)\psi(x)$ transform in the same way. The invariance of the fermion action under the gauge transformation (2.3) requires the following transformation property for the gauge field:

$$A_\mu(x) \rightarrow A'_\mu(x) = \Omega(x)A_\mu(x)\Omega(x)^\dagger + i(\partial_\mu\Omega(x))\Omega(x)^\dagger. \quad (2.4)$$

The second line of (2.1) is the gluonic part of the QCD action which contains the coupling strength g . The field strength tensor

$$F_{\mu\nu}(x) = -i[D_\mu(x), D_\nu(x)] \quad (2.5)$$

is defined as a commutator of covariant derivatives. The trace in (2.1) runs over color indices and guarantees the invariance of the gauge action under gauge transformations.

It is possible to add a gauge-fixing term to the action in (2.1), introducing a non-trivial additional Jacobian determinant, which is canceled by unphysical auxiliary fields ξ , the so-called ghost fields. This procedure for gauge fixing is called Faddeev-Popov method [45]. Since we focus on the calculation of gauge-invariant quantities in lattice QCD, this method is not further discussed here.

Perturbative calculations of Feynman diagrams containing loops lead to ultraviolet divergences. These divergences can be isolated in well-defined expressions using a regularization scheme such as dimensional regularization. In lattice QCD, which will be discussed in the following section, the lattice spacing a is used as a cutoff regulator. After regularization, parameters are rescaled such that all divergences cancel. This process called renormalization does not set the results of a calculation to a distinct numerical value. To fix this problem, a renormalization scheme such as the modified minimal subtraction scheme ($\overline{\text{MS}}$) [46] is usually chosen. This in turn leads to results depending on the unphysical renormalization scale μ .

2.2 Concepts of QCD on the lattice

With the QCD action as in eq. (2.1), observables can be calculated as expectation values of operators $O(\psi, \bar{\psi}, A_\mu)$

$$\begin{aligned} \langle 0|O|0\rangle &= \frac{1}{Z} \int D[\psi]D[\bar{\psi}]D[A_\mu]O(\psi, \bar{\psi}, A_\mu) e^{iS_{\text{QCD}}(\psi, \bar{\psi}, A_\mu)} \\ Z &= \int D[\psi]D[\bar{\psi}]D[A_\mu]e^{iS_{\text{QCD}}(\psi, \bar{\psi}, A_\mu)}, \end{aligned} \tag{2.6}$$

where Z is the partition function. The expectation value is obtained by evaluating the path integral over the fields ψ , $\bar{\psi}$ and A_μ . The QCD action enters in the weight $e^{iS_{\text{QCD}}(\psi, \bar{\psi}, A_\mu)}$ for each of these possible configurations.

Perturbation theory can be applied in the high energy regime to calculate observables, since the strong coupling $\alpha_S = g^2/4\pi$ gets small. In contrary, when the energies approach the strong interaction scale Λ_{QCD} or lower values, α_S diverges and other methods are needed to perform calculations.

2.2.1 Formulation of fermions and gluons on the lattice

One approved method for non-perturbative calculations in QCD is the discretization of space-time on a four-dimensional lattice with spacing a , with

$$x = an \tag{2.7}$$

being any space-time point. The vector n exists on a $N_s^3 \times N_t$ lattice given by

$$\Lambda = \{n \mid n_\mu \in \{0, 1, \dots, N_s - 1\}, \mu = 1, 2, 3; n_4 \in \{0, 1, \dots, N_t - 1\}\}. \tag{2.8}$$

Fermion fields $\psi(n)$ are defined on the lattice sites only and are introduced as Grassmann numbers to obey Fermi statistics. The gauge link $U_\mu(n)$ connects the lattice point n with point $n + \hat{\mu}$, $\mu \in \{1, 2, 3, 4\}$ being a direction. The gauge links are elements of SU(3) and transform under gauge transformations as

$$U_\mu(n) \rightarrow U'_\mu(n) = \Omega(n)U_\mu(n)\Omega^\dagger(n + \hat{\mu}). \tag{2.9}$$

Forward and backward links can be related by $U_{-\mu}(n) = U^\dagger(n - \hat{\mu})$. In order to formulate a discretized version of the QCD action given in eq. (2.1), the partial derivative is expressed on the lattice in a symmetric way:

$$\partial_\mu \psi(x) \rightarrow \frac{1}{2a} [\psi(n + \hat{\mu}) - \psi(n - \hat{\mu})]. \tag{2.10}$$

Further details about the formulation of QCD on a lattice can be found in [47]. Note that the action enters as $e^{iS_{\text{QCD}}}$ in the expectation value given in eq. (2.6). In order to perform simulations of QCD on the lattice, a Wick rotation $t \rightarrow -it$ from Minkowski to Euclidean time is performed. This leads to the exponential in eq. (2.6) becoming a real weight, making Monte Carlo simulations possible.

2.2.2 Discretized version of the QCD action

To simulate QCD on a discrete lattice, a discretized version of the QCD action is needed. It is built by combining a discrete formulation of the gauge action with a discrete formulation of the fermion action. From the different possible choices, the focus of this section lies on the Lüscher-Weisz gauge action and Wilson-clover fermion action.

Discrete gauge action

Since the discrete gauge action has to be invariant under gauge transformations, it is constructed from a gauge-invariant combination of link variables $U_\mu(n)$. Considering the transformation properties in eq. (2.9), it is clear that every closed path built of gauge links is invariant under gauge transformations. The plaquette, consisting of only four links, is the simplest choice:

$$U_{\mu\nu}(n) = U_\mu(n)U_\nu(n + \hat{\mu})U_{-\mu}(n + \hat{\mu} + \hat{\nu})U_{-\nu}(n + \hat{\nu}). \quad (2.11)$$

By constructing the sum over all plaquettes on a lattice, counting each one with exactly one orientation and defining the inverse coupling as $\beta = 6/g^2$, the Wilson gauge action is expressed as

$$S_G[U] = \frac{\beta}{3} \sum_{n \in \Lambda} \sum_{\mu < \nu} \text{Re tr}[\mathbf{1} - U_{\mu\nu}(n)]. \quad (2.12)$$

It can be shown that this definition of the discrete gauge action approaches the continuum action up to $\mathcal{O}(a^2)$.

Since lattice simulations use finite lattice spacings a , discretization errors are present and should be reduced as far as possible. Discretization errors can be lowered by adding specific terms to the action and matching their coefficients such that the continuum limit is not changed. This procedure is called Symanzik improvement [48, 49] and applying it to the Wilson gauge action yields the tree-level improved Lüscher-Weisz gauge action $S_G^{LW}[U]$ [50, 51] with discretization effects of $\mathcal{O}(g^2 a^2)$.

Discrete fermionic action

Using the fermion fields $\psi(n)$ and gauge links $U_\mu(n)$, which have been introduced in section 2.2.1, fermions in an external gauge field can be described on the lattice using the naive fermion action:

$$S_F[\psi, \bar{\psi}, U] = a^4 \sum_{n \in \Lambda} \sum_f \bar{\psi}^f(n) \left(\sum_{\mu=1}^4 \gamma_\mu \right. \\ \left. \times \frac{U_\mu(n)\psi^f(n + \hat{\mu}) - U_{-\mu}(n)\psi^f(n - \hat{\mu})}{2a} + m^f \psi^f(n) \right). \quad (2.13)$$

The sum over quark flavors runs up to N_f . The gauge invariance of this formulation of the action can be verified by using the transformation properties of the fermion fields and links, and the relation $U_{-\mu}(n) = U^\dagger(n - \hat{\mu})$.

The naive fermion action can be rewritten in terms of the naive Dirac operator $D(n|m)_{ab}^{\alpha\beta}$:

$$S_F[\psi, \bar{\psi}, U] = a^4 \sum_{n,m \in \Lambda} \sum_f \sum_{a,b,\alpha,\beta} \bar{\psi}^f(n)_{\alpha,a} D^f(n|m)_{\alpha\beta} \psi^f(m)_{\beta,b}$$

$$D^f(n|m)_{\alpha\beta} = \sum_{\mu=1}^4 \frac{U_\mu(n)_{ab} \delta_{n+\hat{\mu},m} - U_{-\mu}(n)_{ab} \delta_{n-\hat{\mu},m}}{2a} + m^f \delta_{\alpha\beta} \delta_{ab} \delta_{nm}. \quad (2.14)$$

The inverse $D^{-1}(n|m)$ of the Dirac operator is called quark propagator and in the continuum case represents a single fermion, with $D^{-1}(n|m)$ having exactly one pole. In the lattice formulation of QCD, the Dirac propagator exhibits 15 additional poles corresponding to 15 unphysical fermions, which are referred to as doublers.

To remove the doublers, Wilson suggested to add an additional term to the Dirac operator, which leads to the doublers decoupling from the theory as $a \rightarrow 0$. Thus, by adding the so-called Wilson term, the continuum Dirac operator is obtained in the continuum limit. Defining $\gamma_{-\mu} = -\gamma_\mu$ for $\mu = 1, 2, 3, 4$, the Wilson Dirac operator can be written as

$$D^{f,\text{Wilson}}(n|m)_{\alpha\beta} = \left(m^f + \frac{4}{a}\right) \delta_{\alpha\beta} \delta_{ab} \delta_{nm} - \frac{1}{2a} \sum_{\pm\mu} (\mathbb{1} - \gamma_\mu)_{\alpha\beta} U_\mu(n)_{ab} \delta_{n+\hat{\mu},m}, \quad (2.15)$$

and the Wilson fermion action takes the following form:

$$S_F^{\text{Wilson}}[\psi, \bar{\psi}, U] = a^4 \sum_{n,m \in \Lambda} \sum_f \sum_{a,b,\alpha,\beta} \bar{\psi}^f(n)_{\alpha,a} D^{f,\text{Wilson}}(n|m)_{\alpha\beta} \psi^f(m)_{\beta,b}. \quad (2.16)$$

The Wilson fermion action has discretization effects of $\mathcal{O}(a)$. As for the discrete gauge action, Symanzik improvement can be used to reduce those. An $\mathcal{O}(a)$ -improved Wilson fermion action is obtained by adding a so-called clover term [52] to the action:

$$S_F^{\text{Wilson-clover}}[\psi, \bar{\psi}, U] = S_F^{\text{Wilson}}[\psi, \bar{\psi}, U] + c_{\text{SW}} a^5 \sum_{n \in \Lambda} \sum_{\mu < \nu} \bar{\psi}(n) \frac{1}{2} \sigma_{\mu\nu} F_{\mu\nu}(n) \psi(n). \quad (2.17)$$

The coefficient c_{SW} is referred to as Sheikholeslami-Wohlert coefficient, and a common choice for $F_{\mu\nu}(n)$ is

$$\begin{aligned}
F_{\mu\nu}(n) &= \frac{-i}{8a^2}(Q_{\mu\nu}(n) - Q_{\nu\mu}(n)) \\
Q_{\mu\nu}(n) &= U_{\mu\nu}(n) + U_{\nu-\mu} + U_{-\mu-\nu} + U_{-\nu\mu}.
\end{aligned}
\tag{2.18}$$

In order to remove all $\mathcal{O}(a)$ -effects from the fermionic action, the coefficient c_{SW} has to be determined non-perturbatively.

2.2.3 Generation of ensembles with Monte Carlo simulations

In the last section, a formulation of the QCD action on a finite lattice in Euclidean space-time was derived, consisting of the Lüscher-Weisz gauge action and the Wilson-clover fermion action:

$$S_{\text{QCD}}[\psi, \bar{\psi}, U] = S_G^{LW}[U] + S_F^{\text{Wilson-clover}}[\psi, \bar{\psi}, U]. \tag{2.19}$$

Using this discretized form of the action, physical observables can be calculated on the lattice by evaluating expectation values as in eq. (2.6). To do so, the path integral is substituted by a sum over all field configurations with given initial and final state, being $|0\rangle$ in case of eq. (2.6).

Since the expression for the path integral contains a Boltzmann factor of e^{-S} , which depends on the fields, each configuration contributes to the sum with a different weight. The configurations with large weights are of higher importance in the sum, leading to the concept of importance sampling. The sampling is performed according to the weights, and more configurations with larger weight are generated during the simulations, using the Hybrid Monte Carlo (HMC) algorithm [53].

The probability distribution according to which the gauge field configurations are sampled is

$$P[U] = \frac{1}{Z} e^{-S_G[U]} \prod_f \det[D_f]. \tag{2.20}$$

The distribution contains a product over flavors of fermion determinants $\det[D_f]$, which are identical to fermionic partition functions:

$$\det[D_f] = Z_F[U] = \int D[\psi^f, \bar{\psi}^f] e^{-S_F[\psi^f, \bar{\psi}^f, U]}. \tag{2.21}$$

Using the Matthews-Salam formula, it can be shown that the fermionic partition functions are in fact determinants. A proof is found for example in [47].

Since the fermion determinants function as weights in the probability distribution in eq. (2.20), they have to be real and positive. Due to γ_5 -hermiticity of the Dirac operator, the determinant is real. In the case of the up and down quark having equal masses, i.e. $m_u = m_d = m_l$ with m_l being the light quark mass, it can be shown that the light quark determinant is positive [47].

A Markov process is used to find configurations with the correct probability distribution. The Markov chain begins from an arbitrary configuration and stochastically evolves towards an area of configurations with large Boltzmann factor.

Twisted-mass reweighting

The generation of gauge fields can suffer from algorithmic instabilities when especially light Wilson quarks are used. To stabilize the simulations, twisted-mass reweighting [54] can be employed to separate the low modes of the Dirac operator of the light quarks and exclude those modes from the simulations.

In case of mass-degenerate light quarks, the product of u and d quark determinants can be formulated as one light quark determinant:

$$\det[D_u]\det[D_d] = \det[D_l]\det[D_l] = \det[D_l^\dagger]\det[D_l] = \det[D_l^\dagger D_l]. \quad (2.22)$$

There are multiple choices for an exact factorization of the light quark determinant

$$\det[D_l^\dagger D_l] = W_l \det[\tilde{D}_l^\dagger \tilde{D}_l], \quad (2.23)$$

where \tilde{D}_l is a modified Dirac operator with shifted eigenvalue spectrum, which is then used in the HMC algorithm to avoid instabilities. The reweighting factor W_l has to be considered for every gauge configuration to compensate for the modification of the Dirac operator. Details about possible modifications and the calculation of reweighting factors can be found in [54]. The practical implementation of reweighting in the data analysis will be discussed in section 2.3.3.

Boundary conditions

To enable non-perturbative calculations of observables with lattice QCD, the discrete space-time lattice is finite. Due to this finite nature of the lattice, the behavior at the boundaries has to be well-defined.

Periodic boundary conditions in all four directions are a common choice since they preserve translational invariance. However, with decreasing lattice spacing, the simulations can get trapped in a certain topological charge sector, leading to a loss of ergodicity and biased results. This problem can be avoided by imposing open boundary conditions in time for the gauge field [55] when using small lattice spacings. This method for choosing the boundary conditions is applied by the Coordinated Lattice Simulations (CLS) effort [56], whose gauge ensembles are used for the projects presented in this thesis.

2.3 Methods in lattice QCD measurements and analysis

After briefly having explained the generation of gauge configurations which are used to calculate expectation values in lattice QCD, this section presents certain methods that are used to obtain those expectation values and corresponding error estimates in practice.

2.3.1 Propagator calculation

As introduced in eq. (2.6), observables in lattice QCD are calculated as expectation values of operators. Those operators typically involve multiple fermion and antifermion fields, and the corresponding fermionic expectation values are related to quark propagators with Wick's theorem, see for example section 5.1.6. in [47]. As mentioned below eq. (2.14), the quark propagator is the inverse of the Dirac operator. $D^{-1}(n|m)$ is a $12V \times 12V$ matrix, with V denoting the volume of the four-dimensional lattice. Each element $D^{-1}(n|m)_{ba}^{\beta\alpha}$ connects a source with space-time position m , Dirac index α and color index a with a sink with position n , Dirac index β and color index b . The calculation and storage of the complete matrix, also called all-to-all propagator, for each gauge configuration, is usually avoided.

Point sources

Following the notation of [47], the computation can be limited to a single column of the propagator by taking into account a specific source position m_0 with Dirac index α_0 and color index a_0 , resulting in a so-called point-to-all propagator

$$\begin{aligned}
D^{-1}(n|m_0)_{ba_0}^{\beta\alpha_0} &= \sum_{m,\alpha,a} D^{-1}(n|m)_{ba}^{\beta\alpha} S_0^{(m_0,\alpha_0,a_0)}(m)_a^\alpha \\
S_0^{(m_0,\alpha_0,a_0)}(m)_a^\alpha &= \delta(m - m_0) \delta_{\alpha\alpha_0} \delta_{aa_0},
\end{aligned} \tag{2.24}$$

where S_0 is called point source. Eq. (2.24) is equivalent to a system of equations $DG = S$ with Dirac matrix D , desired propagator vector G and source vector S . In the case of a point source, there are 12 equations to be solved, one for each combination of Dirac and color indices. The propagator can be calculated numerically with iterative methods, using for example a multigrid algorithm [57, 58].

The three-point correlation functions, which will be defined in sections 4.2.2 and 5.2.2 for the transversity PDF and Boer-Mulders function, describe propagation from a source at x_{src} to a sink at x_{snk} with an operator inserted at x_{ins} . The point-to-all propagator from x_{src} to all other points of the lattice is calculated as just described, and gives $D^{-1}(x_{\text{snk}}|x_{\text{src}})$. In addition, the three-point correlation functions in general also involve all-to-all propagators.

Sequential method

To avoid the computationally expensive inversions needed to obtain the all-to-all propagators, the sequential method was introduced in [59]. Here, the technique is very briefly described for the pion. Due to γ_5 -hermiticity of the quark propagator (see section 5.4.3. in [47] for details), only one all-to-all propagator is needed. Instead of calculating the all-to-all propagator $D^{-1}(x_{\text{ins}}|x_{\text{snk}})$ which connects the sink with all insertion timeslices, the product $D^{-1}(x_{\text{ins}}|x_{\text{snk}})D^{-1}(x_{\text{snk}}|x_{\text{src}})$ is substituted by the sequential propagator

$$\Sigma(x_{\text{ins}}, x_{\text{src}}) = \sum_{\vec{x}_{\text{snk}}} e^{-i\vec{p}\cdot(\vec{x}_{\text{snk}}-\vec{x}_{\text{src}})} D^{-1}(x_{\text{ins}}|x_{\text{snk}}) D^{-1}(x_{\text{snk}}|x_{\text{src}}). \tag{2.25}$$

The sequential propagator can be calculated by inversion of the Dirac operator with the point-to-all propagator $D^{-1}(x_{\text{snk}}|x_{\text{src}})$ as source for the inversion. A momentum phase $e^{-i\vec{p}\cdot(\vec{x}_{\text{snk}}-\vec{x}_{\text{src}})}$ is added to the source before inversion for a non-zero final momentum \vec{p} . It is in general also possible to use a sequential propagator as a source for a second sequential propagator.

2.3.2 Smearing techniques

Momentum smearing for quark fields

Since hadrons are not pointlike, but extended objects, extended quark sources and sinks are necessary to improve the overlap with the desired physical state. This can be achieved for quarks at rest using for example Wuppertal quark smearing [60, 61].

For calculating PDFs and TMDPDFs from the lattice, however, hadrons have to carry non-zero momenta. In order to achieve adequate overlaps of the wave functions of hadrons with their respective ground states even at large momenta, the momentum smearing technique [62] can be employed. This method is based on Wuppertal smearing, while modifying the smearing procedure for a hadron with momentum \vec{p} . The quark smearing is applied iteratively within hadronic sources or sinks, and the quark wave function is built by

$$\psi_{n+1}(x) = \frac{1}{1 + 2d\epsilon} \left[\psi_n(x) + \epsilon \sum_{j=\pm 1}^{\pm d} U_j^{\text{smearred}}(x) e^{i\vec{k}\cdot\vec{j}} \psi_n(x + a\hat{j}) \right]. \quad (2.26)$$

The space dimension is denoted by d , and ϵ is a positive parameter. The gauge links U^{smearred} are obtained by smearing the gauge fields, which will be discussed in the following paragraph. By applying eq. (2.26) to the quark fields, a fraction of the hadron momentum is distributed to the quarks. In the free case, the best choice for the quark momentum \vec{k} is $\vec{k} = \vec{p}/2$ for mesons with mass-degenerate valence quarks and $\vec{k} = \vec{p}/3$ for baryons. For the interacting case, when defining $\vec{k} = \alpha\vec{p}$, the optimal values of α found in [62] are $\alpha \approx 0.8 > 1/2$ for the pion and $\alpha \approx 0.45 > 1/3$ for the proton.

Smearing of gauge fields

Since the gauge field fluctuates strongly over short distances on the lattice, using the unmodified gauge field for the quark smearing could result in a defective quark source or sink. The fluctuations can be softened with gauge smearing.

APE smoothing A possible method for this is APE smoothing [63], where the smeared link is obtained by averaging the unsmeared link $U_\mu(x)$ with its surrounding staples. The procedure is iterative, and one step is described by

$$\begin{aligned}
U_{n+1}(x) &= \mathcal{P}_{\text{SU}(3)} \left(\alpha^{\text{APE}} U_{\mu,n}(x) + S_{\mu,n}(x) \right) \\
S_{\mu,n}(x) &= \sum_{\pm\nu \neq \mu} U_{\nu}(x) U_{\mu}(x + a\hat{\nu}) U_{-\nu}(x + a\hat{\nu} + a\hat{\mu}),
\end{aligned} \tag{2.27}$$

where α^{APE} is a weight factor and

$$\mathcal{P}_{\text{SU}(3)}(V) = X \in \text{SU}(3) \tag{2.28}$$

is a back projection to $\text{SU}(3)$ which maximizes $\text{Re tr}[XV^\dagger]$.

HYP smearing Another procedure for smearing the gauge fields is HYP smearing [64]. A HYP smeared gauge link is constructed by mixing links within hypercubes that are attached to the original link.

In order to avoid modifying the fermion action, smeared gauge fields are not used for the computation of quark propagators.

2.3.3 Error estimation

The calculation of observables in lattice QCD as expectation values of operators was introduced with eq. (2.6). In practice, N_{conf} gauge configurations are used to obtain N_{conf} measurements A_i of an observable:

$$A = \{A_i \mid i = 0, \dots, N_{\text{conf}} - 1\}. \tag{2.29}$$

A set of twisted-mass reweighting factors, which were introduced in eq. (2.23), has to be considered for those gauge configurations:

$$W = \{W_i \mid i = 0, \dots, N_{\text{conf}} - 1\}. \tag{2.30}$$

Note that, compared to (2.23), the subscript l is omitted for better readability. The mean of A , taking into account the reweighting factors, can be written as

$$\bar{A} = \frac{\sum_i W_i A_i}{\sum_i W_i}, \quad i = 0, \dots, N_{\text{conf}} - 1. \tag{2.31}$$

Naively, it could be expected that the error of A can be estimated using the standard deviation

$$\sigma = \sqrt{\frac{1}{N_{\text{conf}}} \sum_i (W_i A_i - \bar{A})^2}. \tag{2.32}$$

However, the standard deviation as in eq. (2.32) is only accurate for normal distributions with a sample size going to infinity. A valid error estimation for an observable computed on the lattice can be achieved using resampling techniques such as jackknife or bootstrap resampling, which approximate the underlying sampling distribution. Since those methods function with statistically independent data, it is important to remove correlations in the dataset A . Typically, binning with bin size b is used, where $N_b = \lfloor \frac{N_{\text{conf.}}}{b} \rfloor$ binned measurements and reweighting factors

$$\begin{aligned} A^b &= \{A_j^b \mid j = 0, \dots, N_b - 1\} \\ W^b &= \{W_j^b \mid j = 0, \dots, N_b - 1\} \end{aligned} \quad (2.33)$$

are produced by taking the average of all data inside a bin

$$\begin{aligned} A_j^b &= \frac{\sum_k W_k A_k}{\sum_k W_k}, \quad k = jb, \dots, jb + b - 1 \\ W_j^b &= \sum_k W_k, \quad k = jb, \dots, jb + b - 1. \end{aligned} \quad (2.34)$$

Using the binned data A^b and reweighting factors W^b , resampling techniques can be applied to estimate the error of an observable A .

Bootstrap resampling

During bootstrap resampling, M samples are generated from the binned data:

$$A^{\text{bootstrap}} = \{A_j^{\text{bootstrap}} \mid j = 0, \dots, M - 1\}. \quad (2.35)$$

The number of samples can be chosen freely, and one sample $A_j^{\text{bootstrap}}$ is obtained by randomly selecting N_b binned measurements and taking the weighted average. Duplicates are possible during the selection. The bootstrap error of A is given by

$$\begin{aligned} \sigma^{\text{bootstrap}} &= \sqrt{\frac{1}{M-1} \sum_{j=0}^{M-1} (A_j^{\text{bootstrap}} - \bar{A}^{\text{bootstrap}})^2} \\ \bar{A}^{\text{bootstrap}} &= \frac{1}{M} \sum_{j=0}^{M-1} A_j^{\text{bootstrap}}. \end{aligned} \quad (2.36)$$

Jackknife resampling

Another resampling method is the jackknife technique, which is a linear approximation of the bootstrap resampling. In jackknife resampling, N_b samples are obtained from the binned data:

$$A^{\text{jackknife}} = \{A_j^{\text{jackknife}} \mid j = 0, \dots, N_b - 1\}. \quad (2.37)$$

The number of jackknife samples equals the number of binned measurements. A sample $A_j^{\text{jackknife}}$ is generated by computing the weighted average of all binned measurements A_i^b , leaving out the measurement with $i = j$. The jackknife error of A is calculated as

$$\begin{aligned} \sigma^{\text{jackknife}} &= \sqrt{\frac{N_b - 1}{N_b} \sum_{j=0}^{N_b-1} \left(A_j^{\text{jackknife}} - \bar{A}^{\text{jackknife}}\right)^2} \\ \bar{A}^{\text{jackknife}} &= \frac{1}{M} \sum_{j=0}^{N_b-1} A_j^{\text{jackknife}}. \end{aligned} \quad (2.38)$$

One of the advantages of resampling methods such as bootstrap and jackknife resampling is the applicability of those methods not only for error estimation of primary, but also of secondary quantities. While primary quantities are measured directly on the lattice, secondary quantities are extracted for example by combining multiple primary quantities, or in fitting procedures.

Covariance matrix

The covariance matrix can be viewed as generalization of variance to multiple dimensions. It is a square matrix containing the covariance values of each pair of elements of a vector. The covariance matrix C of a vector \vec{x} with elements x_i , $i \in \{1, 2, \dots, n\}$ is a $n \times n$ matrix. The diagonal of the covariance matrix is equal to the variance σ^2 of said vector, with σ being the standard deviation introduced in eq. (2.32).

The elements of C can for example be obtained with bootstrap resampling, and the element C_{ij} is given by

$$C_{ij} = \frac{1}{M-1} \sum_{k=0}^M \left(x_{i,k}^{\text{bootstrap}} - \bar{x}_i^{\text{bootstrap}}\right) \left(x_{j,k}^{\text{bootstrap}} - \bar{x}_j^{\text{bootstrap}}\right), \quad (2.39)$$

where the number of bootstrap samples is denoted by M , $x_{i,k}^{\text{bootstrap}}$ is the k th bootstrap sample of x_i , and $\bar{x}_i^{\text{bootstrap}}$ is the bootstrap mean of x_i , see

section 2.3.3. Calculating the covariance matrix for a vector with jackknife resampling is done analogously, where the prefactor $\frac{1}{M-1}$ is replaced with $\frac{N_b-1}{N_b}$, see eq. (2.38).

2.3.4 Fitting

To extract information from observables obtained with lattice QCD calculations, it is crucial to estimate those observables with functions that depend on the lattice data as well as certain parameters. A set of parameters $\{p\}$ that allows for the best description of the data is found by minimizing the χ^2 -functional. Following [65], the χ^2 -functional for data \vec{x} with Gaussian errors and correlations described by a covariance matrix C is given by

$$\chi^2(\{p\}) = \sum_{i,j} (x_i - f(x_i; \{p\})) (C^{-1})_{ij} (x_j - f(x_j; \{p\})), \quad (2.40)$$

where C^{-1} is the inverse of the covariance matrix, which is calculated for example with bootstrap resampling as in eq. (2.39). By iteratively minimizing $\chi^2(\{p\})$ with respect to the parameters $\{p\}$, the best parameters to describe the data with the function $f(x; \{p\})$ are found. For a fit that minimizes $\chi^2(\{p\})$ as defined in eq. (2.40), the value of $\chi^2/\text{d.o.f.}$, where d.o.f. (degrees of freedom) is given by the number of fitted data points minus the number of parameters p , is a measure of the fit quality. For uncorrelated data, $\chi^2/\text{d.o.f.}$ is expected to be 1. A value of $\chi^2/\text{d.o.f.}$ that significantly differs from 1 is either a sign of strong correlations between the data points or an incorrect estimation of the correlations. Generally, either underestimated or negatively correlated errors lead to $\chi^2/\text{d.o.f.}$ being considerably larger than 1, while values of $\chi^2/\text{d.o.f.}$ that are notably smaller than 1 can be the cause of either overestimated or positively correlated errors [65].

In case the correlations between data points are not considered in the fit, only the diagonal of the covariance matrix is taken into account and eq. (2.40) simplifies to

$$\chi^2(\{p\}) = \sum_i \frac{(x_i - f(x_i; \{p\}))^2}{(\sigma_i^{\text{bootstrap}})^2}, \quad (2.41)$$

with $\sigma_i^{\text{bootstrap}}$ denoting the bootstrap error for data point x_i , see eq. (2.36). When performing the fit by minimizing eq. (2.41), the resulting value for $\chi^2/\text{d.o.f.}$ cannot directly be used as a measure of fit quality.

ensemble	β	$a[\text{fm}]$	N_s	N_t	bc	$m_\pi[\text{MeV}]$	$L_s m_\pi$
X650	3.34	0.098	48	48	p	338	8.1
H102	3.4	0.085	32	96	o	354	4.9
H105	3.4	0.085	32	96	o	281	3.9
C101	3.4	0.085	48	96	o	222	4.6
N203	3.55	0.064	48	128	o	348	5.4
N302	3.7	0.049	48	128	o	348	4.2

Table 2.1: Parameters of the CLS ensembles analyzed within this thesis. Given are the inverse coupling β , the lattice spacing a , the geometry specified by $N_s^3 \times N_t$, the boundary conditions in temporal direction (p: periodic, o: open), the pion mass and the dimensionless combination $L_s m_\pi$.

2.4 Gauge ensembles generated by the Coordinated Lattice Simulations effort

CLS ensembles are generated with the tree-level improved Lüscher-Weisz gauge action and 2+1 flavors of non-perturbatively $O(a)$ -improved Wilson fermions. The boundary conditions in spatial direction are periodic, while in temporal direction either periodic or open boundary conditions are employed.

In order to facilitate a controlled limit to the continuum in the calculation of the quark Boer-Mulders function of the pion (see section 5.7.7), and additionally also to the physical pion mass in the calculation of the transversity PDF of the nucleon (see section 4.7.2), gauge ensembles with different lattice spacings and pion masses are selected for the analysis in this thesis. The specifications of these CLS ensembles are summarized in tab. 2.1.

Chapter 3

Parton physics using Large-Momentum Effective Theory

This chapter introduces distribution functions that are key components for the description of the internal hadron structure. In section 3.1, the parton distribution function is introduced in the continuum as the longitudinal momentum distribution of quarks and gluons inside a hadron. For many years, it was not possible to calculate PDFs ab initio from the lattice, but only the leading Mellin moments of PDFs. With large-momentum effective theory, a framework which allows for a direct calculation on the lattice was proposed [43, 44]. A short introduction to LaMET is given in section 3.2. Section 3.3 focuses on the calculation of parton distribution functions from lattice QCD with LaMET, discussing also renormalization and matching to the light-cone PDFs. The generalization of PDFs to include longitudinal as well as transverse parton momenta leads to the transverse momentum dependent parton distribution function, whose continuum definition is given in section 3.4. Details of the lattice calculation of TMDPDFs with LaMET are covered in section 3.5.

The description and nomenclature in this chapter is guided by [66].

3.1 Parton distribution function in the continuum

In Feynman's naive parton model [67], hadrons are composed of so-called partons which are considered to be non-interacting due to large time dilation in the fast moving hadron. The model was originally proposed [4, 5] to

describe deep inelastic scattering (DIS), where a proton is probed using an electron with high energy.

The scattering is best described in the Breit frame, where the proton moves fast in z -direction with a large momentum component P_z :

$$P_\mu = \left(\sqrt{\frac{Q^2}{4x_B^2} + M^2}, 0, 0, \frac{Q}{2x_B} \right). \quad (3.1)$$

The virtual photon moves with $q^z = -Q$ in z -direction, M is the proton mass and $x_B = Q^2/(P \cdot q)$ is the Bjorken scale.

The internal structure of protons with large momenta $P_z \gg \Lambda_{\text{QCD}}$ resembles that structure at $P_z = \infty$ [67]. The limit $P_z \rightarrow \infty$ is approached in the Bjorken limit $Q^2 \rightarrow \infty$, $P \cdot q \rightarrow \infty$. Details on Bjorken scaling can be found in [5, 4].

In the parton model, the scattering of an electron off a proton is approximated by the scattering of the electron off a parton with longitudinal momentum xP_z , weighted by the probability of finding a parton with momentum fraction $0 < x < 1$ inside the proton. These probability distributions can formally be expressed using parton distribution functions.

Most often, parton distribution functions are expressed using time-dependent light-front (LF) correlators. The light-cone or light-front is defined by $t - z = \text{const.}$, and correlations of this type can straightforwardly be characterized using two conjugate light-cone vectors

$$\begin{aligned} p^\mu &= (A, 0, 0, A) \\ n^\mu &= \left(\frac{1}{2}A, 0, 0, -\frac{1}{2}A \right), \end{aligned} \quad (3.2)$$

with parameter A . To further simplify the description of correlations on the light-cone, light-front coordinates can be used:

$$\xi^\mu = (\xi^+, \xi^-, \vec{\xi}_\perp), \quad \xi^\pm = \frac{\xi^0 \pm \xi^3}{\sqrt{2}}, \quad \vec{\xi}_\perp = (\xi_1, \xi_2). \quad (3.3)$$

The Dirac matrices $\gamma^\pm = (\gamma^0 \pm \gamma^3)/\sqrt{2}$ are defined analogously.

At twist-2, there are three different parton distribution functions describing the longitudinal momentum distributions of quarks in a proton, namely the unpolarized, helicity and transversity PDF. The quark transversity PDF of a proton describes the probability of finding a transversely polarized quark with longitudinal momentum fraction x inside a transversely polarized proton. In terms of light-cone coordinates it reads [24, 25]

$$\delta q(x, \mu) = \int \frac{d\xi^-}{4\pi} e^{-ixP^+\xi^-} \langle PS_\perp | \bar{\psi}(\xi^-) \gamma^+ \gamma^\perp \gamma_5 W(\xi^-, 0) \psi(0) | PS_\perp \rangle, \quad (3.4)$$

where $|PS_\perp\rangle$ is a proton state with momentum P in z -direction and transverse polarization S_\perp , and μ is the renormalization scale in the $\overline{\text{MS}}$ scheme. The quark field is denoted by ψ and gauge invariance is ensured by the gauge link $W(\xi^-, 0)$ which runs along the light-cone direction:

$$W(\xi^-, 0) = \mathcal{P} \exp \left[ig \int_{\xi^-}^0 du n \cdot A(un) \right]. \quad (3.5)$$

Path ordering is indicated by \mathcal{P} . The transversity PDF as in eq. (3.4) is supported for $x \in [-1, 1]$. For $x < 0$, the antiquark distribution $\delta \bar{q}(x) = -\delta q(-x)$ can be defined.

Precise knowledge of all parton distribution functions is crucial for a deep understanding of the inner proton structure and interpretation of experimental data. From the twist-2 PDFs, the transversity PDF is the least known from experiment since it is chiral-odd and has to couple to another chiral-odd quantity to be measurable [24, 68, 69]. This is only given for certain transverse spin asymmetries in Drell-Yan processes and SIDIS, making it very challenging to measure [70]. Global analyses of the transversity PDF have been performed by fitting the experimental data [71, 72, 73, 74, 75, 76, 77, 78, 79, 80, 81, 70].

Since only few experimental results are available for the transversity PDF, theoretical determinations are of great importance. However, since lattice QCD is constructed in Euclidean space using imaginary time, time dependent correlations as in eq. (3.4) cannot be calculated directly. Thus, for many years, the theoretical approach to parton distribution functions was limited to the computation of Mellin moments [27, 28, 29, 30]. While it is possible to calculate the lowest few Mellin moments, including the tensor charge g_T [82, 83, 84, 85, 86], it is not feasible to calculate enough moments to model the full x -dependence of PDFs.

Advances in theory have allowed ab initio calculations of PDFs in lattice QCD. These approaches are namely the short-distance expansion defining pseudo-PDFs [87, 88] and the large-momentum effective theory using quasi-PDFs [43, 44]. Since this thesis focuses on calculations in LaMET, the next section gives an introductory presentation of this theory.

3.2 Large-Momentum Effective Theory

Large-momentum effective theory is based on the ideas of Feynman's naive parton model, especially on the assumption that the structure of a hadron is independent of its momentum P if P is larger than the strong interaction scale Λ_{QCD} . Replacing a hadron at large momentum by a hadron at $P = \infty$, its constituents – the so-called partons – become non-interacting due to infinite time-dilation.

This concept is utilized in LaMET by stating that parton distributions, which are time dependent correlations at large hadron momenta, can be determined by calculating time independent correlations at large, but finite, hadron momenta P and taking the limit $P \rightarrow \infty$. This approach has the advantage that time independent correlations can be calculated in lattice QCD, making the full x -dependence of parton distributions accessible from theory.

To illustrate the connection between a hadron at large momentum P and at infinite momentum, fig. 3.1 shows how a line segment in the frame of a hadron moving with momentum P is affected by boosting the hadron to near the light-cone.

Feynman's parton model uses the infinite-momentum limit ($P \gg \Lambda_{\text{UV}} \rightarrow \infty$), while the physical limit is ($\Lambda_{\text{UV}} \gg P \rightarrow \infty$). Due to UV divergences in quantum field theories these two limits are not equivalent and the resulting parton distributions and quasi-parton distributions differ. However, each can be calculated from the other in continuum QCD, resulting in matching functions.

A more technical description of large-momentum effective theory is given in the following section by focusing on the calculation of parton distribution functions in LaMET.

3.3 Parton distribution function from Lattice QCD using Large-Momentum Effective Theory

The core principle of large-momentum effective theory is to make the time dependence of parton distributions such as PDFs accessible by using external states with large momenta. In order to retrieve the quark transversity PDF of a proton, which is defined by (3.4), from the lattice, a time independent, momentum dependent quantity called quasi-PDF is defined:

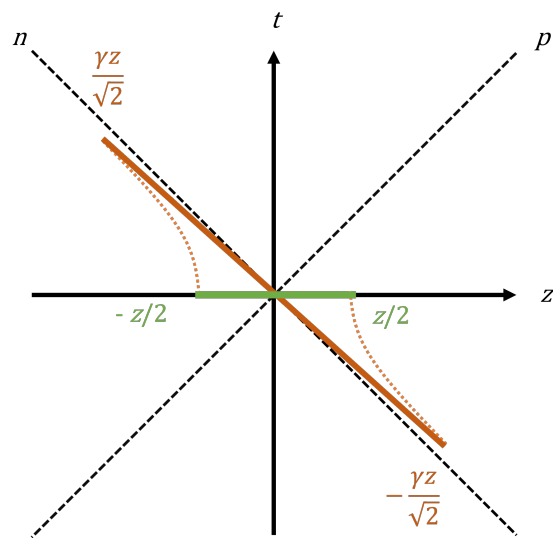


Figure 3.1: A line segment of length z (green) in the frame of a hadron with large momentum in z -direction. In the rest frame of the hadron, the segment (orange) is viewed as approaching the light-cone, which is indicated by the light-cone directions n and p . The two frames are connected by a Lorentz boost with Lorentz factor γ , and the length of the segment after the boost is γz .

$$\begin{aligned}
\delta\tilde{q}(x, P_z, 1/a) &= \int \frac{dz}{2\pi} P_z e^{ixz} \bar{h}(z, P_z, 1/a) \\
\bar{h}(z, P_z, 1/a) &= \frac{1}{2P_0} \langle PS_\perp | \bar{\psi}(z) \gamma^t \gamma^\perp \gamma_5 W(z, 0) \psi(0) | PS_\perp \rangle.
\end{aligned} \tag{3.6}$$

P_z denotes the proton momentum in z -direction and a is the lattice spacing. In the gamma structure, $\gamma^\perp = \gamma^x$ or $\gamma^\perp = \gamma^y$ can be inserted, corresponding to the direction of the transverse proton polarization. These different choices of Euclidean operators lead to the same light-front PDF. $W(z, 0)$ is a straight gauge link in z -direction. The momentum factor in the first line of eq. (3.6) stems from the differential $d\lambda = P_z dz$, while the factor $1/(2P_0)$ in the second line is canceled during renormalization. The time independent matrix element \bar{h} , also called quasi-light-front (quasi-LF) correlation, can be calculated using lattice QCD.

The IR non-perturbative physics of the Euclidean quasi-PDF and the PDF on the light-front is the same, and the differences between those two quantities can be estimated by expanding the P_z -dependence of the quasi-PDF

$$\delta\tilde{q}(y, P_z, \mu) = \int_{-1}^1 \frac{dx}{|x|} C\left(\frac{y}{x}, \frac{\mu}{xP_z}\right) \delta q(x, \mu) + \mathcal{O}\left(\frac{\Lambda_{\text{QCD}}^2}{(yP_z)^2}, \frac{\Lambda_{\text{QCD}}^2}{((1-y)P_z)^2}\right), \tag{3.7}$$

where y is the momentum fraction of the quark. The matching kernel C contains only UV physics and is calculable perturbatively. Power corrections are suppressed by the quark momentum yP_z as well as by $(1-y)P_z$. The renormalization scale is denoted by μ . Details about renormalization will be discussed in section 3.3.2.

By inverting eq. (3.7), the light-front PDF can be expressed in terms of the quasi-PDF, which is crucial for LaMET calculations of PDFs and other parton distributions. The inverted matching formula reads as follows:

$$\delta q(x, \mu) = \int_{-\infty}^{\infty} \frac{dy}{|y|} \tilde{C}\left(\frac{x}{y}, \frac{\mu}{yP_z}\right) \delta\tilde{q}(y, P_z, \mu) + \mathcal{O}\left(\frac{\Lambda_{\text{QCD}}^2}{(xP_z)^2}, \frac{\Lambda_{\text{QCD}}^2}{((1-x)P_z)^2}\right). \tag{3.8}$$

The expansion can already converge at moderately large P_z , while large momenta are especially important to suppress the power corrections in the endpoint regions with small or large momentum fractions x . The next section discusses what momenta are necessary to reach convergence in certain ranges of x .

3.3.1 Validity of the factorization formula

For the factorization formula in eq. (3.8) to be valid, higher twist contributions of order $\mathcal{O}\left(\frac{\Lambda_{\text{QCD}}^2}{(xP_z)^2}\right)$ and $\mathcal{O}\left(\frac{\Lambda_{\text{QCD}}^2}{((1-x)P_z)^2}\right)$ need to be small. This entails the following requirements for the range of momentum fractions x of the quark inside a proton:

$$x \gg \frac{\Lambda_{\text{QCD}}}{P_z}, \quad x \ll 1 - \frac{\Lambda_{\text{QCD}}}{P_z}. \quad (3.9)$$

Wanting to draw conclusions about the possible range of values for x raises the question of which proton momenta P_z can be reached in LaMET calculations. This question can be answered by considering the resolution with which a proton can be investigated on the lattice.

The size of a hadron is momentum dependent and varies with the frame. In order to examine the internal structure of a proton in its rest frame, the lattice spacing has to be considerably smaller than the inverse QCD scale, i.e.

$$a \ll \Lambda_{\text{QCD}}^{-1}. \quad (3.10)$$

Using the typical scale $\Lambda_{\text{QCD}} \approx 200$ MeV of non-perturbative QCD effects, as well as

$$\hbar c \approx 0.1973 \text{ GeV fm}, \quad (3.11)$$

and natural units $\hbar = c = 1$, eq. (3.10) yields $a \ll 0.99$ fm. Thus, a lattice spacing of approximately $a \ll 0.2$ fm is necessary to study a proton at rest.

When the proton has non-zero momentum P_z , the condition in eq. (3.10) changes due to Lorentz contraction of the proton in z -direction, and becomes

$$a \ll (\gamma \Lambda_{\text{QCD}})^{-1}. \quad (3.12)$$

The Lorentz boost factor

$$\gamma = \frac{1}{\sqrt{1 - \frac{v^2}{c^2}}} = \sqrt{1 + \left(\frac{P_z}{m_0 c}\right)^2} \quad (3.13)$$

for a proton with large momentum $P_z = 5$ GeV and rest mass $m_0 \approx 0.938$ GeV is $\gamma \approx 5.4$. Inserting γ in eq. (3.12) leads to the requirement $a \ll 0.18$ fm. Therefore a lattice spacing of $a \leq 0.037$ fm, which is much smaller than in the rest case, is needed to reach the same resolution.

Simulating at such small lattice spacings requires a large amount of computing resources and comes with various other challenges. One of those difficulties is the possibility of the topological charge being trapped in certain sectors in the Monte Carlo simulations, see 2.2.3. Moreover, the signal-to-noise ratio can decrease with small lattice spacings. In consequence, making use of even smaller lattice spacings is currently not possible and even $P_z^{\text{max}} = 5 \text{ GeV}$ has not been reached in LaMET calculations so far.

Inserting $P_z = 5 \text{ GeV}$ in the condition for the momentum fraction in eq. (3.9) gives $x \gg 0.04$ and $x \ll 0.96$. A currently more realistic value of $P_z = 2.5 \text{ GeV}$ yields $x \gg 0.08$ and $x \ll 0.92$, leading to the factorization being valid in an approximate range of $0.1 < x < 0.9$. The actual range of momentum fractions where LaMET calculations are reliable of course depends on the maximum momentum which is implemented in the specific calculation.

3.3.2 Renormalization of quasi-PDFs in the hybrid scheme

The quasi-PDF defined in eq. (3.6) does not only depend on the proton momentum P_z but also on lattice artifacts. In the quasi-LF correlation $\bar{h}(z, P_z, 1/a)$, divergences both linear and logarithmic in the lattice spacing a are present. Theoretically, these divergences should be canceled by higher orders in the matching formula in eq. (3.8), however, in practice it is necessary to apply non-perturbative renormalization.

In the past, various different possibilities for non-perturbative renormalization procedures were proposed, including [89, 90, 91]. Nevertheless, these approaches introduce unwanted IR effects in the quasi-LF correlation at large distances z .

A solution which enables a valid non-perturbative renormalization at all distances was introduced with the hybrid renormalization scheme [92], where short and long distances are renormalized separately. At short distances, the quasi-LF correlation is for example renormalized as in the ratio scheme [90, 93, 94], by dividing it by the same correlation in the rest frame. For long distances, self-renormalization [95] is employed, which removes UV divergences while preserving IR physics.

The quasi-LF correlation renormalized in hybrid scheme is given by

$$\tilde{h}_R(z, P_z) = \frac{\tilde{h}(z, P_z, 1/a)}{\tilde{h}(z, P_z = 0, 1/a)} \theta(z_s - |z|) + \eta_s \frac{\tilde{h}(z, P_z, 1/a)}{Z_R(z, 1/a)} \theta(|z| - z_s), \quad (3.14)$$

where the first and second term are the quasi-LF correlations that are renormalized in the ratio scheme and using self-renormalization, respectively.

The calculation of the renormalization factor $Z_R(z, 1/a)$ will be discussed in this section. The short and long distance regions are separated at $z = z_s$, which is not a fixed length, and should be varied in the perturbative region to find the ideal value which causes the least variation in the result. Continuity of the renormalized quasi-LF correlation at $z = z_s$ is ensured by the factor $\eta_s = Z_R(z_s, 1/a)/\tilde{h}(z_s, P_z = 0, 1/a)$. An additional normalization

$$\tilde{h}(z, P_z, 1/a) = \frac{\bar{h}(z, P_z, 1/a)}{\bar{h}(z = 0, P_z, 1/a)} \quad (3.15)$$

was introduced in eq. (3.14). Due to the normalization, integrating the momentum distribution after Fourier transformation will result in 1 rather than the proton isovector tensor charge g_T . For the extraction of g_T from the matrix elements calculated in this work, see 4.4.

The renormalized quasi-LF correlation in eq. (3.14) does not explicitly depend on the lattice spacing a , since the singular a -dependence is canceled by the renormalization. However, remaining discretization effects need to be taken into account by performing a continuum extrapolation, see section 4.7.2.

Self renormalization The renormalization factor $Z_R(z, 1/a)$ in the self renormalization, which was introduced in eq. (3.14), is given by

$$\begin{aligned} Z_R(z, 1/a) &= \frac{\tilde{h}(z, 1/a)}{\tilde{h}_R(z)} \\ \tilde{h}_R(z) &= \exp[g(z) - m_0 z] = \exp[g_0(z)]. \end{aligned} \quad (3.16)$$

$Z_R(z, 1/a)$ is obtained in two steps. In the first step, to extract $g(z)$, the bare quasi-LF correlations $\tilde{h}(z, P_z = 0, 1/a)$ in the rest frame are fitted with a functional form following from perturbative QCD, which reads [95]

$$\begin{aligned} \ln \tilde{h}(z, 1/a) &= \frac{kz}{a \ln(a\Lambda_{\text{QCD}})} + g(z) + f(z)a^2 \\ &+ \frac{3C_F}{11 - 2N_f/3} \ln \left[\frac{\ln(1/(a\Lambda_{\text{QCD}}))}{\ln(\mu/\Lambda_{\text{QCD}})} \right] + \ln \left[1 + \frac{d}{\ln(a\Lambda_{\text{QCD}})} \right]. \end{aligned} \quad (3.17)$$

The first term on the r.h.s. accounts for the linear divergence. The second term $g(z) = g_0(z) + m_0(z)$ consists of the contribution $g_0(z)$ containing intrinsic non-perturbative physics and of the finite renormalon term $m_0(z)$. Discretization errors are included by $f(z)a^2$. The remaining two terms come

from the resummation of leading and sub-leading logarithmic divergences, and only impact the overall normalization at different lattice spacings.

In the second step, after obtaining $g(z)$ from fitting the bare matrix elements in the rest frame, m_0 is determined. Since the factorization formula given in eq. (3.8) is only valid in the $\overline{\text{MS}}$ scheme, the renormalized quasi-LF correlation $\tilde{h}_R(z)$ needs to be equal to the short distance perturbative $\overline{\text{MS}}$ result in the continuum, which is (see supplemental material of [42])

$$Z_{\overline{\text{MS}}}(z) = 1 + \frac{\alpha_s C_F}{2\pi} (2 \ln(z^2 \mu^2 e^{2\gamma_E}) + 2) \quad (3.18)$$

at one-loop level. This leads to the following condition:

$$\begin{aligned} Z_{\overline{\text{MS}}}(z) &= \tilde{h}_R(z) = \exp[g(z) - m_0 z] \\ \ln Z_{\overline{\text{MS}}}(z) &= g(z) - m_0 z \\ m_0 z &= g(z) - \ln Z_{\overline{\text{MS}}}(z). \end{aligned} \quad (3.19)$$

Thus, m_0 can be extracted by fitting $g(z) - \ln Z_{\overline{\text{MS}}}(z)$ with $m_0 z$. Inserting $g(z)$ and m_0 in eq. (3.16) gives the self renormalization factor.

3.3.3 One-loop matching kernel in the hybrid scheme

After extracting the quasi-LF correlation $\tilde{h}(z, P_z, 1/a)$ from lattice calculations, which will be discussed in detail in section 4.3, and renormalizing it in the hybrid scheme, a Fourier transformation is necessary to obtain the quasi-PDF $\delta\tilde{q}(x, P_z, 1/a)$ in momentum space, which is defined in eq. (3.6). Through matching to the light-cone as in eq. (3.8), the final result for the transversity PDF in the proton is obtained.

To obtain the one-loop matching kernel in the hybrid scheme, the matching kernel in the ratio scheme needs to be calculated. In momentum space, it reads [42]

$$C_r \left(x, \frac{\mu}{p_z} \right) = \delta(1-x) + \frac{\alpha_s C_F}{2\pi} \begin{cases} \left[\frac{2x}{1-x} \ln \frac{x}{x-1} - \frac{2}{1-x} \right]_+ & x > 1 \\ \left[\frac{2x}{1-x} \left(\ln \frac{4p_z^2}{\mu^2} + \ln x(1-x) \right) + 2 \right]_+ & 0 < x < 1 \\ \left[-\frac{2x}{1-x} \ln \frac{x}{x-1} + \frac{2}{1-x} \right]_+ & x < 0, \end{cases} \quad (3.20)$$

and in the hybrid scheme, it is given by [42]

$$\begin{aligned}
C_h\left(x, \frac{\mu}{p_z}, \lambda_s\right) &= C_r\left(x, \frac{\mu}{p_z}\right) + \delta C\left(x, \frac{\mu}{p_z}, \lambda_s\right) \\
&= C_r\left(x, \frac{\mu}{p_z}\right) + \frac{\alpha_s C_F}{\pi} \left[-\frac{1}{|1-x|} + \frac{2\text{Si}((1-x)\lambda_s)}{\pi(1-x)} \right]_+.
\end{aligned}
\tag{3.21}$$

In eq. (3.20) and eq. (3.21), p_z denotes the momentum in z -direction of an on-shell massless external quark state which was used for the derivation in [42]. The long- and short-distance regions in the hybrid renormalization are separated by λ_s , and Si indicates the sign function. A more detailed derivation can be found in [42]. Similar calculations are performed in [96, 97], with results agreeing with the matching kernel given in eq. (3.20) and eq. (3.21).

3.4 Transverse momentum dependent parton distribution function in the continuum

After discussing parton distribution functions in sections 3.1 and 3.3, the logical consequence is to introduce transverse momentum dependent parton distribution functions (TMDPDFs) as a generalization of PDFs, with TMDPDFs including not only longitudinal, but also transverse momenta of partons.

TMDPDFs play a crucial role in the description of the hadronic structure. They enable to access the 3D tomography of hadrons, which is in line with the physical objective of the EIC. Detailed knowledge of TMDPDFs is also exceptionally important for predicting observables in high-energy processes where the transverse momenta of final state particles are measured. Examples for such processes are semi-inclusive deep inelastic scattering (SIDIS) and the Drell-Yan (DY) process, which are investigated at the EIC as well as the LHC.

At first, TMDPDFs have been established by Collins and Soper [9, 10, 11, 12, 13, 14] to describe the Drell-Yan process and electron-positron annihilation. Decades later, they were generalized to also account for SIDIS [98, 99].

3.4.1 Definition of TMDPDFs

At leading twist, there exist eight different TMDPDFs, which can be obtained through Lorentz decomposition of a parent TMD correlator, as will

be discussed in section 3.4.3. This section introduces the transverse momentum dependent parton distribution function in light-cone coordinates by the example of the unpolarized TMDPDF. The Boer-Mulders function, which is one of the main focus points of this thesis, will be introduced in section 3.4.3. Following the nomenclature of [66], the unpolarized TMDPDF can be expressed as

$$f(x, \vec{k}_\perp) = \frac{1}{2P^+} \int \frac{d\lambda}{2\pi} \frac{d^2\vec{b}_\perp}{(2\pi)^2} e^{-i\lambda x + i\vec{k}_\perp \cdot \vec{b}_\perp} \times \langle P | \bar{\psi}(\lambda n/2 + \vec{b}_\perp) \gamma^+ \mathcal{W}(\lambda n/2 + \vec{b}_\perp) \psi(-\lambda n/2) | P \rangle, \quad (3.22)$$

with $|P\rangle$ being an unpolarized hadron state with momentum P in z -direction and $\mathcal{W}(\lambda n/2 + \vec{b}_\perp)$ denoting a staple-shaped gauge link along the light-cone direction n^μ , which is defined as

$$\begin{aligned} \mathcal{W}(\xi) &= W^\dagger(\xi) W_\perp W(-\xi \cdot pn) \\ W(\xi) &= \mathcal{P} \exp \left[-ig \int_0^{-\infty} d\lambda n \cdot A(\xi + \lambda n) \right]. \end{aligned} \quad (3.23)$$

The transverse gauge link W_\perp at infinity is needed for gauge invariance.

Compared to the collinear PDF, which was introduced in eq. (3.4) through the example of the transversity PDF, the TMDPDF in eq. (3.22) exhibits an additional dependence on the transverse parton momentum \vec{k}_\perp , with \vec{b}_\perp being the Fourier conjugate of \vec{k}_\perp . A symmetric placement of the quark and antiquark fields $\psi, \bar{\psi}$ was chosen in eq. (3.22). Choosing to asymmetrically position the fields at $\lambda n + \vec{b}_\perp$ and 0 would lead to the same result.

Note that while the orientation of the staple-shaped gauge link does not matter in the case of unpolarized TMDPDFs, there is a distinction when TMDPDFs are spin dependent. The link \mathcal{W} in eq. (3.22) is past-pointing, matching the kinematics of the DY process. When describing SIDIS, a future-pointing gauge link should be chosen.

3.4.2 Rapidity divergence

The infinitely long light-like gauge links in eq. (3.22) introduce the so-called rapidity divergence. It stems from radiation of gluons collinear to those gauge links and is not regularizable with standard UV regulators. The rapidity divergence can, however, be regularized with various methods, which can be classified as either on-light-cone regulators [100, 101, 102, 103, 104] or

off-light-cone regulators [9, 98, 99]. While the gauge links stay along n^μ after on-light-cone regularization, the off-light-cone regularization removes the rapidity divergence by choosing gauge links in a direction off the light-cone.

Off-light-cone regularization is very well compatible with the ideas of LaMET and is used in the lattice QCD calculations for the TMDPDF in chapter 5. This subsection shortly discusses how to control rapidity divergences in an on-light-cone scheme. For that, it is practical to include the rapidity regulator when defining the TMDPDF. The light-cone TMDPDF in coordinate space, where the staple-shaped gauge link along light-cone direction n^μ is regularized using the δ -regulator [102, 103] in light-cone minus direction, reads

$$f(\lambda, b_\perp, \mu, \delta^-/P^+) = \langle P | \bar{\psi}(\lambda n/2 + \vec{b}_\perp) \not{n} \mathcal{W}(\lambda n/2 + \vec{b}_\perp) |_{\delta^-} \psi(-\lambda n/2) | P \rangle. \quad (3.24)$$

Note that due to rotational invariance, the TMDPDF depends only on the absolute value $b_\perp = |\vec{b}_\perp|$. The staple-shaped link in eq. (3.24) is defined as in eq. (3.23), but uses gauge-links along light-cone direction n^μ regularized with the δ -regulator according to

$$W(\xi) |_{\delta^-} = \mathcal{P} \exp \left[-ig \int_0^{-\infty} d\lambda A^+(\xi + \lambda n) e^{-\frac{\delta^-}{2P^+} |\lambda|} \right]. \quad (3.25)$$

The TMDPDF $f(\lambda, b_\perp, \mu, \delta^-/P^+)$ diverges as $\delta^- \rightarrow 0$.

Soft function

In on-light-cone schemes, rapidity divergences are multiplicative in coordinate space [105], and can be removed by the soft function. Essentially, the soft function is a cross section for color charges moving fast in two conjugate light-cone directions, emitting soft gluons. The TMD soft function emerges from factorization theorems for the Drell-Yan process [14, 106] and SIDIS [99, 107]. For Drell-Yan, it is defined by [108, 109]

$$S(b_\perp, \mu, \delta^+, \delta^-) = \frac{\text{tr} \langle 0 | \mathcal{W}_n(\vec{b}_\perp) |_{\delta^+} \mathcal{W}_p^\dagger(\vec{b}_\perp) |_{\delta^-} | 0 \rangle}{N_c}. \quad (3.26)$$

The TMD soft function contains two staple-shaped gauge links \mathcal{W}_n and \mathcal{W}_p which lie along the light-cone directions n^μ and p^μ , respectively. In eq. (3.26), N_c denotes the number of colors.

For small parameters δ^+ and δ^- , the soft function can be expressed in terms of the rapidity dependent, non-perturbative Collins-Soper evolution kernel $K(b_\perp, \mu)$ [9] and a rapidity independent part $\mathcal{D}_2(b_\perp, \mu)$ [66]:

$$S(b_{\perp}, \mu, \delta^+, \delta^-) = e^{\ln \frac{\mu^2}{2\delta^+\delta^-} K(b_{\perp}, \mu) + \mathcal{D}_2(b_{\perp}, \mu)}. \quad (3.27)$$

The soft function defined in eq. (3.26) and the Collins-Soper kernel and rapidity independent function \mathcal{D}_2 introduced in eq. (3.27) satisfy the following renormalization group equations (RGEs) [66]:

$$\begin{aligned} \mu^2 \frac{d}{d\mu^2} \ln S(b_{\perp}, \mu, \delta^+, \delta^-) &= -\Gamma_{\text{cusp}}(\alpha_s) \ln \frac{\mu^2}{2\delta^+\delta^-} + \gamma_s(\alpha_s) \\ \mu^2 \frac{d}{d\mu^2} K(b_{\perp}, \mu) &= -\Gamma_{\text{cusp}}(\alpha_s) \\ \mu^2 \frac{d}{d\mu^2} \mathcal{D}_2(b_{\perp}, \mu) &= \gamma_s(\alpha_s) - K(b_{\perp}, \mu). \end{aligned} \quad (3.28)$$

In eq. (3.28), $\Gamma_{\text{cusp}}(\alpha_s)$ denotes the cusp anomalous dimension [110] and $\gamma_s(\alpha_s)$ is the soft anomalous dimension [111].

Rapidity renormalization in on-light-cone regularization schemes

For TMDPDFs defined in an on-light-cone scheme, the soft function can be used as a renormalization factor to cancel rapidity divergences, resulting in a renormalized TMDPDF of the following form [112, 113]:

$$f(x, b_{\perp}, \mu, \zeta) = \lim_{\delta^- \rightarrow 0} \frac{f(x, b_{\perp}, \mu, \delta^-/P^+)}{\sqrt{S(b_{\perp}, \mu, \delta^- e^{2y_n}, \delta^-)}}. \quad (3.29)$$

The numerator is obtained by Fourier-transforming eq. (3.24) to momentum space, and the rapidity scale ζ is defined as

$$\zeta = 2(xP^+)^2 e^{2y_n}, \quad (3.30)$$

where y_n is an arbitrarily chosen rapidity parameter. Since the soft function consists of two staple-shaped gauge links, see eq. (3.26), while the numerator $f(x, b_{\perp}, \mu, \delta^-/P^+)$ on the r.h.s. of eq. (3.29) contains only one staple, the square root in eq. (3.29) ensures a proper cancelation of rapidity divergences.

The dependence of the renormalized light-cone TMDPDF on the rapidity scale is described by the Collins-Soper evolution equation

$$2\zeta \frac{d}{d\zeta} f(x, b_{\perp}, \mu, \zeta) = K(b_{\perp}, \mu). \quad (3.31)$$

3.4.3 Decomposition of the TMD correlator in terms of TMDPDFs

The unpolarized TMDPDF has been used to introduce TMDPDFs as a generalization of collinear PDFs in section 3.4.1 and discuss their divergences and renormalization on the light-cone in section 3.4.2. As already mentioned, there are eight different TMDPDFs at leading twist, which will be established in this section. The notation and argumentation of this section is guided by [32].

Decomposition of the TMD correlator in momentum space The unpolarized TMDPDF, which is also known as $f_1(x, \mathbf{k}_\perp, \mu, \zeta)$ in literature, is one of eight TMDPDFs which emerge from the decomposition of the TMD correlators $\Phi^{[\Gamma]}(x, \mathbf{k}_\perp, P, S, \mu, \zeta)$, $\Gamma = \gamma^+, \gamma^+\gamma^5, i\sigma^{i+}\gamma^5$, at leading twist. The TMD correlators are decomposed into TMDPDFs as [114, 115, 116, 117]

$$\begin{aligned}
\Phi^{[\gamma^+]}(x, \mathbf{k}_\perp, P, S, \mu, \zeta) &= f_1 - \left[\frac{\epsilon_{ij} k_i S_j}{m} f_{1T}^\perp \right]_{\text{odd}} \\
\Phi^{[\gamma^+\gamma^5]}(x, \mathbf{k}_\perp, P, S, \mu, \zeta) &= \Lambda g_1 + \frac{\mathbf{k}_\perp \cdot \mathbf{S}_\perp}{m} g_{1T} \\
\Phi^{[i\sigma^{i+}\gamma^5]}(x, \mathbf{k}_\perp, P, S, \mu, \zeta) &= S_i h_1 + \frac{(2k_i k_j - \mathbf{k}_\perp^2 \delta_{ij}) S_j}{2m^2} h_{1T}^\perp \\
&\quad + \frac{\Lambda k_i}{m} h_{1L}^\perp + \left[\frac{\epsilon_{ij} k_j}{m} h_1^\perp \right]_{\text{odd}},
\end{aligned} \tag{3.32}$$

with m being the hadron mass and $\sigma^{\mu\nu} = \frac{i}{2} [\gamma^\mu, \gamma^\nu]$. The helicity and transverse spin component of the hadron are denoted by Λ and S_i , respectively. The indices i and j lie in the plane spanned by the transverse parton momentum \mathbf{k}_\perp . The eight TMDPDFs occurring in eq. (3.32) ($f_1, g_1, h_1, g_{1T}, h_{1L}^\perp, h_{1T}^\perp, f_{1T}^\perp$ and h_1^\perp) depend on x, \mathbf{k}_\perp, μ and ζ , but, for the sake of simplicity, the dependence is not made explicit here. A more detailed discussion and the decomposition of the TMD correlator in terms of Lorentz-invariant amplitudes can be found in [32].

Fig. 3.2 shows a schematic illustration of the various TMDPDFs at leading twist, categorized by the polarization of the hadron and parton, respectively.

As indicated by the brackets $[\]_{\text{odd}}$ in eq. (3.32), the Siverson function f_{1T}^\perp [118] and the Boer-Mulders function h_1^\perp [26] are time reversal odd (T-odd) TMDPDFs. Both functions are related to the single transverse spin asymmetry [26, 119, 120, 121]. While the Siverson function represents the unpolarized


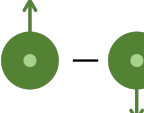


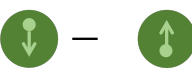
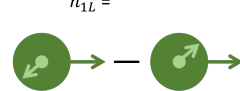
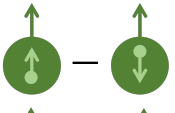

Hadron \ Parton	Unpol.	Long.	Trans.
Unpol.	$f_1 =$ 		$f_{1T}^\perp =$ 
Long.		$g_1 =$ 	$g_{1T} =$ 
Trans.	$h_1^\perp =$ 	$h_{1L}^\perp =$ 	$h_1 =$  $h_{1T}^\perp =$ 

Figure 3.2: Schematic illustration of the eight different leading twist TMD-PDFs f_1 , g_1 , h_1 , g_{1T} , h_{1L}^\perp , h_{1T}^\perp , f_{1T}^\perp and h_1^\perp . The dark green circles and arrows represent hadrons and hadron polarization, while the light green circles and arrows depict partons and their respective polarization.

parton distribution in a transversely polarized hadron, the Boer-Mulders function describes the transverse polarization of partons in an unpolarized hadron. The extraction of the quark Boer-Mulders function of a pion from lattice QCD using LaMET will be the topic of chapter 5.

Decomposition of the TMD correlator in position space Since b_\perp -dependent matrix elements are obtained from the lattice, see 5.3, a decomposition of the TMD correlator in \mathbf{b}_\perp -space is given here. Such a decomposition is found by Fourier-transforming the decomposition in \mathbf{k}_\perp -space with respect to \mathbf{k}_\perp . After setting the helicity as well as transverse spin components of the hadron to zero for the Boer-Mulders case with an unpolarized hadron, the decomposition of the TMD correlator in position space can be written as [122]

$$\Phi^{[i\sigma^{i+}\gamma_5]}(x, \mathbf{b}_\perp, P, S = \Lambda = 0, \mu, \zeta) = i\epsilon^{ij} b_{\perp j} m h_1^\perp(x, b_\perp). \quad (3.33)$$

In eq. (3.33), $h_1^\perp(x, b_\perp)$ denotes the Boer-Mulders function in b_\perp -space. Note that the tilde which is used in [122] to highlight the b_\perp -dependence of the Boer-Mulders function is omitted here to avoid confusion with the quasi-observables in this thesis. This form of the decomposition will be needed

when extracting the Boer-Mulders function from the lattice data, since the factors b_\perp and m have to be considered. Note that $h_1^\perp(x, b_\perp)$ is a real function, for an explicit check see for example the perturbative computation in [123], where the function E_q in eq. (4.19) is real.

3.4.4 Previous TMDPDF determinations

Gaining knowledge about TMDPDFs is difficult and information about those distribution functions is currently very limited. One main approach to study TMDPDFs is fitting experimental data with models [124, 125, 78, 126, 127, 128, 129]. However, due to the deficient data, these global fits are not completely satisfactory. Even though in the future the EIC will add to the experimental data suitable for TMDPDF extractions, it is still very important to investigate TMDPDFs from first principles. Theoretical determinations in turn can also be used in the choice of models for the fits of experimental data, or as test of those fits.

Until recently, the main approach to gain information about TMDPDFs using lattice QCD has been to calculate Mellin moments of distribution functions and use either these moments or ratios of these moments to extract for example certain Lorentz-invariant amplitudes [31] or generalized shifts [32, 33, 34]. The Collins-Soper kernel can also be determined very efficiently by studying ratios of Mellin moments [35]. But since a calculation beyond the first few moments is currently not feasible, it is not possible to reliably predict the x -dependence of TMDPDFs using Mellin moments.

From the eight TMDPDFs at leading twist, the Boer-Mulders function $h_1^\perp(x, b_\perp)$ is one out of two distribution functions that also occur in an unpolarized hadron, which leads to special interest for this particular TMDPDF. However, the insights gained so far from theoretical as well as phenomenological studies are very limited. An analysis of lattice data as well as phenomenological models from 2008 [130] predicts similarities of the Boer-Mulders function for different hadrons. Similarities of the Boer-Mulders function and Boer-Mulders shift across hadrons were also claimed in [131] and [33], respectively, but could not be verified to this day with a direct calculation of $h_1^\perp(x, b_\perp)$. Other studies include for example the lattice QCD calculation of the generalized Boer-Mulders shift [32, 33, 34] and a determination of the Boer-Mulders function from global fits to ATLAS data for the angular coefficient A_2 [132], which does not lead to significant constraints for h_1^\perp . Similar to collinear PDFs, it is possible to investigate the full x -dependence of TMDPDFs like h_1^\perp on the lattice using LaMET.

3.5 Transverse momentum dependent parton distribution function from Lattice QCD using Large-Momentum Effective Theory

This section describes the investigation of TMDPDFs on the lattice in LaMET, which includes the definition of quasi-TMDPDFs in section 3.5.1 and a discussion of their renormalization in section 3.5.2. The Collins-Soper kernel and soft function are the subjects of discussions in sections 3.5.3 and 3.5.4, respectively. Both quantities are necessary for matching the quasi-TMDPDF to the light-cone, see section 3.5.5.

3.5.1 Definition of quasi-TMDPDFs

When studying TMDPDFs from first principles with LaMET, the starting point is the quasi-TMDPDF, which contains an equal-time matrix element that can be calculated on the lattice. The subtracted quasi-Boer-Mulders function in coordinate space reads

$$\tilde{h}_1^\perp(z, b_\perp, P_z, a) = \lim_{L \rightarrow \infty} \frac{\langle P | \bar{\psi}(b_\perp \hat{n}_\perp) \Gamma \mathcal{W}_z(b_\perp \hat{n}_\perp, z \hat{n}_z) \psi(z \hat{n}_z) | P \rangle}{\sqrt{Z_E(2L + z, b_\perp, a)}}, \quad (3.34)$$

with z and b_\perp being the longitudinal and transverse separations of the quark fields, and \hat{n}_z and \hat{n}_\perp denoting the corresponding unit vectors. The hadron moves with momentum P that has a large component P_z in z -direction, and in the Boer-Mulders case, $|P\rangle$ denotes a unpolarized hadron state. The bare matrix element in the numerator of eq. (3.34) contains a gauge-invariant non-local quark bilinear operator, where two quark fields are connected with a staple-shaped gauge link with extent L running along the z -direction:

$$\mathcal{W}_z(b_\perp \hat{n}_\perp, z \hat{n}_z) = W_z^\dagger(L \hat{n}_z + b_\perp \hat{n}_\perp, b_\perp \hat{n}_\perp) W_\perp(L \hat{n}_z + b_\perp \hat{n}_\perp, L \hat{n}_z) W_z(L \hat{n}_z, z \hat{n}_z). \quad (3.35)$$

The staple is formed by straight Wilson lines W_z along the z -direction and W_\perp along the transverse direction.

Since the time reversal odd Boer-Mulders function exists only due to final state interactions in SIDIS or initial state interactions in the Drell-Yan process, which break the symmetry under time reversal, symmetry-breaking also needs to be introduced in the theoretical definition. This is achieved by the directionality of the staple-shaped gauge link. For straight gauge links

connecting the inserted quark fields, the Boer-Mulders function would vanish [33].

The denominator of eq. (3.34) consists of the vacuum expectation value of a two-dimensional rectangular Euclidean Wilson loop with length $2L + z$ and width b_\perp :

$$\begin{aligned}
Z_E(2L + z, b_\perp, a) &= \frac{1}{N_c} \text{tr} \langle 0 | W_z(0, (2L + z)\hat{n}_z) \\
&\times W_\perp^\dagger((2L + z)\hat{n}_z + b_\perp\hat{n}_\perp, (2L + z)\hat{n}_z) \\
&\times W_z^\dagger(b_\perp\hat{n}_\perp, b_\perp\hat{n}_\perp + (2L + z)\hat{n}_z) W_\perp(b_\perp\hat{n}_\perp, 0) | 0 \rangle.
\end{aligned} \tag{3.36}$$

After performing the limit $L \rightarrow \infty$, the subtracted quasi-Boer-Mulders function in eq. (3.34) does not depend on the length L of the staple. An analysis of the L -dependence will be shown in section 5.4.2.

3.5.2 Renormalization of quasi-TMDPDFs in the short distance ratio scheme

The matrix element in the numerator of eq. (3.34) is a bare quantity which suffers from various divergences. Wilson line self energy leads to linear divergence, while the staple-shaped Wilson link $\mathcal{W}_z(b_\perp\hat{n}_\perp, z\hat{n}_z)$ introduces pinch-pole singularity from the interactions between the two Wilson lines in z -direction. Keeping the length L of the staple-shaped link finite regulates the pinch-pole singularity.

Square root of the rectangular Euclidean Wilson loop

Both the linear divergence and pinch-pole singularity can be eliminated by dividing by the square root of the rectangular Euclidean Wilson loop $Z_E(2L + z, b_\perp, a)$ [133, 134, 135, 92, 136]. In order to properly cancel those divergences, the total length of the rectangular Wilson loop is chosen to be twice the total length of the staple-shaped link used in the definition of the bare matrix element in the numerator of eq. (3.34). The usage of Z_E also gets rid of unwanted contributions from the transverse gauge link W_\perp connecting the two long Wilson lines along the z -direction at the endpoints.

Short distance ratio scheme

However, not all divergences are canceled by the square root of the rectangular Wilson loop Z_E . The subtracted quasi-TMDPDF in eq. (3.34) still suffers from logarithmic UV divergences, which stem from the endpoints of the

Wilson links. Staple-shaped operators can be renormalized multiplicatively [137], and there are different approaches for eliminating the logarithmic divergence. In this thesis, we choose to divide the subtracted quasi-TMDPDF with hadron momentum P_z and longitudinal and transverse separations z and b_\perp of the quark fields by the subtracted quasi-TMDPDF at zero momentum and short distances z_0 and $b_{\perp,0}$ [138]. The renormalized quasi-TMDPDF in coordinate space can then be expressed as

$$\tilde{h}_1^{\perp,\overline{\text{MS}}}(z, b_\perp, P_z, \mu) = \frac{\tilde{h}_1^\perp(z, b_\perp, P_z, a)}{Z_O(z_0, b_{\perp,0}, a, \mu)}, \quad (3.37)$$

where the logarithmic divergence factor Z_O reads

$$Z_O(z_0, b_{\perp,0}, a, \mu) = \frac{\tilde{h}_1^\perp(z_0, b_{\perp,0}, P_z = 0, a)}{\tilde{h}_{1,\text{pert.}}^{\perp,\overline{\text{MS}}}(z_0, b_{\perp,0}, P_z = 0, \mu)}. \quad (3.38)$$

Note that while the singular dependence on the lattice spacing a has been canceled on the l.h.s. of eq. (3.37), lattice artifacts might still be present, and are taken into account by extrapolating to the continuum, see section 5.7.7.

On the r.h.s. of eq. (3.38), the perturbative results $\tilde{h}_{1,\text{pert.}}^{\perp,\overline{\text{MS}}}(z_0, b_{\perp,0}, P_z = 0, \mu)$ are used to convert the renormalized quasi-TMDPDF to the $\overline{\text{MS}}$ scheme [138]. The conversion is necessary since the quasi-TMDPDF will be matched to the light-cone TMDPDF, see section 5.7, and the corresponding factorization formula is only valid in the $\overline{\text{MS}}$ scheme.

The perturbative result $\tilde{h}_{1,\text{pert.}}^{\perp,\overline{\text{MS}}}(z_0, b_{\perp,0}, P_z = 0, \mu)$ on the r.h.s. of eq. (3.38) is given by [138]¹

$$\begin{aligned} \tilde{h}_{1,\text{pert.}}^{\perp,\overline{\text{MS}}}(z_0, b_{\perp,0}, P_z = 0, \mu) = & 1 + \frac{\alpha_S C_F}{2\pi} \left\{ \frac{1}{2} + 3\gamma_E - 3 \ln 2 \right. \\ & \left. + \frac{3}{2} \ln \left[\mu^2 (b_{\perp,0}^2 + z_0^2) \right] - 2 \frac{z_0}{b_{\perp,0}} \arctan \frac{z_0}{b_{\perp,0}} \right\} + \mathcal{O}(\alpha_S^2). \end{aligned} \quad (3.39)$$

Short scales z_0 and $b_{\perp,0}$ have to be chosen in order for perturbation theory to be valid. After conversion to the $\overline{\text{MS}}$ scheme, the dependence of the renormalized quasi-TMDPDF $\tilde{h}_1^{\perp,\overline{\text{MS}}}(z, b_\perp, P_z, z_0, \mu)$ in eq. (3.37) on $b_{\perp,0}$ is canceled, while a dependence on the renormalization scale μ is introduced.

¹The calculation in [138] was carried out for the zero-momentum matrix element with gamma structure $\Gamma = \gamma_t$, giving a result which is independent of the external hadron state. At present, perturbative calculations are performed within LPC to verify that the expression in eq. (3.39) is also valid for $\Gamma = \gamma_1 \gamma_3$.

After converting the renormalized quasi-TMDPDF in $\overline{\text{MS}}$ scheme to momentum space using a Fourier transformation with respect to z , the quasi-TMDPDF satisfies the following RGE [9, 139, 140]

$$\mu^2 \frac{d}{d\mu^2} \ln \tilde{h}_1^{\perp, \overline{\text{MS}}}(x, b_{\perp}, \mu, \zeta_z) = \gamma_F(\alpha_s(\mu)), \quad (3.40)$$

with γ_F being the anomalous dimension for the heavy-light quark current [141, 142, 143]. In eq. (3.40), the explicit dependence on z_0 is dropped, and the dependence on the momentum P_z is replaced by a dependence on the Collins-Soper scale $\zeta_z = (2xP_z)^2$.

Renormalization group resummation²

The perturbative expression for the zero-momentum matrix element in eq. (3.39) fulfills the renormalization group equation [39]

$$\frac{d\tilde{h}_{1,\text{pert.}}^{\perp, \overline{\text{MS}}}(z_0, b_{\perp,0}, 0, \mu)}{d \log \mu} = \gamma_F(\alpha_s(\mu)) \tilde{h}_{1,\text{pert.}}^{\perp, \overline{\text{MS}}}(z_0, b_{\perp,0}, 0, \mu), \quad (3.41)$$

leading to logarithmic terms of the form $\log \left[\mu^2 (b_{\perp,0}^2 + z_0^2) e^{2\gamma_E/4} \right]$ being present up to all orders in perturbation theory in $\tilde{h}_{1,\text{pert.}}^{\perp, \overline{\text{MS}}}$. Depending on the values of μ and the short scales $b_{\perp,0}$ and z_0 , the logarithmic terms become relevant, and resumming them can improve the accuracy of the perturbative result. The renormalization group resummation (RGR) is carried out by solving eq. (3.41), leading to

$$\tilde{h}_{1,\text{pert.}}^{\perp, \overline{\text{MS}}, \text{RGR}}(z_0, b_{\perp,0}, 0, \mu) = \tilde{h}_{1,\text{pert.}}^{\perp, \overline{\text{MS}}}(z_0, b_{\perp,0}, 0, \mu) \exp \left[\int_{\alpha_s(\mu_0)}^{\alpha_s(\mu)} d\alpha' \frac{\gamma_F(\alpha')}{\beta(\alpha')} \right], \quad (3.42)$$

with $\tilde{h}_{1,\text{pert.}}^{\perp, \overline{\text{MS}}}(z_0, b_{\perp,0}, 0, \mu)$ being the fixed-order result given in eq. (3.39) and the physical scale μ_0 that is chosen during resummation. The one-loop, or next-to-leading order (NLO), expressions for the anomalous dimension $\gamma_F(\alpha_s)$ of the heavy-light quark current and beta function $\beta(\alpha_s)$ are given by

$$\begin{aligned} \gamma_F(\alpha_s) &= \gamma_0 \alpha_s + \gamma_1 \alpha_s^2 \\ \beta(\alpha_s) &= \beta_0 \alpha_s^2 + \beta_1 \alpha_s^3. \end{aligned} \quad (3.43)$$

²The work regarding renormalization group resummation which is presented in this thesis was done in close collaboration with Yushan Su, who also developed code for extracting the NLO logarithmic divergence factors with RGR. The results which are presented in section 5.4.3 are produced with code that the author has written, that was double-checked against Yushan Su's code.

For obtaining the resummed renormalization factors presented in section 5.4.3, the coefficients γ_0, γ_1 from [144] and β_0, β_1 from [145] are used.

Since the logarithmic divergence factor in the short distance ratio scheme is obtained using expressions from both lattice QCD and continuum perturbation theory, the following two conditions have to be satisfied for (3.38) giving a valid renormalization factor [41]:

$$\bullet \quad z_0, b_{\perp,0} \ll \frac{1}{\Lambda_{\text{QCD}}} \qquad \bullet \quad b_{\perp,0} \gtrsim a.$$

The first condition ensures that $b_{\perp,0}$ and z_0 are UV scales for perturbation theory to be valid and the second condition is needed so that the dependence of the lattice object on $b_{\perp,0}$ and z_0 can be described by continuum theory. When both conditions are satisfied, the logarithmic divergence factor should only mildly depend on those short scales.

A consistency check is to extract $Z_O(z_0, b_{\perp,0}, a, \mu)$ with different values of $b_{\perp,0}$ and z_0 and try to identify a window where the divergence factor is almost constant. Such a study is shown in section 5.4.3, where the renormalization factors are extracted for various CLS ensembles with and without using RGR for the perturbative expression for the zero-momentum matrix element at NLO.

3.5.3 Momentum evolution equation for quasi-TMD-PDFs

In contrast to light-cone TMDPDFs, whose rapidity divergences were discussed in 3.4.2, quasi-TMDPDFs do not suffer from rapidity divergences, since no light-like gauge links are involved in their definitions. Instead of requiring a separate rapidity regulator as in the light-cone case, the momentum P_z can be viewed as an off-light-cone regulator for the quasi-TMDPDF.

When considering the momentum evolution equation for the quasi-TMD-PDF $\tilde{h}_1^{\perp, \overline{\text{MS}}}$ [9, 139, 140]

$$P_z \frac{d}{dP_z} \ln \tilde{h}_1^{\perp, \overline{\text{MS}}}(x, b_{\perp}, \mu, \zeta_z) = K(b_{\perp}, \mu) + \mathcal{G} \left(\frac{P_z^2}{\mu^2} \right), \quad (3.44)$$

its similarity to the rapidity evolution equation of the light-cone TMD-PDF in eq. (3.31), also called Collins-Soper evolution equation, is apparent. In eq. (3.44), $K(b_{\perp}, \mu)$ is the Collins-Soper kernel, which is independent of the rapidity regularization scheme. The perturbative term $\mathcal{G} \left(\frac{P_z^2}{\mu^2} \right)$ exists only in the off-light-cone scheme.

From eq. (3.44), it is obvious that in order to account for the P_z -dependence of the quasi-TMDPDF, $K(b_\perp, \mu)$ has to be included in the matching to the light-cone TMDPDF at rapidity scale ζ . The non-perturbative Collins-Soper kernel can be calculated on the lattice by considering ratios of quasi-TMDPDFs [146], quasi-TMD wave functions [36, 147] or ratios of Mellin moments of quasi-TMDPDFs [35] at different hadron momenta P_z . At small b_\perp , the Collins-Soper kernel can also be reliably determined from global fits of Drell-Yan and SIDIS data [148, 149].

3.5.4 Off-light-cone soft function

In order for the matching between the quasi-TMDPDF and the light-cone TMDPDF to be valid, rapidity regularization scheme dependence also has to be considered. When using the same scheme for the unsubtracted light-cone TMDPDF and the soft function, the renormalized TMDPDF, which is defined in eq. (3.29), does not depend on the rapidity regularization scheme. In contrast, the renormalized quasi-TMDPDF in eq. (3.37) uses the momentum P_z as an off-light-cone regulator and thus is scheme dependent. To remove this dependence on the rapidity regularization scheme, a Euclidean formulation of the soft function in the same off-light-cone scheme is crucial. This TMD soft function can be extracted using lattice QCD as a form factor of a boosted heavy-quark pair [150] or using a light meson form factor and a quasi-TMD wave function [150, 36, 40]. It is also possible to perturbatively calculate the off-light-cone soft function [151].

At large rapidities, the off-light-cone soft function can be written as [140]

$$S(b_\perp, \mu, Y, Y') = e^{(Y+Y')K(b_\perp, \mu) + \mathcal{D}(b_\perp, \mu)} + \dots, \quad (3.45)$$

where the rapidities of the off-light-cone vectors are denoted by Y and Y' . $K(b_\perp, \mu)$ is the rapidity regularization scheme independent Collins-Soper kernel, which also occurs in the momentum evolution equation of the quasi-TMDPDF given in eq. (3.44), whereas $\mathcal{D}(b_\perp, \mu)$ is the rapidity independent but scheme dependent part. From this, the reduced soft function is defined as

$$S_r(b_\perp, \mu) \equiv e^{-\mathcal{D}(b_\perp, \mu)}. \quad (3.46)$$

In the matching formula between the quasi-TMDPDF and the light-cone TMDPDF, the square root of the intrinsic soft function is used to cancel the dependence on the rapidity regularization scheme, as will be discussed in the following section 3.5.5.

3.5.5 Matching of quasi-TMDPDF to light-cone TMD-PDF

After extracting the quasi-TMDPDF, which was introduced in section 3.5.1, from the lattice using equal-time matrix elements containing a staple-shaped Wilson link, renormalizing the quasi-TMDPDF as described in section 3.5.2, and performing a Fourier transformation to momentum space, the quasi-TMDPDF can be matched to the light-cone.

As argued in sections 3.5.3 and 3.5.4, matching to the light-cone has to include the Collins-Soper kernel $K(b_\perp, \mu)$ and the reduced soft function $S_r(b_\perp, \mu)$. The difference between the regularization scheme independent combination of the renormalized quasi-TMDPDF with the square root of the reduced soft function, and the light-cone TMDPDF evolved to the desired rapidity scale ζ using the Collins-Soper evolution equation, can be calculated perturbatively, leading to the following factorization formula [140, 66]

$$\begin{aligned} \tilde{h}_1^{\perp, \overline{\text{MS}}}(x, b_\perp, \mu, \zeta_z) \sqrt{S_r(b_\perp, \mu)} &= H\left(\frac{\zeta_z}{\mu^2}\right) e^{K(b_\perp, \mu) \frac{1}{2} \ln\left(\frac{\zeta_z}{\mu}\right)} \\ &\times h_1^{\perp'}(x, b_\perp, \mu, \zeta) + \mathcal{O}\left(\frac{\Lambda_{\text{QCD}}^2}{\zeta_z}, \frac{M^2}{\zeta_z}, \frac{1}{b_\perp^2 \zeta_z}\right). \end{aligned} \quad (3.47)$$

Power-corrections are collected in the last term. The perturbative matching kernel $H\left(\frac{\zeta_z}{\mu^2}\right)$ often is written in exponential form as $H = e^h$. At NLO, the kernel reads [151, 152, 66]

$$h^{(1)}\left(\frac{\zeta_z}{\mu^2}\right) = \frac{\alpha_s C_F}{2\pi} \left(-2 + \frac{\pi^2}{12} + \ln\frac{\zeta_z}{\mu^2} - \frac{1}{2} \ln^2\frac{\zeta_z}{\mu^2}\right). \quad (3.48)$$

As seen from eq. (3.48), the light-cone quantity $h_1^{\perp'}(x, b_\perp, \mu, \zeta)$ does not include any dependence on the momentum P_z . The convergence of the results for the light-cone Boer-Mulders function with P_z is studied in section 5.7.3.

After matching the quasi-TMDPDF $\tilde{h}_1^{\perp, \overline{\text{MS}}}(x, b_\perp, \mu, \zeta_z)$ to the light-cone in eq. (3.47), when considering the decomposition of the TMD correlator in position space given in eq. (3.33), one obtains the quantity

$$h_1^{\perp'}(x, b_\perp, \mu, \zeta) \equiv b_\perp m \cdot h_1^\perp(x, b_\perp, \mu, \zeta). \quad (3.49)$$

Thus, dividing the light-cone quantity $h_1^{\perp'}$ by the transverse separation b_\perp and hadron mass m is necessary to extract the Boer-Mulders function h_1^\perp . Note that the factor of i appearing in eq. (3.33) cancels with the additional factor of i being present in the TMD correlator in eq. (3.33) in comparison with the gamma structure $\Gamma = \gamma_1 \gamma_3$ used in this work, see section 5.2.2.

Chapter 4

LaMET calculations for the isovector quark transversity PDF of the nucleon

After giving a short theoretical introduction to parton distribution functions in chapter 3.1 and transverse momentum dependent parton distribution functions in chapter 3.4, and presenting large-momentum effective theory as a method to obtain those distribution functions from the lattice, see chapters 3.2, 3.3 and 3.5, the focus will now lie on the practical calculations to extract PDFs and TMDPDFs with LaMET.

The subject of this chapter is the lattice QCD calculation of the isovector quark transversity distribution $\delta u(x) - \delta d(x)$ of the nucleon in the continuum and physical mass limit with LaMET. The terms nucleon and proton are used interchangeably in the following sections, since the nucleon interpolators will be defined with the quark content of the proton in eq. (4.1). The calculation of $\delta u(x) - \delta d(x)$ is published in [42]. The author of this thesis is one of the main authors of [42], and the project was done in close collaboration with the co-authors. The figures from [42] are taken over with small alterations.

4.1 Gauge ensembles and setup

The CLS gauge ensembles used in the calculation of the quark transversity PDF have been shown in tab. 2.1. These ensembles use the tree-level improved Lüscher-Weisz gauge action and $\mathcal{O}(a)$ -improved Wilson fermion action with $N_f = 2 + 1$ flavors, as introduced in chapter 2.2.2. Four different lattice spacings $a = \{0.098, 0.085, 0.064, 0.049\}$ fm and multiple pion masses between 222 MeV and 354 MeV are employed in order to facilitate a controlled

extrapolation to the continuum and to physical pion mass, see section 4.7.2. Proton momenta up to 2.83 GeV enable taking the infinite momentum limit, which is crucial when working with LaMET.

From each gauge ensemble, 500 configurations are used in the calculations, with the exception of X650, where 1500 configurations are utilized. For the extraction of the zero-momentum matrix elements, which naturally show a larger signal-to-noise ratio compared to non-zero-momentum data, a smaller set of configurations is used for some ensembles, consisting of 350 configurations for H102 and 100 configurations for H105 and N203.

In order to improve the signal-to-noise ratio, two steps of APE smoothing (see 2.3.2) are applied to the gauge fields, as well as momentum smearing of the quark fields, as was discussed in 2.3.2.

4.2 Correlation functions

To extract the matrix element $\bar{h}(z, P_z, 1/a)$, which is included in the quasi-PDF definition in eq. (3.6), from the lattice, correlation functions have to be computed. To establish the correlation functions needed for the isovector quark transversity PDF of the proton, the proton interpolators are defined as follows [47]

$$\begin{aligned}\mathcal{N}_P(x) &= \epsilon_{abc} u_a(x) \left(u_b(x)^T C \gamma_5 d_c(x) \right) \\ \bar{\mathcal{N}}_P(x) &= \epsilon_{a'b'c'} \left(\bar{u}_{b'}(x) C \gamma_5 \bar{d}_{c'}(x)^T \right) \bar{u}_{a'}(x),\end{aligned}\tag{4.1}$$

where up and down quarks are represented by $u(x)$ and $d(x)$, respectively, and $x = (\vec{x}, t)$. The proton quark content is used to form the gauge-invariant interpolators, which are color singlets. The terms in brackets form so-called diquarks, using the charge conjugation matrix C , and the transposition acts on the Dirac indices. The interpolators exhibit one open Dirac index, which is not made explicit in eq. (4.1).

The proton interpolators defined in eq. (4.1) annihilate or create all states which have the same quantum numbers as the proton. Using these interpolators, the two-point and three-point correlation functions can be defined, both of which are necessary to extract the isovector quark transversity PDF of the proton from the lattice.

4.2.1 Two-point correlation function

For the two-point correlation function, a proton is created at space-time point $x_{\text{src}} = (\vec{x}_{\text{src}}, t_{\text{src}})$ and annihilated at space-time point $x_{\text{snk}} = (\vec{x}_{\text{snk}}, t_{\text{snk}})$. With

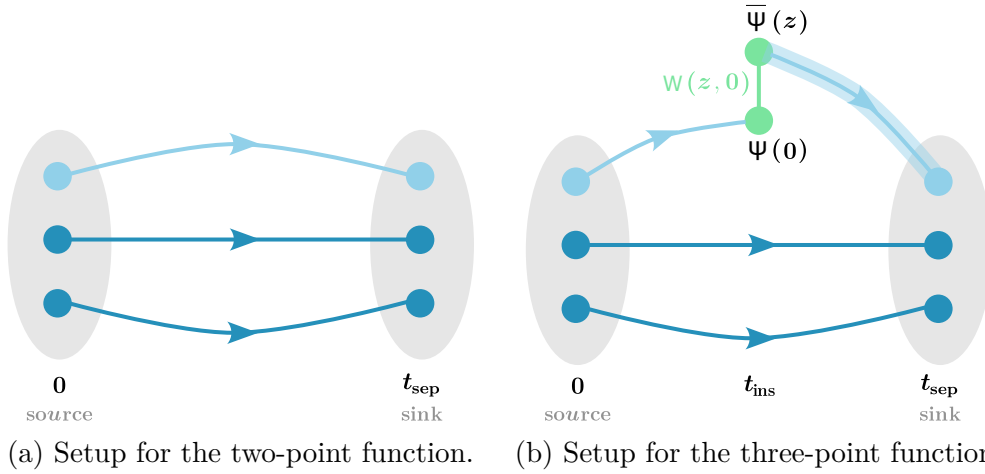


Figure 4.1: Simplified illustration of the lattice setup for calculating the two-point function $C_{2\text{pt}}(P_z, t_{\text{sep}})$ (4.1a) and the three-point function $C_{3\text{pt},\Gamma}(P_z, t_{\text{ins}}, t_{\text{sep}}, z)$ (4.1b) on the lattice. The nucleon source and sink carry momentum P_z in z -direction. Quark propagators are depicted by blue lines, while quark flavors are not made explicit. Fig. 4.1b: The sequential method [59] is applied to calculate the shaded quark propagator. The inserted quark and antiquark fields separated by z and the Wilson line connecting them are shown in green.

the proton interpolators defined as in (4.1), and using the parity projector $P_+ = \frac{1}{2}(\mathbb{1} + \gamma_4)$ to project onto positive parity, the two-point correlation function is written as

$$C_{2\text{pt}}(P_z, t_{\text{sep}}) = a^3 P_+ \sum_{\vec{x}_{\text{snk}}} e^{-i\vec{p}\cdot(\vec{x}_{\text{snk}} - \vec{x}_{\text{src}})} \langle \mathcal{N}_P(x_{\text{snk}}) \bar{\mathcal{N}}_P(x_{\text{src}}) \rangle, \quad (4.2)$$

where the momentum \vec{p} is fixed by the Fourier transformation, and $\vec{p} = (0, 0, P_z)$ only has a non-zero spatial component in z -direction. The two-point function thus depends on P_z and on the temporal separation $t_{\text{sep}} = t_{\text{snk}} - t_{\text{src}}$ of the source and the sink. Setting $t_{\text{src}} = 0$ is possible due to translational invariance and aids to simplify the following calculations.

A simplified illustration of the nucleon two-point function setup on the lattice is shown in fig. 4.1a. The nucleon source and sink carry momentum P_z in z -direction. Quark flavors are not specified, since different contractions lead to different types of diagrams. The contractions which are necessary for the calculation of $C_{2\text{pt}}(P_z, t_{\text{sep}})$ are found using Wick's theorem.

Wick contractions Using Wick's theorem, the two-point correlation function can be expressed in terms of quark propagators:

$$\begin{aligned}
C_{2\text{pt}}(P_z, t_{\text{sep}}) = a^3 P_+ \sum_{\vec{x}_{\text{snk}}} e^{-i\vec{p}\cdot(\vec{x}_{\text{snk}}-\vec{x}_{\text{src}})} \epsilon_{abc} \epsilon_{a'b'c'} (C\gamma_5)^{\beta\gamma} (C\gamma_5)^{\beta'\gamma'} \\
\times D_{cc'}^{\gamma\gamma'}(x_{\text{snk}}, x_{\text{src}}) \left(U_{ab'}^{\alpha\beta'}(x_{\text{snk}}, x_{\text{src}}) U_{ba'}^{\beta\alpha'}(x_{\text{snk}}, x_{\text{src}}) \right. \\
\left. - U_{aa'}^{\alpha\alpha'}(x_{\text{snk}}, x_{\text{src}}) U_{bb'}^{\beta\beta'}(x_{\text{snk}}, x_{\text{src}}) \right), \tag{4.3}
\end{aligned}$$

with $U(x_{\text{snk}}, x_{\text{src}})$ and $D(x_{\text{snk}}, x_{\text{src}})$ being the up and down quark propagators for propagation from the source at position x_{src} to the sink at position x_{snk} . The propagators $U = (D^u)^{-1}$ and $U = (D^d)^{-1}$ are the inverse of the Wilson Dirac operators introduced in eq. (2.15). Details about the calculation of quark propagators on the lattice can be found in section 2.3.1. For the calculations in this project, the Chroma software suite [153] was used, combined with a multigrid solver [57, 58] for inverting the Dirac operator. Additional code needed to calculate the PDF matrix elements was developed by Peng Sun and Xiaonu Xiong. The lattice calculations were performed at the University of Regensburg using the high-performance computer Athene, at the Leibniz Supercomputing Center with SuperMUC-NG, and at the High Performance Computing Center of Central South University in Changsha, China.

The propagator evaluations and contractions in eq. (4.3) are performed on the gauge configurations of the ensembles of interest, see 2.1 for the ensemble parameters. The proton momenta P_z and number of measurements on each configuration are summarized in tab. 4.1.

To obtain the mean and error estimate for the proton two-point function, statistical methods can be applied, see 2.3.3. In this project, binning with bin size 5 is used for X650, while for the other ensembles the data is not binned. Bootstrap resampling with 4000 samples is used to estimate the statistical errors.

Spectral decomposition When inserting a full set of states

$$\mathbb{1} = \sum_n \frac{1}{2E_n} |n\rangle\langle n| \tag{4.4}$$

between the two interpolators in the two-point correlation function in eq. (4.2), using translational invariance and inserting Euclidean time evolution and space translation operators acting on the interpolators, the two-point function can be expressed as

Ensemble	P_z [GeV]	t_{sep}/a	z_{max}/a	$N_{\text{meas.}}/N_{\text{conf.}}$
X650	{0, 1.84, 2.37, 2.63}	{5, 7, 9}	18	1 (run 1)
				2 (run 2)
H102	{0, 1.82, 2.27, 2.73}	{7, 8, 9}	20	2
H105	{0, 1.82}	{7, 8, 9}	20	2
C101	{0, 1.82}	{6, 7, 8, 9}	20	2
		{10, 11, 12}		4
N203	{0, 1.62, 2.02, 2.42, 2.83}	13	30	8
		{14, 15}		16
		{10, 12}		4
N302	{0, 2.09, 2.62}	14	30	8
		{16, 18}		16

Table 4.1: Proton momenta P_z , source-sink separations t_{sep}/a , maximum insertion quark field separation z_{max}/a and number of measurements per configuration for the ensembles used in the calculation for the quark transversity PDF in the proton.

$$\begin{aligned}
C_{2\text{pt}}(P_z, t_{\text{sep}}) &= P_+ \sum_n \frac{e^{-E_n t_{\text{sep}}}}{2E_n} \langle \Omega | \mathcal{N}_P | n \rangle \langle n | \overline{\mathcal{N}}_P | \Omega \rangle \\
&\propto e^{-E_0 t_{\text{sep}}} \left(1 + \mathcal{O} \left(e^{-\Delta E t_{\text{sep}}} \right) \right).
\end{aligned} \tag{4.5}$$

The proton interpolators $\mathcal{N}_P = \mathcal{N}_P(\vec{0}, 0)$, $\overline{\mathcal{N}}_P = \overline{\mathcal{N}}_P(\vec{0}, 0)$ are located at space-time origin. The energy of the vacuum state $|\Omega\rangle$ is set to $E_\Omega = 0$. The approximation in eq. (4.5) assumes a large source-sink separation t_{sep} so that the state with the lowest energy E_0 , which is the proton ground state, exhibits the largest contribution in the spectral decomposition. Excited states are suppressed exponentially at large t_{sep} and are taken into account by the term containing $\Delta E = E_1 - E_0$.

Dispersion relation The proton ground and excited state energies depend on the momentum of the proton. To extract the ground state energy E_0 , a fit of the two-point correlation function with the following two-state fit form, motivated by the spectral decomposition in eq. (4.5), is performed:

$$C_{2\text{pt}}(P_z, t_{\text{sep}}) = c_4(P_z) e^{-E_0(P_z) t_{\text{sep}}} (1 + c_5(P_z) e^{-\Delta E(P_z) t_{\text{sep}}}). \tag{4.6}$$

The two-point function is fitted for every ensemble and proton momentum P_z , and the validity of the continuum dispersion relation

$$E(\vec{p}) = \sqrt{m^2 + \vec{p}^2} \tag{4.7}$$

with hadron mass m is tested by fitting the extracted energies $E_0(P_z)$ with

$$E_0(P_z) = \sqrt{m^2 + c_1 P_z^2 + c_2 a^2 P_z^4}, \tag{4.8}$$

where $m = E(P_z = 0)$. The term which is quadratic in the lattice spacing parametrizes the discretization error. The fit results for the dispersion relation on each ensemble are shown in fig. 4.2, where the error bands are determined by fitting $E_0(P_z)$ with eq. (4.8) for each bootstrap sample and estimating the uncertainty as described in section 2.3.3. The fitted energies agree with the dispersion relation within 3σ .

4.2.2 Three-point correlation function

In order to extract the matrix element $\tilde{h}(z, P_z, 1/a)$ from the lattice, a three-point correlation function has to be evaluated in addition to the two-point

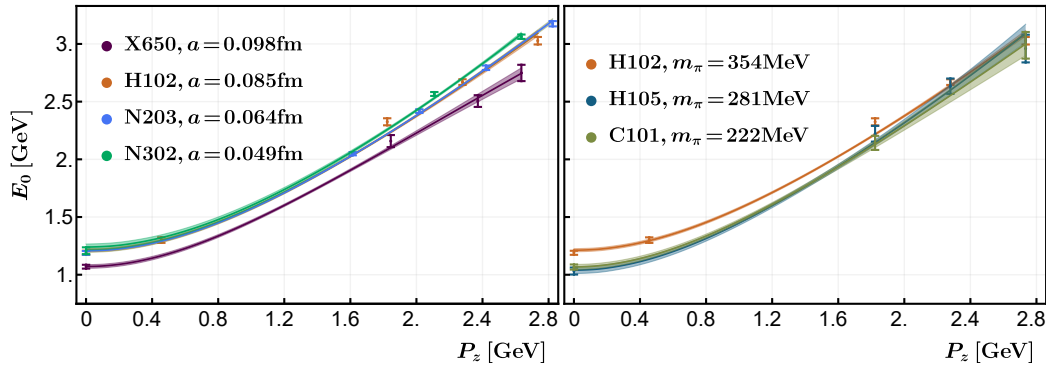


Figure 4.2: Dispersion relation on ensembles X650, H102, N203, N302 with roughly same pion mass of $m_\pi \approx 340$ MeV (left panel) and on ensembles H102, H105, C101 with same lattice spacing $a = 0.085$ fm (right panel) [42].

function defined in eq. (4.2). To obtain the three-point correlator, a proton is created at x_{src} , a non-local current of the form

$$\begin{aligned} \mathcal{O}_\Gamma(x, z) = & \bar{u}_{a''}(x) \Gamma W(x_z, x_z + z) u_{a''}(x + z \hat{n}_z) \\ & - \bar{d}_{a''}(x) \Gamma W(x_z, x_z + z) d_{a''}(x + z \hat{n}_z) \end{aligned} \quad (4.9)$$

is inserted at $x_{\text{ins}} = (\vec{x}_{\text{ins}}, t_{\text{ins}})$, and the proton is destroyed at x_{snk} . The separation of the quark fields in z -direction is denoted as z . The fields are connected with a gauge link $W(x_z, x_z + z)$ in z -direction to ensure gauge invariance. For the extraction of the isovector quark transversity PDF, the isovector combination is used in the inserted current and the gamma structure is chosen as $\Gamma = \gamma^t \gamma^\perp \gamma_5$ with $\perp = x$.

The three-point function is then defined as

$$\begin{aligned} C_{3\text{pt}, \Gamma}(P_z, t_{\text{ins}}, t_{\text{sep}}, z) = & a^6 P_\perp \sum_{\vec{x}_{\text{snk}}, \vec{x}_{\text{ins}}} e^{-i\vec{p} \cdot (\vec{x}_{\text{snk}} - \vec{x}_{\text{src}})} \\ & \times \langle \mathcal{N}_P(x_{\text{snk}}) \mathcal{O}_\Gamma(x_{\text{ins}}, z) \bar{\mathcal{N}}_P(x_{\text{src}}) \rangle \end{aligned}, \quad (4.10)$$

with $P_\perp = -\mathbf{1}(\gamma_2 \gamma_3 + \gamma_1 \gamma_5)/2$ being the polarization operator for transverse polarization in x -direction. A signal for the three-point correlation function is only given for operator insertion times between the temporal positions of source and sink, i.e. $t_{\text{src}} < t_{\text{ins}} < t_{\text{snk}}$.

A simplified illustration of the lattice setup for calculating the nucleon three-point function $C_{3\text{pt}, \Gamma}(P_z, t_{\text{ins}}, t_{\text{sep}}, z)$ is shown in fig. 4.1b. The nucleon source and sink carry momentum P_z in z -direction. The sequential method [59], see section 2.3.1, is applied to calculate the shaded quark propagator.

The inserted quark and antiquark fields with longitudinal separation z in z -direction are depicted in green with a gauge link connecting them. Quark flavors are not made explicit, since different types of diagrams result from the Wick contractions.

Wick contractions Analogously to the two-point function, the three-point function can be expressed using quark propagators by applying Wick's theorem. The expression for the isovector case is derived by considering the up and down quark current insertion separately.

Starting with the up quark insertion, i.e. inserting the non-local current

$$\mathcal{O}_{\Gamma,u}(x, z) = \bar{u}_a''(x)\Gamma W(x_z, x_z + z)u_a''(x + z\hat{n}_z) \quad (4.11)$$

in the three-point function

$$\begin{aligned} C_{3\text{pt},\Gamma}^u(P_z, t_{\text{ins}}, t_{\text{sep}}, z) &= a^6 P_{\perp} \sum_{\vec{x}_{\text{snk}}, \vec{x}_{\text{ins}}} e^{-i\vec{p}\cdot(\vec{x}_{\text{snk}}-\vec{x}_{\text{src}})} \epsilon_{abc}\epsilon_{a'b'c'} \\ &\times (C\gamma_5)^{\beta\gamma} (C\gamma_5)^{\beta'\gamma'} \langle u_a^\alpha(x_{\text{snk}})u_b^\beta(x_{\text{snk}})d_c^\gamma(x_{\text{snk}})\bar{d}_{a''}^{\alpha'}(x_{\text{ins}})\Gamma \\ &\times W(z_{\text{snk}}, z_{\text{src}})d_{a''}^{\alpha''}(x_{\text{ins}} + z\hat{n}_z)\bar{u}_{b'}^{\beta'}(x_{\text{src}})\bar{d}_{c'}^{\gamma'}(x_{\text{src}})\bar{u}_{a'}^{\alpha'}(x_{\text{src}})\rangle, \end{aligned} \quad (4.12)$$

and performing the Wick contractions, leads to

$$\begin{aligned} C_{3\text{pt},\Gamma}^u(P_z, t_{\text{ins}}, t_{\text{sep}}, z) &= a^6 P_{\perp} \sum_{\vec{x}_{\text{snk}}, \vec{x}_{\text{ins}}} e^{-i\vec{p}\cdot(\vec{x}_{\text{snk}}-\vec{x}_{\text{src}})} \epsilon_{abc}\epsilon_{a'b'c'} (C\gamma_5)^{\beta\gamma} (C\gamma_5)^{\beta'\gamma'} \\ &\times D_{cc'}^{\gamma\gamma'}(x_{\text{snk}}, x_{\text{src}}) \\ &\times \left(U_{aa''}^{\alpha\alpha''}(x_{\text{snk}}, x_{\text{ins}})\Gamma W(z_{\text{snk}}, z_{\text{src}})U_{a''b'}^{\alpha''\beta'}(x_{\text{ins}} + z\hat{n}_z, x_{\text{src}})U_{ba'}^{\beta\alpha'}(x_{\text{snk}}, x_{\text{src}}) \right. \\ &+ U_{ab'}^{\alpha\beta'}(x_{\text{snk}}, x_{\text{src}})U_{ba''}^{\beta\alpha''}(x_{\text{snk}}, x_{\text{ins}})\Gamma W(z_{\text{snk}}, z_{\text{src}})U_{a''a'}^{\alpha''\alpha'}(x_{\text{ins}} + z\hat{n}_z, x_{\text{src}}) \\ &- U_{aa''}^{\alpha\alpha''}(x_{\text{snk}}, x_{\text{ins}})\Gamma W(z_{\text{snk}}, z_{\text{src}})U_{a''a'}^{\alpha''\alpha'}(x_{\text{ins}} + z\hat{n}_z, x_{\text{src}})U_{bb'}^{\beta\beta'}(x_{\text{snk}}, x_{\text{src}}) \\ &- U_{aa'}^{\alpha\alpha'}(x_{\text{snk}}, x_{\text{src}})U_{ba''}^{\beta\alpha''}(x_{\text{snk}}, x_{\text{ins}})\Gamma W(z_{\text{snk}}, z_{\text{src}})U_{a''b'}^{\alpha''\beta'}(x_{\text{ins}} + z\hat{n}_z, x_{\text{src}}) \\ &\left. + \text{disconnected contributions} \right). \end{aligned} \quad (4.13)$$

In the case of eq. (4.13), where a non-local operator has been inserted, disconnected contributions consist of quark propagators which describe propagation from x_{ins} to $x_{\text{ins}} + z\hat{n}_z$, i.e. they start and end at the same t_{ins} . Since isospin symmetry is used, i.e. $m_u = m_d$, propagators for up and down quark

do not differ from each other, and those contributions cancel when calculating the isovector combination. The Wick contractions for the down quark insertion with the non-local current

$$\mathcal{O}_{\Gamma,d}(x, z) = \bar{d}_a''(x)\Gamma W(x_z, x_z + z)d_a''(x + z\hat{n}_z) \quad (4.14)$$

are performed analogously, but contain less terms, since for the proton there is only one d quark line where the current can be inserted. The resulting three-point function expressed in terms of quark propagators is

$$\begin{aligned} C_{3\text{pt},\Gamma}^d(P_z, t_{\text{ins}}, t_{\text{sep}}, z) &= a^6 P_{\perp} \sum_{\vec{x}_{\text{snk}}, \vec{x}_{\text{ins}}} e^{-i\vec{p}\cdot(\vec{x}_{\text{snk}} - \vec{x}_{\text{src}})} \epsilon_{abc} \epsilon_{a'b'c'} (C\gamma_5)^{\beta\gamma} (C\gamma_5)^{\beta'\gamma'} \\ &\times D_{ca''}^{\gamma\alpha''}(x_{\text{snk}}, x_{\text{ins}})\Gamma W(z_{\text{snk}}, z_{\text{src}})D_{a''c'}^{\alpha''\gamma'}(x_{\text{ins}} + \hat{n}_z, x_{\text{src}}) \\ &\times \left(U_{ab'}^{\alpha\beta'}(x_{\text{snk}}, x_{\text{src}})U_{ba'}^{\beta\alpha'}(x_{\text{snk}}, x_{\text{src}}) - U_{aa'}^{\alpha\alpha'}(x_{\text{snk}}, x_{\text{src}})U_{bb'}^{\beta\beta'}(x_{\text{snk}}, x_{\text{src}}) \right) \\ &+ \text{disconnected contributions.} \end{aligned} \quad (4.15)$$

The isovector three-point function is constructed as

$$C_{3\text{pt},\Gamma}^{u-d}(P_z, t_{\text{ins}}, t_{\text{sep}}, z) = C_{3\text{pt},\Gamma}^u(P^z, t_{\text{ins}}, t_{\text{sep}}, z) - C_{3\text{pt},\Gamma}^d(P^z, t_{\text{ins}}, t_{\text{sep}}, z). \quad (4.16)$$

The source-sink separations t_{sep}/a and maximum separation z_{max}/a of the inserted quark fields used for the calculation of $C_{3\text{pt},\Gamma}^{u-d}(P_z, t_{\text{ins}}, t_{\text{sep}}, z)$ on various gauge ensembles are listed in tab. 4.1. For the ensembles N203 and N302 with smaller lattice spacings, the number of measurements is increased for large source-sink separations to achieve a better signal-to-noise ratio.

Spectral decomposition Similar as for the two-point function, the spectral decomposition can be performed for the three-point function defined in eq. (4.10) by inserting two full sets of states:

$$\begin{aligned} C_{3\text{pt}}(P_z, t_{\text{ins}}, t_{\text{sep}}, z) &= P_{\perp} \sum_{n,m} \frac{e^{-E_n t_{\text{sep}}} e^{-(E_m - E_n) t_{\text{ins}}}}{4E_n E_m} \\ &\times \langle \Omega | \mathcal{N}_P | n \rangle \langle n | \mathcal{O}_{\Gamma} | m \rangle \langle m | \overline{\mathcal{N}}_P | \Omega \rangle. \end{aligned} \quad (4.17)$$

When defining overlap factors as

$$\mathcal{A}_n = \langle \Omega | \mathcal{N}_P | n \rangle, \mathcal{A}_n^* = \langle n | \overline{\mathcal{N}}_P | \Omega \rangle, \quad (4.18)$$

and considering one generic excited state in addition to the proton ground state, i.e. setting $n = 0, 1$ and $m = 0, 1$, the three-point correlation function becomes

$$\begin{aligned}
C_{3\text{pt}}(P_z, t_{\text{ins}}, t_{\text{sep}}, z) = & |\mathcal{A}_0|^2 \langle 0 | \mathcal{O}_\Gamma | 0 \rangle e^{-E_0 t_{\text{sep}}} + |\mathcal{A}_1|^2 \langle 1 | \mathcal{O}_\Gamma | 1 \rangle e^{-E_1 t_{\text{sep}}} \\
& + \mathcal{A}_0 \mathcal{A}_1^* \langle 0 | \mathcal{O}_\Gamma | 1 \rangle e^{-E_0(t_{\text{sep}} - t_{\text{ins}})} e^{-E_1 t_{\text{ins}}} \\
& + \mathcal{A}_1 \mathcal{A}_0^* \langle 1 | \mathcal{O}_\Gamma | 0 \rangle e^{-E_1(t_{\text{sep}} - t_{\text{ins}})} e^{-E_0 t_{\text{ins}}}.
\end{aligned} \tag{4.19}$$

For simplicity, the polarization operator is dropped in eq. (4.19). The energies in eq. (4.17) and eq. (4.19) exhibit a dependence on P_z , which is not made explicit.

4.3 Extraction of the ground state matrix element

The ground state matrix element necessary to extract the proton's isovector quark transversity PDF is denoted by $\langle 0 | \mathcal{O}_\Gamma | 0 \rangle$ in (4.19), and is equal to $\bar{h}(z, P_z, 1/a)$ in the definition of the quasi-PDF in eq. (3.6). To access $\bar{h}(z, P_z, 1/a)$ from the two-point and three-point function data, the ratio

$$R_\Gamma(P_z, t_{\text{ins}}, t_{\text{sep}}, z) = \frac{C_{3\text{pt}}(P_z, t_{\text{ins}}, t_{\text{sep}}, z)}{C_{2\text{pt}}(P_z, t_{\text{sep}})} \tag{4.20}$$

is evaluated and a combined fit with the two-point function is performed. The fit function to approximate $C_{2\text{pt}}(P_z, t_{\text{sep}})$ is given in (4.6), and the two-state fit function for the ratio $R_\Gamma(P_z, t_{\text{ins}}, t_{\text{sep}}, z)$ can be derived by considering the spectral decomposition of the two- and three-point functions:

$$R_\Gamma(P_z, t_{\text{ins}}, t_{\text{sep}}, z) = \frac{c_0 + c_1 \left[e^{-\Delta E(t_{\text{sep}} - t_{\text{ins}})} + e^{-\Delta E t_{\text{ins}}} \right] + c_3 e^{-\Delta E t_{\text{sep}}}}{1 + c_5 e^{-\Delta E t_{\text{sep}}}}. \tag{4.21}$$

The ground state matrix element $\bar{h}(z, P_z, 1/a)$ is denoted by c_0 in eq. (4.21), where for better readability the dependence of the fit parameters c_0, c_1, c_3, c_5 and ΔE on the lattice spacing a , momentum P_z and longitudinal distance z is not made explicit. Note that the fit of $R_\Gamma(P_z, t_{\text{ins}}, t_{\text{sep}}, z)$ is performed for each value of z individually, leading to the z -dependence of all parameters. The dependence of c_5 and ΔE on z is only weak, since those parameters are mainly fixed from the two-point function due to its data

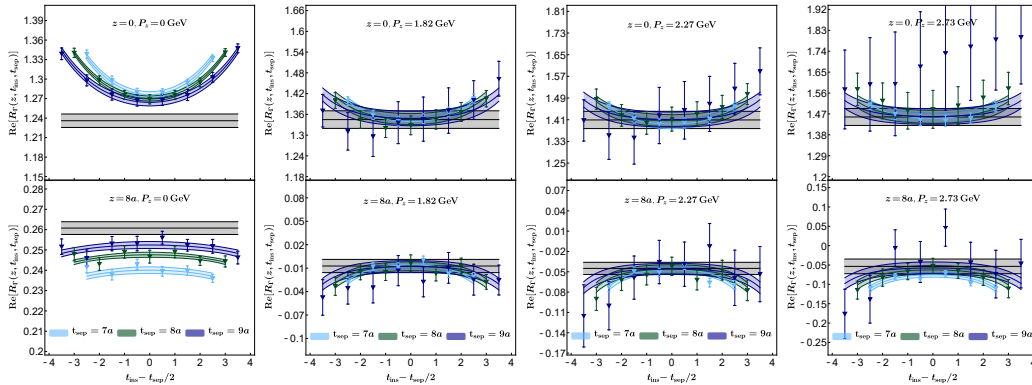


Figure 4.3: Examples for fitting the ratio $R_\Gamma(P_z, t_{\text{ins}}, t_{\text{sep}}, z)$ to extract the ground state matrix element $\bar{h}(z, P_z, 1/a)$. Shown are the results for the real part of $R_\Gamma(P_z, t_{\text{ins}}, t_{\text{sep}}, z)$ for the ensemble H102 with momenta $P_z = \{0, 1.82, 2.27, 2.73\}$ GeV and $z = \{0, 8\}a$ [42].

points having smaller errors and hence larger weights when constructing χ^2 , see section 2.3.4.

To suppress excited state contributions, the source-sink separations t_{sep} have to be as large as possible. However, the signal-to-noise ratio decays with increasing t_{sep} . To check whether excited state contamination is under control, the matrix elements were fitted with different sets of source-sink separations, leading to results that are consistent in statistical errors.

An example for fits of the ground state matrix element is shown in fig. 4.3, where fits of the real part of the ratio $R_\Gamma(P_z, t_{\text{ins}}, t_{\text{sep}}, z)$ are depicted for the ensemble H102 with momenta $P_z = \{0, 1.82, 2.27, 2.73\}$ GeV and $z = \{0, 8\}a$. Due to increased errors of the ratio $R_\Gamma(P_z, t_{\text{ins}}, t_{\text{sep}}, z)$ for larger source-sink separations t_{sep} , these data points have less impact on the fits.

Since the fits performed to extract the ground state matrix element take correlations into account by minimizing χ^2 as defined in eq. (2.40), $\chi^2/\text{d.o.f.}$ is a measure of the fit quality. Fig. 4.4 shows the histogram distribution of $\chi^2/\text{d.o.f.}$ for all combined two-state fits of the ratio $R_\Gamma(P_z, t_{\text{ins}}, t_{\text{sep}}, z)$ and the two-point function $C_{2\text{pt}}(P_z, t_{\text{sep}})$. The distribution from combining all ensembles is depicted in addition to plotting the histograms for each ensemble individually. The distributions are normalized so that the area underneath each curve is 1. The values of $\chi^2/\text{d.o.f.}$ are close to 1, indicating a high fit quality, see section 2.3.4.

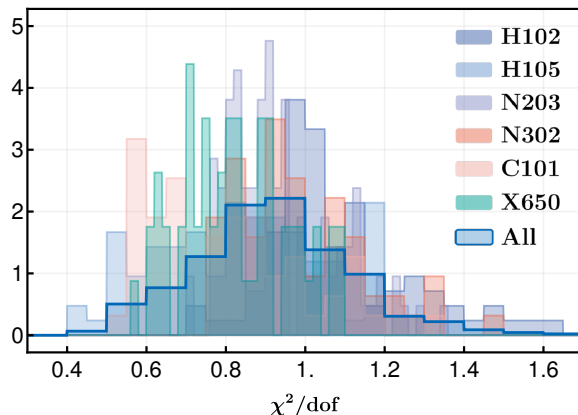


Figure 4.4: Histograms of the $\chi^2/\text{d.o.f.}$ of all combined two-state fits of ratio and two-point function to extract the ground state matrix elements. The distributions are shown for all ensembles individually, as well as combined, and are normalized so that the area underneath each curve is 1 [42].

4.4 Nucleon isovector tensor charge

As a consistency check, the isovector nucleon tensor charge g_T is extracted from the bare matrix elements obtained in this work. The tensor charge is equal to the first Mellin moment of the transversity PDF and can be written as

$$g_T \equiv g_T^u - g_T^d = Z_T \frac{\langle PS_\perp | \bar{u}(0) \gamma^t \gamma^\perp \gamma_5 u(0) - \bar{d}(0) \gamma^t \gamma^\perp \gamma_5 d(0) | PS_\perp \rangle}{\langle PS_\perp | PS_\perp \rangle}, \quad (4.22)$$

where the bare local matrix elements were extracted as described in the previous section. The renormalization factors Z_T are calculated in [82] for all CLS ensembles used in this project, except for X650, which in turn is excluded from the determination of g_T . Since the definition of g_T is Lorentz-invariant, local matrix elements with zero-momentum as well as non-zero momenta are included in the extraction of g_T . The non-zero momenta used to obtain g_T are $P_z^{\text{max}} = 2.73 \text{ GeV}$ for H102, $P_z^{\text{max}} = 1.82 \text{ GeV}$ for H105, $P_z^{\text{max}} = 1.82 \text{ GeV}$ for C101, $P_z^{\text{max}} = 2.83 \text{ GeV}$ for N203 and $P_z^{\text{max}} = 2.62 \text{ GeV}$ for N302.

The resulting values $\tilde{g}_T(a, m_\pi, P_z)$ are extrapolated to the continuum and physical pion mass with [82]

$$\tilde{g}_T(a, m_\pi, P_z) = \bar{g}_T + c_1 m_\pi^2 + c_2 m_{\pi, \text{phys}}^2 \ln m_{\pi, \text{phys}} + c_3 a^2 + c_4 a^2 P_z^2. \quad (4.23)$$

The term $a^2 P_z^2$ is included to account for discretization effects from the matrix elements with non-zero momenta. The extrapolated result is

$$g_T = \bar{g}_T + c_1 m_\pi^2 + c_2 m_{\pi,\text{phys}}^2 \ln m_{\pi,\text{phys}}, \quad (4.24)$$

and is given by $g_T = 1.018(68)$ in this work. The result is in good agreement with the Mainz19 [82], FLAG21 [85] result of $g_T = 0.965(61)$ and recent results from other groups [86, 84, 83].

4.5 Renormalization in the hybrid scheme¹

After obtaining the bare ground state matrix elements $\bar{h}(z, P_z, 1/a)$ by fitting two-point and three-point correlation functions, the matrix elements are renormalized non-perturbatively in the hybrid scheme like described in section 3.3.2. As in eq. (3.14), the bare matrix elements are renormalized separately for short and long distances z . For short distances $|z| < z_s$, the inverse of the bare proton matrix elements at $P_z = 0$ is used as renormalization factor, combined with normalization with the local bare matrix element. The distance z_s separating short and long distances is chosen as $z_s = 0.3$ fm and varied down to a value of $z_s = 0.18$ fm to include systematic uncertainties from the choice of z_s .

Renormalization factors for short distances

The bare matrix elements $\bar{h}(z, P_z = 0, 1/a)$, whose inverse is used for renormalization at short distances, are shown in fig. 4.5 for the gauge ensembles X650, H102, N203 and N302. The imaginary parts are consistent with zero.

Renormalization factors for long distances

To renormalize the matrix elements at long distances $|z| > z_s$, the self renormalization factor $Z_R(z, 1/a)$, which was introduced in eq. (3.16), is extracted. In order to better follow the steps of the calculation, the reader is reminded of the definition of $Z_R(z, 1/a)$:

$$Z_R(z, 1/a) = \frac{\tilde{h}(z, 1/a)}{\tilde{h}_R(z)} \quad (4.25)$$

$$\tilde{h}_R(z) = \exp[g(z) - m_0 z] = \exp[g_0(z)],$$

¹The renormalization in this section was performed within LPC, mainly by Fei Yao, and is presented for completeness.

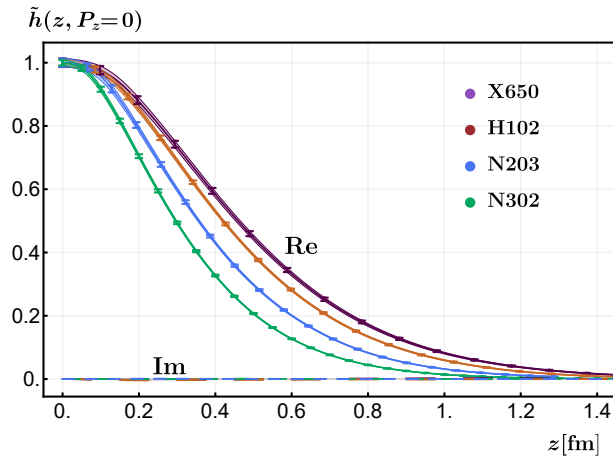


Figure 4.5: Real and imaginary parts of the bare matrix elements at $P_z = 0$ for the gauge ensembles X650, H102, N203 and N302 [42].

where the normalization $\tilde{h}(z, P_z, 1/a) = \bar{h}(z, P_z, 1/a)/\bar{h}(z = 0, P_z, 1/a)$ is used. The self renormalization factor is determined in two steps, where in the first step $g(z)$ is obtained by fitting the a -dependence of the bare nucleon transversity matrix elements in the rest frame with the functional form given in eq. (3.17) for different values of z . Fig. 4.6 shows the lattice data for the bare matrix elements at $P_z = 0$ at various values of z and different lattice spacings, as well as the fit result from fitting with eq. (3.17). The result for the parameter k is $k = 4.35(20) \text{ GeV}^{-1} \text{ fm}^{-1}$. In order to include higher-order perturbative effects and remaining lattice artifacts, d and Λ_{QCD} are also treated as fit parameters [95]. The parameter Λ_{QCD} is tuned for the best fit and set to $\Lambda_{\text{QCD}} = 0.1 \text{ GeV}$. Since the parameter d is tuned in the second step of the self renormalization procedure, its value is not quoted at this point. Using eq. (3.17), $g(z)$ is obtained.

The second step in the self renormalization process is the determination of m_0 . Due to the condition $g(z) - \log Z_{\overline{\text{MS}}}(z) = m_0 z$ from eq. (3.19), m_0 can be obtained by subtracting the continuum short distance perturbative renormalization factor in the $\overline{\text{MS}}$ scheme from $g(z)$ and fitting with $m_0 z + b$. By tuning d in eq. (3.17), $|b|$ is minimized. The fit for the determination of m_0 is depicted in fig. 4.7, where the data points $g(z) - \log Z_{\overline{\text{MS}}}(z)$ as well as the fit result from fitting with $m_0 z + b$ are shown in the small- z region. The resulting parameters are $m_0 = 0.560(85) \text{ fm}^{-1}$, $d = -0.066(70)$ and $b = -0.0015(140)$.

To show that the renormalized matrix element $\tilde{h}_R(z)$ is equal to the continuum perturbative $\overline{\text{MS}}$ result $Z_{\overline{\text{MS}}}(z)$ at short distances z , both quantities are plotted in fig. 4.8. The renormalized lattice matrix elements at $P_z = 0$

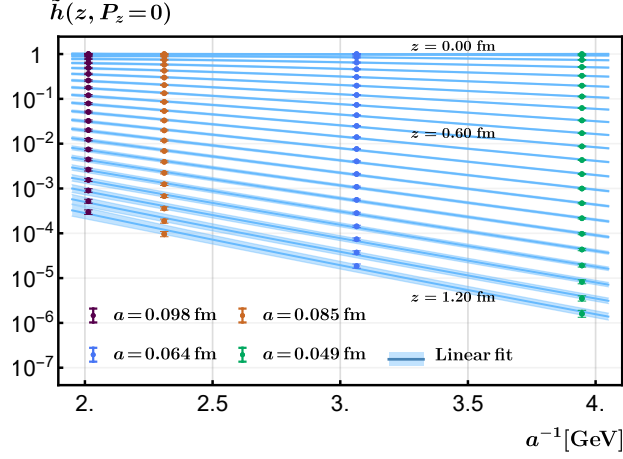


Figure 4.6: Fit of the bare nucleon transversity matrix elements at $P_z = 0$ with eq. (3.17). The bare matrix elements from the lattice calculation at different lattice spacings and values of z are represented by colored data points. The fit result with parameters $k = 4.350(20) \text{ GeV}^{-1} \text{ fm}^{-1}$ and $\Lambda_{\text{QCD}} = 0.1 \text{ GeV}$ is shown as blue bands [42].

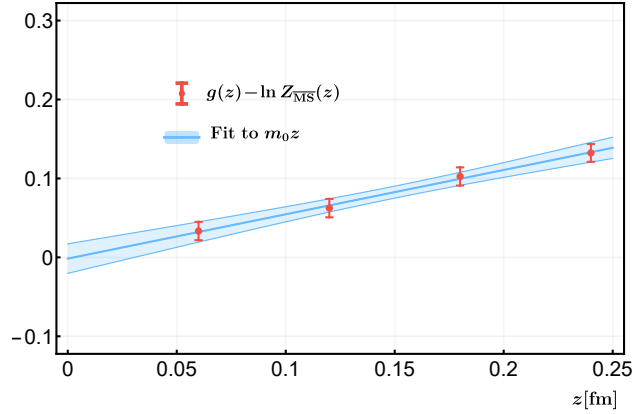


Figure 4.7: Fit for determination of m_0 . The red data points are $g(z) - \log Z_{\overline{\text{MS}}}(z)$, and the blue band shows the fit with $m_0 z + b$. The resulting fit parameters are $m_0 = 0.560(85) \text{ fm}^{-1}$, $d = -0.66(7)$ and $b = -0.0015(140)$ [42].

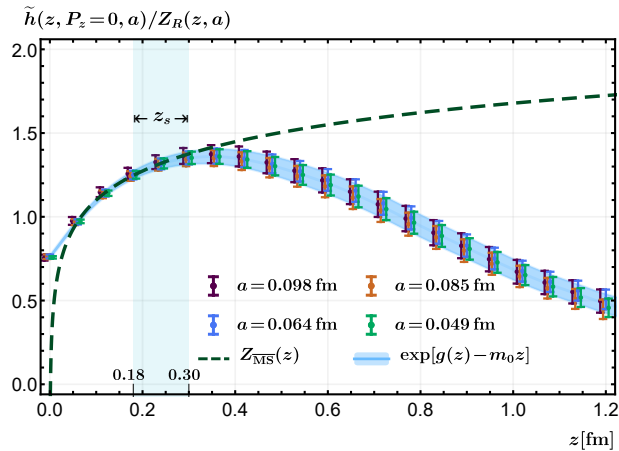


Figure 4.8: Renormalized lattice matrix element $\tilde{h}_R(z) = \tilde{h}(z, 1/a)/Z_R(z, 1/a)$ at zero momentum for various lattice spacings and values of z , depicted as colored points, together with a blue band showing $\exp[g(z) - m_0 z]$ evaluated with the results of the fits described in section 4.5. The perturbative one-loop result $Z_{\overline{\text{MS}}}(z)$ is shown as dashed line and agrees well with $\tilde{h}_R(z)$ at short distances, except for very small z , where discretization effects gain importance [42].

are depicted for various lattice spacings, as well as $\exp[g(z) - m_0 z]$ evaluated with the results of the fits described in this section, and $Z_{\overline{\text{MS}}}(z)$ at one-loop. The range of z in which z_s is varied is shaded in blue. From the figure it is evident that the renormalized matrix element agrees well with the continuum $\overline{\text{MS}}$ result at short distances, except for very small z , where discretization effects come into force.

Lattice results for renormalized quasi-LF correlations

After extracting the renormalization factors for short and long distances separately, the bare matrix elements can be renormalized. The renormalization scale is chosen as $\mu = 2 \text{ GeV}$. The resulting renormalized quasi-LF correlations for the ensembles X650, H102, N203 and N302 with almost equal pion mass are shown in fig. 4.9 as a function of the quasi-LF distance $\lambda = zP_z$. Both real and imaginary parts of the renormalized matrix elements $\tilde{h}_R(\lambda, P_z)$ are depicted for various values of the nucleon momentum P_z . As is apparent from the figure, the convergence with increasing P_z is good. However, excited-state contamination becomes more pronounced with increasing nucleon momentum, leading to larger uncertainties. Due to substantial uncertainties, especially compared to the other data sets, the $P_z = 2.63 \text{ GeV}$ data

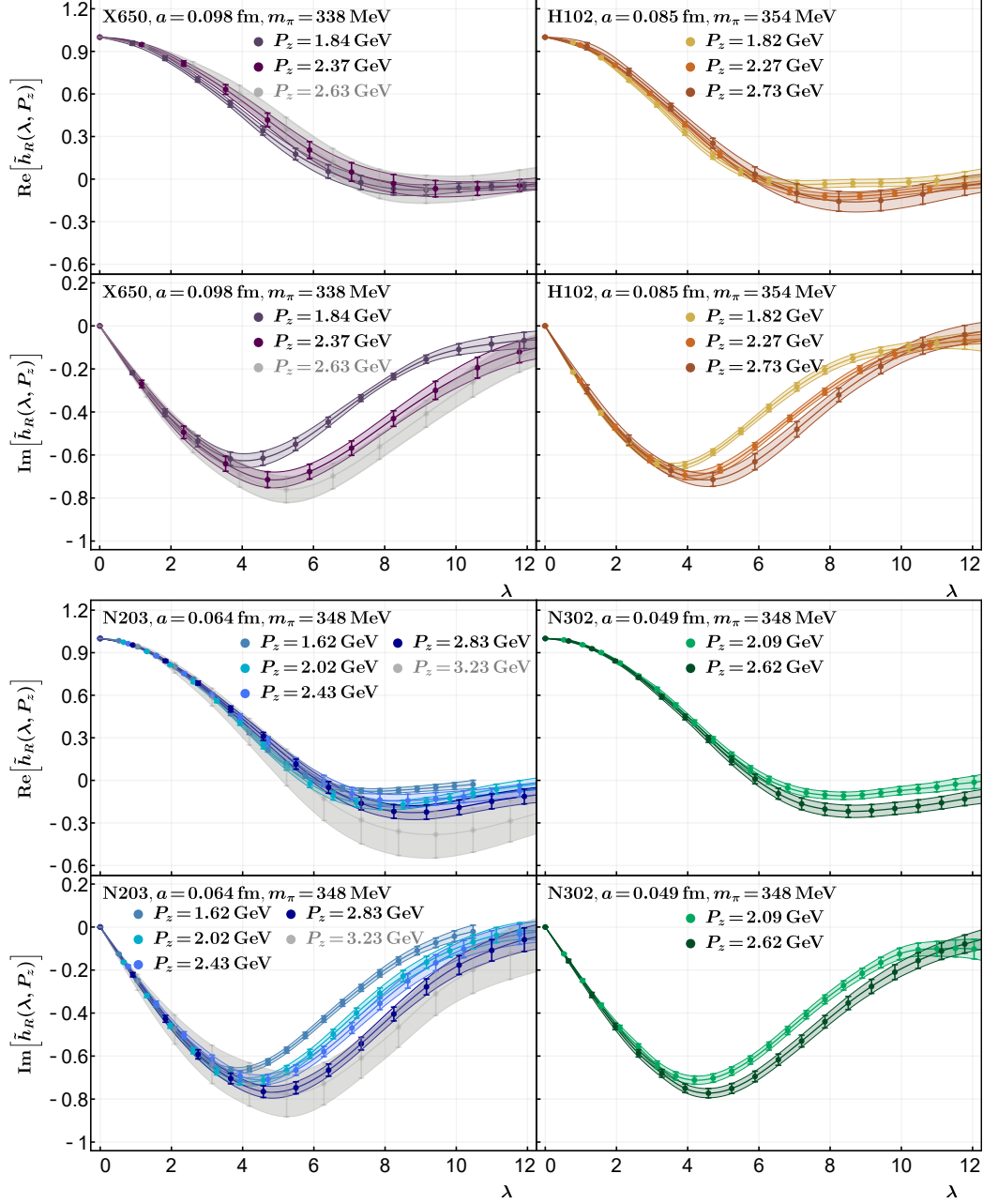


Figure 4.9: Real and imaginary parts of the renormalized matrix elements $\hat{h}_R(\lambda, P_z)$ at renormalization scale $\mu = 2$ GeV as a function of the quasi-LF distance $\lambda = zP_z$. Shown are the ensembles X650, H102, N203 and N302 with nearly the same pion mass [42].

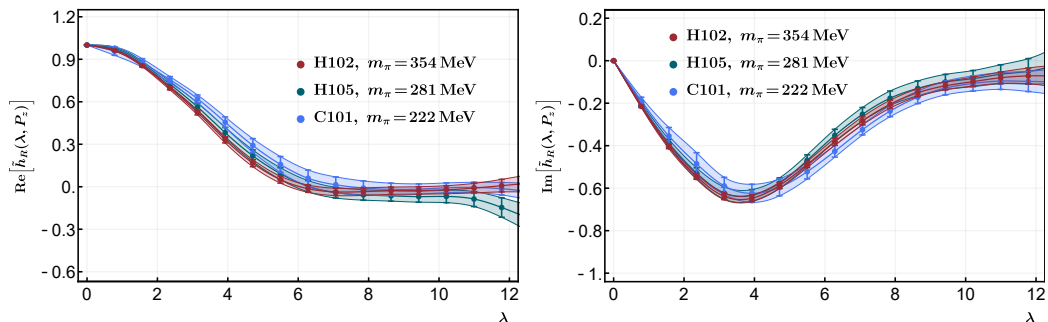


Figure 4.10: Real and imaginary parts of the renormalized matrix elements $\tilde{h}_R(\lambda, P_z)$ at renormalization scale $\mu = 2$ GeV as a function of the quasi-LF distance $\lambda = zP_z$. The data is shown for the ensembles H102, H105 and C101 with the same lattice spacing $a = 0.085$ fm. The nucleon momentum is $P_z = 1.82$ GeV [42].

of X650 as well as $P_z = 3.23$ GeV data of N203 is excluded from the further analysis.

To investigate the pion mass dependence of the renormalized quasi-LF correlations, $\tilde{h}_R(\lambda, P_z)$ at $P_z = 1.82$ GeV is shown in fig. 4.10 for the ensembles H102, H105 and C101 with pion masses of $m_\pi = \{354, 281, 222\}$ MeV and $a = 0.085$ fm. The renormalized results exhibit only a very minor dependence on the pion mass.

4.6 Extrapolation for large quasi-LF distances

For matching the renormalized quasi-LF correlations to the light-cone, it is necessary to perform a Fourier transformation to momentum space, which requires $\tilde{h}_R(\lambda, P_z)$ at all distances λ . It is clearly visible in fig. 4.9 and fig. 4.10 that the errors of the renormalized quasi-LF correlations increase at large λ . Fourier transforming the data after a simple truncation would lead to unphysical oscillations in momentum space.

To circumvent this problem, the renormalized matrix elements calculated on the lattice are supplemented with an extrapolation for large quasi-LF distances λ . The extrapolation form [92]

$$\tilde{h}_R(\lambda, P_z) = \left[\frac{c_1}{(i\lambda)^a} + e^{-i\lambda} \frac{c_2}{(-i\lambda)^b} \right] e^{-\lambda/\lambda_0} \quad (4.26)$$

contains algebraic terms to reflect the power law behavior in the end point region, as well as an exponential term accounting for the expected finite correlation length λ_0 at finite momentum. A large enough region $\lambda \geq \lambda_L$

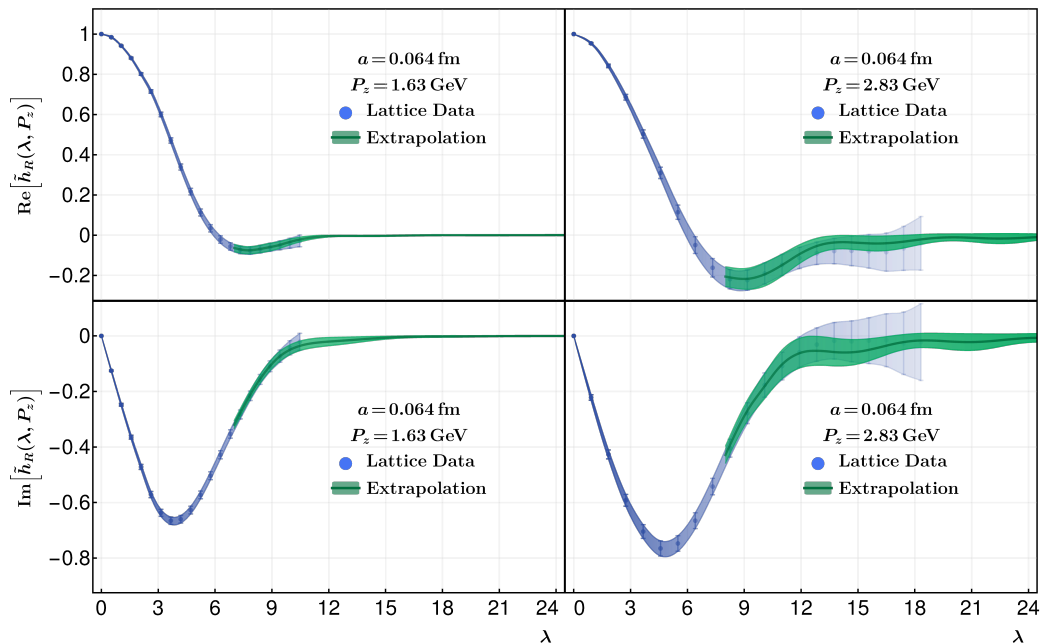


Figure 4.11: Renormalized lattice matrix elements $\tilde{h}_R(\lambda, P_z)$ for N203 with $P_z = 1.63$ GeV (blue data, left column) and $P_z = 2.83$ GeV (blue data, right column) together with the results from extrapolating with eq. (4.26) (green curves). The extrapolation shows good agreement with the lattice data in the moderate- λ region and gives smooth curves with reduced errors in the large- λ region [42].

with truncation value λ_L has to be selected in order to reliably determine the extrapolation parameters c_1 , c_2 , a , b and λ_0 . Since the extrapolation is performed individually for each lattice spacing, pion mass and momentum, all parameters depend on a , m_π and P_z . For the sake of simplicity, these dependencies are omitted in eq. (4.26).

As an example, fig. 4.11 shows the extrapolation of the renormalized matrix elements $\tilde{h}_R(\lambda, P_z)$ for N203 at $P_z = 1.63$ GeV (left column) and $P_z = 2.83$ GeV (right column). The truncation value is chosen as $\lambda_L = 7$ and varied down to $\lambda_L = 4$ for an approximation of the systematic error from the fit with eq. (4.26). The extrapolation results agree well with the renormalized lattice matrix elements in the region of moderately large λ and yield a smooth curve with reduced errors in the large- λ region.

The extrapolation is expected to possibly alter the final PDF results in the endpoint region with small and large x , which is conjugate to the large- λ region [66]. However, this issue is currently not of large concern, since the LaMET expansion breaks down in this region due to large power corrections,

not allowing a reliable prediction anyways.

4.7 Light-cone proton isovector quark transversity distribution

After the renormalized lattice matrix elements are supplemented with extrapolated results for large distances λ , the quasi-LF correlations can be Fourier transformed to momentum space, yielding quasi-distributions in x -space. The light-cone transversity PDF $\delta q(x, P_z, a, m_\pi)$ for different gauge ensembles and proton momenta is then obtained by perturbative matching with the one-loop matching kernel in the hybrid scheme given in eq. (3.21).

4.7.1 Dependence on proton momentum, pion mass and lattice spacing

To picture the dependence of $\delta q(x, P_z, a, m_\pi)$ on the proton momentum P_z , fig. 4.12 shows the light-cone isovector transversity PDF of the proton for the gauge ensembles X650, H102, N203 and N302 with various values of P_z . The ensembles selected for display have almost equal pion mass. As can be seen from the figure, the results exhibit a good convergence with increasing momentum.

The pion mass dependence of the light-cone transversity PDF is investigated by comparing $\delta q(x, P_z, a, m_\pi)$ for the ensembles H102, H105 and C101 with a lattice spacing of $a = 0.085$ fm and $P_z = 1.82$ GeV in fig. 4.13a. The dependence on the pion mass is found to be very mild, as the chosen data sets are almost compatible within errors.

The lattice spacing dependence of $\delta q(x, P_z, a, m_\pi)$ is explored in fig. 4.13b by showing the light-cone transversity PDF for the ensembles X650, H102, N203 and N302 with almost equal pion mass. As it is not possible to entirely disentangle the a -dependence and P_z -dependence, the largest momentum P_z which yields reasonably small errors is chosen for each ensemble. The ensemble X650 (purple curve) with the coarsest lattice spacing does not show good agreement with the other distributions, indicating the presence of discretization effects. With decreasing lattice spacing, the results converge, and the transversity PDF for N203 (blue curve) and N302 (green curve) agrees within error bars.

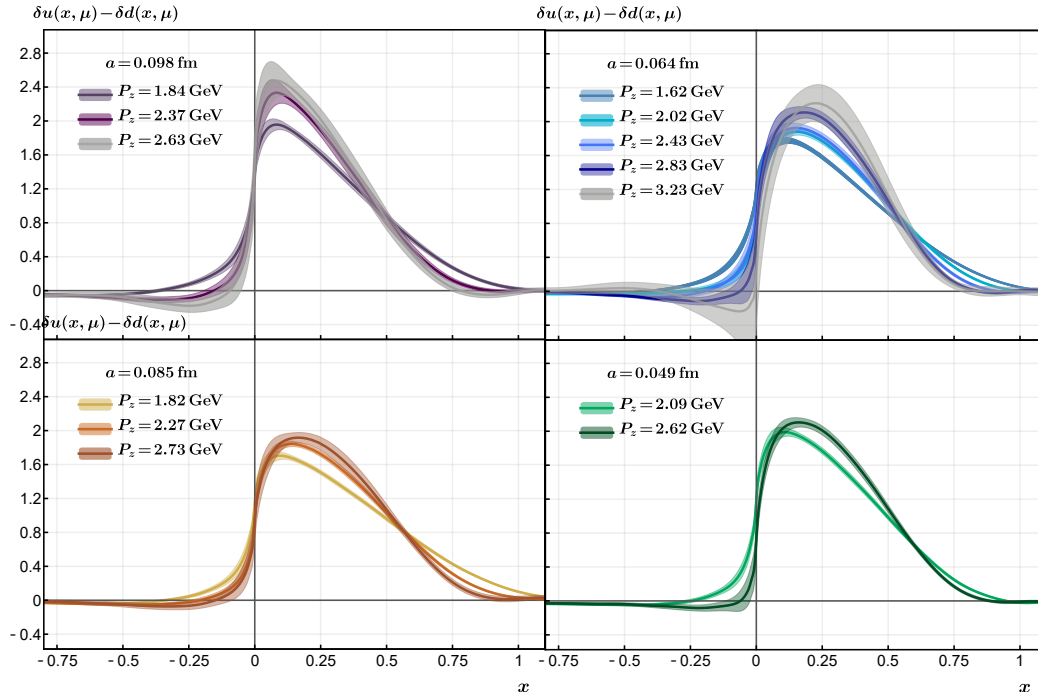
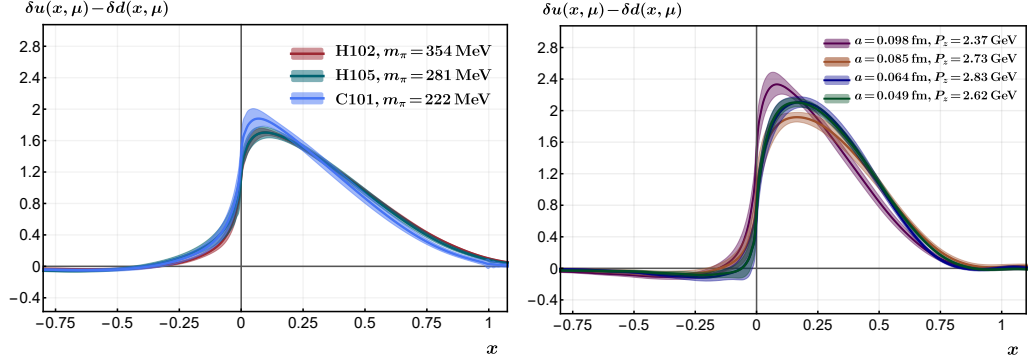


Figure 4.12: Momentum dependence of the isovector quark transversity PDF of the proton at renormalization scale $\mu = 2$ GeV. Shown are the ensembles X650 (upper left), H102 (lower left), N203 (upper right) and N302 (lower right). Data which is excluded from further analysis due to large uncertainties is indicated by grey bands [42].



(a) Pion mass dependence [42].

(b) Lattice spacing dependence [42].

Figure 4.13: Pion mass (4.13a) and lattice spacing (4.13b) dependence of the isovector quark transversity PDF of the proton at renormalization scale $\mu = 2 \text{ GeV}$. The proton momentum chosen for investigation of the pion mass dependence is $P_z = 1.82 \text{ GeV}$. For exploring the a -dependence, the ensembles X650 (purple), H102 (orange), N203 (blue) and N302 (green) with almost equal pion mass are chosen [42].

4.7.2 Combined infinite momentum, physical pion mass and continuum extrapolation

Having extracted the light-cone isovector transversity PDF of the proton for multiple different finite proton momenta, an extrapolation to infinite momentum is performed to ensure the validity of the LaMET factorization formula given in eq. (3.8). Since the calculation is not performed at the physical point, the results are extrapolated to the physical pion mass $m_{\pi, \text{phys}}$. A continuum extrapolation is carried out to remove lattice artifacts. Since for our setup it is not possible to use the same proton momenta for gauge ensembles with different lattice spacings, the P_z -dependence and a -dependence cannot straightforwardly be disentangled. To resolve this issue, the transversity PDF in the infinite momentum, physical pion mass and continuum limit is extracted by a combined extrapolation with the following form

$$\delta q(x, P_z, a, m_\pi) = \frac{1 - g' m_\pi^2 \ln(m_\pi^2 / \mu_0^2) + m_\pi^2 k(x)}{1 - g' m_\pi^2 \ln(m_\pi^2 / \mu_0^2)} \times \left[\delta q_0(x) + a^2 f(x) + a^2 P_z^2 h(x) + \frac{g(x, a)}{P_z^2} \right], \quad (4.27)$$

with $\delta q(x, P_z, a, m_\pi)$ on the l.h.s. denoting the light-cone transversity PDF for ensembles with different lattice spacings and pion masses, as well

as different proton momenta. The form of eq. (4.27) is guided by the study in [154] and includes the chiral logarithm $g'm_\pi^2 \ln(m_\pi^2/\mu_0^2)$ with $\mu_0 = 1$ GeV and $g' = -(4g_A^2 + 1) / [2(4\pi f_\pi)^2]$ in the pion mass extrapolation, with $f_\pi \approx 93$ MeV, and $g_A \approx 1$ being the axial charge of the nucleon. Because CLS ensembles are used in this work, the term $m_\pi^2 k(x)$ is included [155]. The denominator in eq. (4.27) is chosen since the results for the transversity PDF are normalized to the nucleon isovector tensor charge g_T [154]. The terms $a^2 f(x)$ and $a^2 P_z^2 h(x)$ account for discretization effects, while $g(x, a)/P_z^2$ specifies the dependence of the power correction on P_z .

When performing the combined extrapolation, the term $a^2 P_z^2 h(x)$ is zero within errors. The term $a^2 f(x)$, which already has been accounted for in the self renormalization, see eq. (3.17), is also close to zero. The dominant uncertainty from the extrapolation stems from $g(x, a)/P_z^2$.

The final extrapolated result for the transversity PDF is given by

$$\delta q(x) = \frac{1 - g'm_\pi^2 \ln(m_{\pi,\text{phys}}^2/\mu_0^2) + m_{\pi,\text{phys}}^2 k(x)}{1 - g'm_{\pi,\text{phys}}^2 \ln(m_{\pi,\text{phys}}^2/\mu_0^2)} \delta q_0(x). \quad (4.28)$$

4.7.3 Final result and comparison with JAM

The final result for the isovector quark transversity PDF $\delta u(x) - \delta d(x)$ of the proton obtained at $\mu = 2$ GeV, $z_s = 0.3$ fm and $\lambda_L = 7$, normalized by the nucleon isovector tensor charge g_T , is shown in fig. 4.14 as blue curve. The error band includes both statistical and systematic uncertainties, which will be discussed at a later point in this section.

Comparison of final result with global analyses The result of this work is compared to global analyses of the JAM collaboration, namely JAM20 [81] and JAM22 [70], in fig. 4.14. The JAM22 analysis gives an update to JAM20, as it includes new data sets and also constraints from lattice QCD tensor charge calculations and the Soffer bound. Due to those global QCD analysis results being especially sensitive to the chosen data sets and constraints, the difference between JAM22 and JAM20 is seen as a systematic uncertainty from the global fits. The result of this work lies between the two global analyses, showing $\sim 2\sigma$ agreement with both curves, and is consistent with zero in the negative- x region. The shaded bands for $x \in [-0.1, 0.1]$ and $x \in [0.9, 1]$ in fig. 4.14 indicate the region where the LaMET expansion breaks down and predictions are not reliable, considering the largest momentum of $P_z = 2.83$ GeV in this analysis (see section 3.3.1).

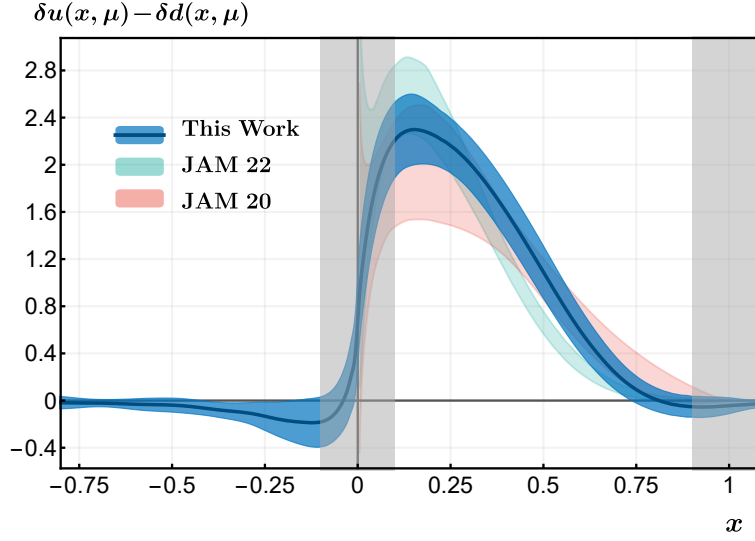


Figure 4.14: Isovector quark transversity PDF of the proton at renormalization scale $\mu = 2 \text{ GeV}$ after extrapolation to the continuum, physical pion mass and infinite momentum limit with eq. (4.27). The result of this work, normalized to the nucleon isovector tensor charge g_T , is shown in blue and compared to the JAM20 [81] and JAM22 [70] global fits [42].

Discussion of uncertainties The final result for the isovector quark transversity PDF of the proton in this work contains statistical as well as different systematic uncertainties, which are added in quadrature to give the full uncertainty. Fig. 4.15 shows the size of the errors from different sources as non-overlapping bands. The statistical uncertainty is estimated using bootstrap resampling with 4000 samples, as well as error propagation for the combined extrapolation. Four different sources of systematic uncertainties are considered, the first of which is from the combined continuum, physical mass and infinite momentum extrapolation. The difference between the extrapolated PDF result and the PDF for N302 and $P_z = 2.62 \text{ GeV}$ is used to approximate this error. Secondly, renormalization scale dependence is considered by varying μ from 2 GeV to 3 GeV and using the difference in the PDF result as systematic uncertainty. The third source of systematic errors is the choice of z_s in the hybrid renormalization scheme. To estimate the corresponding uncertainty, z_s is varied from 0.3 fm to 0.18 fm . Lastly, the value of λ_L in the extrapolation of the renormalized matrix elements to large distances λ is chosen as $\lambda_L = 4$ instead of $\lambda_L = 7$ to use the difference of the results as an error estimate.

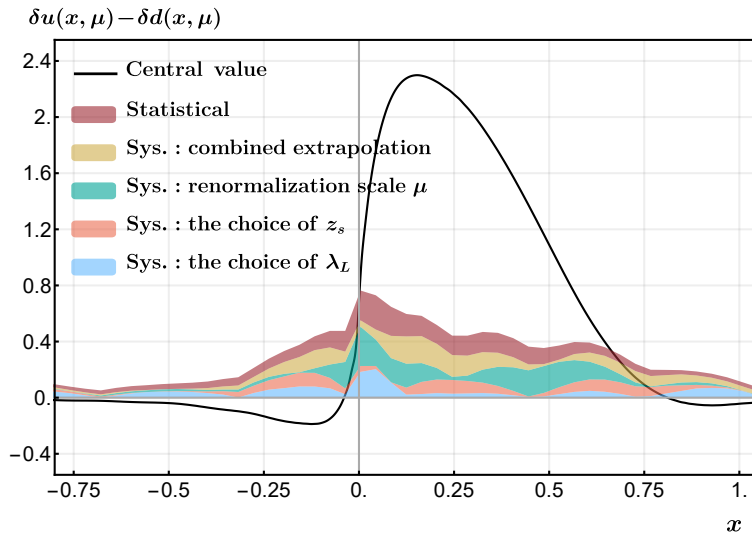


Figure 4.15: Different sources of uncertainties for the isovector quark transversity PDF of the proton with their estimated size depicted as non-overlapping bands. The central value is obtained with $\mu = 2 \text{ GeV}$, $z_s = 0.3 \text{ fm}$ and $\lambda_L = 7$ [42].

Chapter 5

LaMET calculations for the isovector quark Boer-Mulders function of the pion

After having extracted the isovector quark transversity PDF of the proton with LaMET in chapter 4, this chapter will focus on the LaMET calculation of the quark Boer-Mulders function $h_1^\perp(x, b_\perp, \mu, \zeta)$ of the pion. Since TMDPDF calculations on the lattice are just starting, in this work we investigate the pion, for which the signal-to-noise ratio is expected to be better than for other hadrons. The nucleon case is phenomenologically more relevant but is not part of this thesis. As mentioned in section 3.4, TMDPDF calculations are more involved than PDF calculations since TMDPDFs depend in addition on the transverse separation of the quark fields. The Boer-Mulders function in particular is not well constrained from experiments and the theoretical predictions are very limited, see section 3.4.4. Due to those circumstances, the calculation performed in this chapter is not only very tedious and resource consuming, but also highly exploratory.

5.1 Gauge ensembles and setup

For this project, the CLS gauge ensembles X650, H102 and N203, which have been introduced in section 2.4 and whose parameters can be found in tab. 2.1, are used to calculate the quark Boer-Mulders function in the pion. Due to the exploratory nature of this calculation, and also taking into account the mild pion mass dependence of the transversity PDF found in section 4.7.1, ensembles with almost equal pion masses $m_\pi \approx \{338-354\}$ MeV are selected. Lattice spacings of $a = \{0.098, 0.085, 0.064\}$ fm allow for a

Ensemble	$P_z[\text{GeV}]$	$N_{\text{conf.}}$	$N_{\text{meas.}}/N_{\text{conf.}}$
X650	{0, 0.53, 0.79, 1.05, 1.32, 1.58, 1.84}	1892	4
H102	{0, 0.91, 1.37, 1.82}	1008	8
N203	{0, 0.81,	500	8
	1.21, 1.61}	1543	8

Table 5.1: Pion momenta P_z , number of gauge configurations and number of individual measurements per configuration for the ensembles used in the calculation of the quark Boer-Mulders function in the pion.

controlled continuum extrapolation, see section 5.7.7, while more computing resources are needed to also extrapolate to the physical pion mass in the future. Pion momenta up to $P_z = 1.84 \text{ GeV}$ are employed in the analysis, as higher momentum data suffers from significant noise and would require additional computing resources to achieve larger statistics.

For better signal, one step of HYP smearing is applied to the gauge fields, and momentum smearing is used for the quark fields (see section 2.3.2). Eight sources are placed on the lattice, while, in addition, the source positions are modified to perform multiple measurements with a single gauge configuration. The pion momenta, number of configurations and number of individual measurements per configuration used for each CLS ensemble are given in tab. 5.1. For N203, a smaller number of gauge configurations is used in the calculations for the lowest momentum and zero-momentum case, since a sufficient signal can already be seen with that smaller subset of configurations.

5.2 Correlation functions

As for the calculation of the transversity PDF in chapter 4, the calculation of correlation functions on the lattice is necessary to extract the matrix elements needed for the quasi-Boer-Mulders function introduced in 3.5.1. Since in this project the Boer-Mulders function is calculated for a pion, the pion interpolators are used to form the correlators. The pion isotriplet contains two charged pions π^+ and π^- with annihilation operators [47]

$$\begin{aligned}
\mathcal{N}_{\pi^+}(x) &= \bar{d}_c^\alpha(x)(\gamma_5)^{\alpha\beta}u_c^\beta(x) \\
\mathcal{N}_{\pi^-}(x) &= \bar{u}_c^\alpha(x)(\gamma_5)^{\alpha\beta}d_c^\beta(x),
\end{aligned}
\tag{5.1}$$

with space-time coordinate $x = (\vec{x}, t)$, and a neutral pion with annihilation operator [47]

$$\mathcal{N}_{\pi^0}(x) = \frac{1}{\sqrt{2}}(\bar{u}(x)\gamma_5 u(x) - \bar{d}(x)\gamma_5 d(x)). \quad (5.2)$$

Dirac and color indices are omitted in eq. (5.2) and in the following equations. The operators in eq. (5.1) and eq. (5.2) have negative parity and represent color singlets. Besides the annihilation operators which annihilate all states with the same quantum numbers as the respective pion state, creation operators are necessary to form correlation functions. Focusing on the charged pion π^- , the creation operator is found by calculating the conjugation $\mathcal{N}_{\pi^-}^\dagger(x)$ of the interpolator, leading to

$$\bar{\mathcal{N}}_{\pi^-}(x) = \bar{d}(x)\gamma_5 u(x) = \mathcal{N}_{\pi^+}(x), \quad (5.3)$$

which is equal to the annihilation operator for π^+ .

5.2.1 Two-point correlation function

Following the same procedure as for the proton two-point correlation function defined in eq. (4.2), the two-point function for the pion is constructed from the corresponding interpolators by creating a pion at the source $x_{\text{src}} = (\vec{x}_{\text{src}}, t_{\text{src}})$ and annihilating it at the sink $x_{\text{snk}} = (\vec{x}_{\text{snk}}, t_{\text{snk}})$. Not specifying a particular pion interpolator, but using $\mathcal{N}_\pi = \{\mathcal{N}_{\pi^+}, \mathcal{N}_{\pi^-}, \mathcal{N}_{\pi^0}\}$, the two-point correlator is written as

$$C_{2\text{pt}}^\pi(P_z, t_{\text{sep}}) = a^3 \sum_{\vec{x}_{\text{snk}}} e^{-i\vec{p}\cdot(\vec{x}_{\text{snk}} - \vec{x}_{\text{src}})} \langle \mathcal{N}_\pi(x_{\text{snk}}) \bar{\mathcal{N}}_\pi(x_{\text{src}}) \rangle, \quad (5.4)$$

with the spatial momentum $\vec{p} = (0, 0, P_z)$ being non-zero only in z -direction. As in eq. (4.2), the temporal source position t_{src} is set to zero. Since all pion interpolators have definite (negative) parity, no parity projection is needed in the definition of the correlation functions.

A schematic illustration of the lattice setup for calculating the pion two-point function on the lattice is shown in fig. 5.1a, where quark flavors are not specified. The pion source and sink carry momentum P_z in z -direction. One of the quark propagators runs in opposed direction to the other one. This is made plausible by applying Wick's theorem to identify the contractions which are needed to calculate $C_{2\text{pt}}^\pi(P_z, t_{\text{sep}})$ for the pion on the lattice.

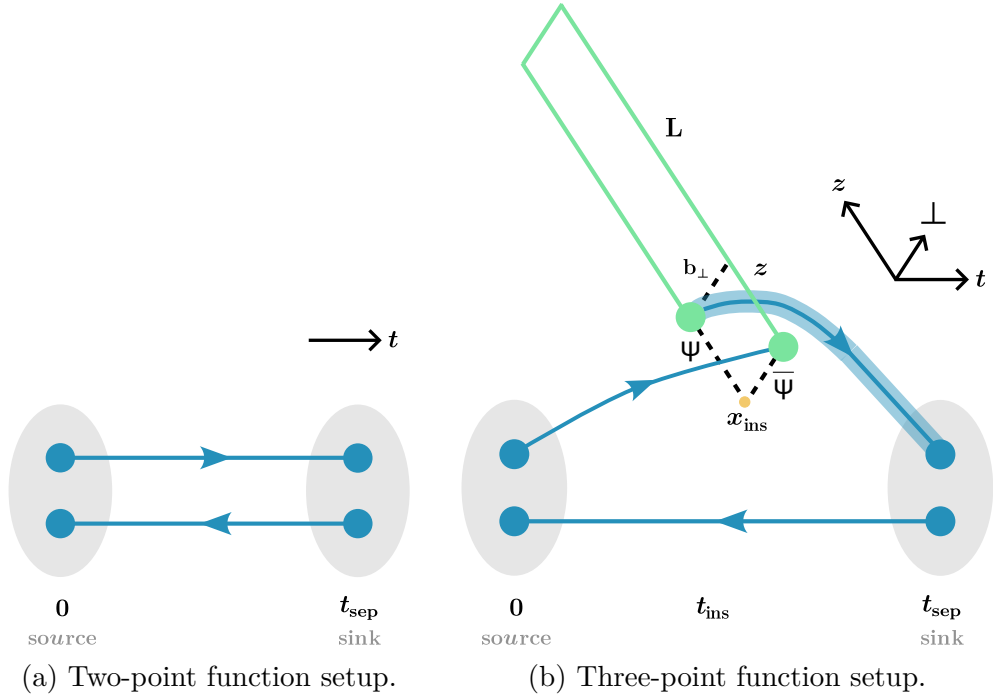


Figure 5.1: Schematic illustration of the lattice calculation of the two-point function $C_{2\text{pt}}^\pi(P_z, t_{\text{sep}})$ (5.1a) and the three-point function $C_{3\text{pt}}^\pi(P_z, t_{\text{ins}}, t_{\text{sep}}, z, b_\perp, L)$ (5.1b) needed for extracting the pion Boer-Mulders function. The pion source and sink have momentum P_z in z -direction. Quark propagators are shown as blue lines, not explicitly stating the quark flavors. For the pion case, the correlators contain one propagator in the opposite direction. Fig. 5.1b: The sequential method [59] is applied to calculate the shaded quark propagator. The inserted quark and antiquark fields that are separated by z in longitudinal and by b_\perp in transverse direction, as well as the staple-shaped Wilson link connecting them, are shown in green. The quark and antiquark fields are both inserted at t_{ins} , an offset in t -direction is used in the figure for better visibility. The point x_{ins} where $z = b_\perp = 0$ is marked in orange.

Wick contractions With the interpolator for the charged pion π^- , using Wick's theorem, the two-point correlation function can be written in terms of quark propagators as

$$C_{2\text{pt}}^{\pi^+}(P_z, t_{\text{sep}}) = -a^3 \sum_{\vec{x}_{\text{snk}}} e^{-i\vec{p}\cdot(\vec{x}_{\text{snk}}-\vec{x}_{\text{src}})} \text{tr} [\gamma_5 U(x_{\text{src}}, x_{\text{snk}}) \gamma_5 D(x_{\text{snk}}, x_{\text{src}})]. \quad (5.5)$$

For exact isospin symmetry, the propagators $U = D$ are equal, leading to the same two-point functions for both charged pions. When performing the Wick contractions for the neutral pion π^0 , disconnected pieces occur. Those contributions cancel each other when isospin symmetry is assumed, leading to the same two-point correlation function as for the charged pions. According to these considerations, when $m_u = m_d$,

$$C_{2\text{pt}}^{\pi}(P_z, t_{\text{sep}}) = C_{2\text{pt}}^{\pi^+}(P_z, t_{\text{sep}}) = C_{2\text{pt}}^{\pi^-}(P_z, t_{\text{sep}}) = C_{2\text{pt}}^{\pi^0}(P_z, t_{\text{sep}}), \quad (5.6)$$

leading to a mass-degenerate pion triplet.

The CLS gauge configurations and pion momenta P_z used to calculate the correlation functions are shown in tab. 5.1. As for the calculation of the nucleon isovector transversity PDF described in chapter 4, the Chroma software suite [153] combined with a multigrid solver [57, 58] is used to perform the lattice calculations for the pion Boer-Mulders function. The additional code, to calculate for example the TMDPDF matrix element or rectangular Euclidean Wilson loop, was developed by Qi-An Zhang within LPC. The lattice calculations for this project were performed at the University of Regensburg using the high-performance computer Athene and at the Leibniz Supercomputing Center with SuperMUC-NG.

For obtaining an estimate of the statistical errors of the correlation functions in this project, binning with a bin size of 5 combined with bootstrap resampling using 800 samples is applied. The bootstrap samples are kept during the entire analysis.

Spectral decomposition As described in section 4.2.1 for the proton two-point function, performing a spectral decomposition for the pion two-point function $C_{2\text{pt}}^{\pi}(P_z, t_{\text{sep}})$ in eq. (5.4) yields

$$C_{2\text{pt}}^{\pi}(P_z, t_{\text{sep}}) \propto e^{-E_0 t_{\text{sep}}} \left(1 + \mathcal{O} \left(e^{-\Delta E t_{\text{sep}}} \right) \right), \quad (5.7)$$

with the energy E_0 of the pion ground state and $\Delta E = E_1 - E_0$ being the energy difference between the pion ground and first excited state.

Ensemble	P_z [GeV]	$t_{\text{sep}}^{\text{min}}/a$	$t_{\text{sep}}^{\text{max}}/a$
X650	0	3	10
	0.53	6	15
	0.79	5	15
	1.05	5	15
	1.32	3	11
	1.58	3	10
	1.84	2	10
H102	0	6	12
	0.91	7	13
	1.37	7	13
	1.82	7	13
N203	0	11	19
	0.81	13	19
	1.21	11	17
	1.61	11	17

Table 5.2: Fit ranges used in the two-state fit with eq. (4.6) of the pion two-point function for each ensemble and P_z , given by the minimum and maximum source-sink separation $t_{\text{sep}}^{\text{min}}/a$ and $t_{\text{sep}}^{\text{max}}/a$.

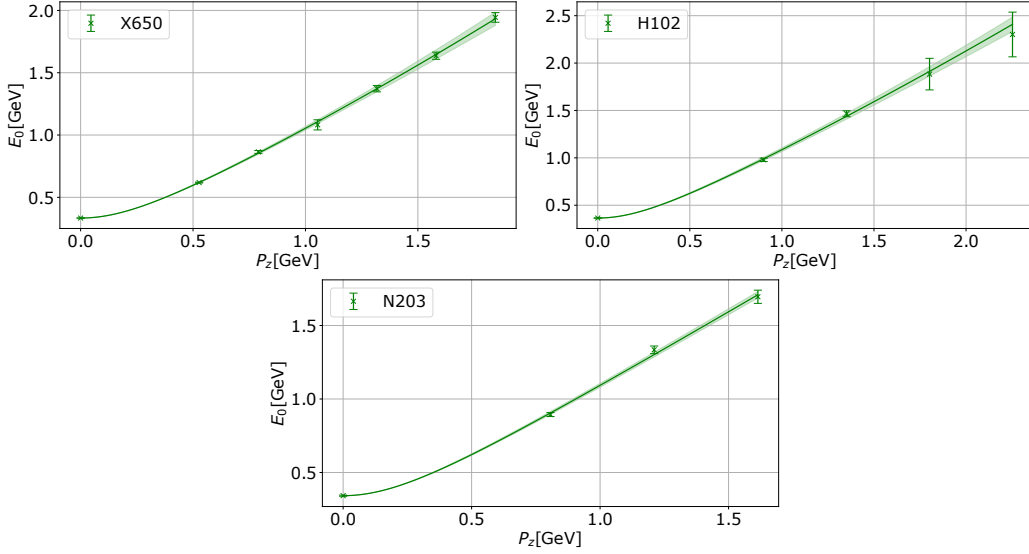


Figure 5.2: Dispersion relation on ensembles X650, H102 and N203. The ground state energies E_0 that are extracted from fitting the pion two-point function with eq. (4.6) are shown together with the results from fitting the dispersion relation with eq. (5.8).

Dispersion relation To extract the pion ground state energy from the two-point correlation function for each momentum P_z , the data is fitted with the same two-state fit form which was introduced in eq. (4.6) for the nucleon, resulting in $E_0(P_z)$. The minimum and maximum values of t_{sep} that are used in the fit of $C_{2\text{pt}}^\pi(P_z, t_{\text{sep}})$ for each ensemble and momentum are given in tab. 5.2. Again, the validity of the continuum dispersion relation is tested with a fit of the extracted energies E_0 with

$$E_0(P_z) = \sqrt{m_\pi^2 + c_1 P_z^2 + c_2 a^2 P_z^4}, \quad (5.8)$$

as already introduced in eq. (4.8) for the nucleon. The pion mass $m_\pi = E(P_z = 0)$ is obtained from the fit of the pion two-point function at zero momentum. The dispersion relation for X650, H102 and N203 is depicted in fig. 5.2, where E_0 extracted from fitting the two-point function with eq. (4.6) is shown together with the result from fitting the dispersion relation with eq. (5.8). The pion masses from fitting $C_{2\text{pt}}^\pi(P_z = 0, t_{\text{sep}})$ using the two-state fit and parameters c_1 , c_2 from fitting the dispersion relation are given in tab. 5.3.

Ensemble	m_π [GeV]	c_1	c_2
X650	0.334(1)	0.972(18)	0.111(50)
H102	0.364(1)	1.028(36)	0.093(38)
N203	0.342(4)	1.079(29)	-0.0093(30)

Table 5.3: Pion mass from two-state fit of $C_{2\text{pt}}^\pi(P_z = 0, t_{\text{sep}})$ with eq. (4.6) and parameters c_1, c_2 from fitting the dispersion relation with eq. (5.8).

5.2.2 Three-point correlation function

To obtain the subtracted quasi-Boer-Mulders function $\tilde{h}_1^\perp(z, b_\perp, P_z, a)$ defined in eq. (3.34), the bare matrix element

$$\tilde{h}_1^{\perp,0}(z, b_\perp, P_z, a, L) \equiv \langle P | \bar{\psi}(b_\perp \hat{n}_\perp) \Gamma \mathcal{W}_z(b_\perp \hat{n}_\perp, z \hat{n}_z) \psi(z \hat{n}_z) | P \rangle, \quad (5.9)$$

which was introduced in the numerator of eq. (3.34), has to be extracted from lattice calculations. For that reason, a three-point correlation function is calculated, where a pion is created at x_{src} , a non-local current

$$\mathcal{O}_\Gamma(x, z, b_\perp, L) = \bar{\psi}(x + b_\perp \hat{n}_\perp) \Gamma \mathcal{W}_z(x + b_\perp \hat{n}_\perp, x + z \hat{n}_z) \psi(x + z \hat{n}_z) \quad (5.10)$$

is inserted at $x_{\text{ins}} = (\vec{x}_{\text{ins}}, t_{\text{ins}})$, and the pion is destroyed at x_{snk} . The quark and antiquark fields in the non-local current are separated by z in longitudinal, i.e. z -direction, and by b_\perp in transverse direction. The transverse direction is chosen as $\perp = x$, and for the gamma structure, $\Gamma = \gamma_1 \gamma_3$ is used. This choice is made by considering the composition of the TMD correlator in b_\perp -space, see eq. (3.33), and setting $+ = 0$, $i = 2$ and $j = 1$. The fields $\bar{\psi}, \psi$ are connected with a staple-shaped gauge link \mathcal{W}_z with extent L along z -direction, which was introduced in eq. (3.35).

With the general pion interpolator \mathcal{N}_π , the three-point correlation function is defined as

$$C_{3\text{pt}}^\pi(P_z, t_{\text{ins}}, t_{\text{sep}}, z, b_\perp, L) = a^6 \sum_{\vec{x}_{\text{snk}}, \vec{x}_{\text{ins}}} e^{-i\vec{p} \cdot (\vec{x}_{\text{snk}} - \vec{x}_{\text{src}})} \times \langle \mathcal{N}_\pi(x_{\text{snk}}) \mathcal{O}_\Gamma(x_{\text{ins}}, z, b_\perp, L) \bar{\mathcal{N}}_\pi(x_{\text{src}}) \rangle. \quad (5.11)$$

Fig. 5.1b shows a simplified illustration of the lattice setup for calculating the three-point function $C_{3\text{pt}}^\pi(P_z, t_{\text{ins}}, t_{\text{sep}}, z, b_\perp, L)$ for the pion. Source and

sink carry momentum P_z in z -direction. Quark flavors are not made explicit. The lower blue line depicts a quark propagator in opposite direction to the other propagators, which follows from the Wick contractions. The sequential method [59], see section 2.3.1, is applied to calculate the shaded quark propagator. Quark and antiquark fields are depicted in green and are both inserted at t_{ins} , where an offset in t -direction is used for better visibility in the figure. ψ and $\bar{\psi}$ are separated by z in longitudinal and by b_\perp in transverse direction, connected by a staple-shaped link with extent L , which is also drawn in green.

Wick contractions As for the two-point function, Wick's theorem is used to express $C_{3\text{pt}}(P_z, t_{\text{ins}}, t_{\text{sep}}, z, b_\perp, L)$ in terms of quark propagators. Using the negatively charged pion π^- with up quark current insertion, i.e. setting $\bar{\psi} = \bar{u}$ and $\psi = u$ in eq. (5.10), gives

$$\begin{aligned}
C_{3\text{pt}}^{\pi^-, u}(P_z, t_{\text{ins}}, t_{\text{sep}}, z, b_\perp, L) &= -a^6 \sum_{\vec{x}_{\text{snk}}, \vec{x}_{\text{ins}}} e^{-i\vec{p}\cdot(\vec{x}_{\text{snk}} - \vec{x}_{\text{src}})} \\
&\times \left\{ \text{tr} \left[\gamma_5 D(x_{\text{snk}}, x_{\text{src}}) \gamma_5 U(x_{\text{src}}, x_{\text{ins}} + b_\perp \hat{n}_\perp) \gamma_1 \gamma_3 \mathcal{W}_z(x_{\text{ins}} + b_\perp \hat{n}_\perp, x_{\text{ins}} + z \hat{n}_z) \right. \right. \\
&\quad \left. \left. U(x_{\text{ins}} + z \hat{n}_z, x_{\text{snk}}) \right] \right. \\
&\quad \left. - \text{tr} \left[\gamma_5 D(x_{\text{snk}}, x_{\text{src}}) \gamma_5 U(x_{\text{src}}, x_{\text{snk}}) \gamma_1 \gamma_3 \mathcal{W}_z(x_{\text{ins}} + b_\perp \hat{n}_\perp, x_{\text{ins}} + z \hat{n}_z) \right. \right. \\
&\quad \left. \left. U(x_{\text{ins}} + z \hat{n}_z, x_{\text{ins}} + b_\perp \hat{n}_\perp) \right] \right\}. \tag{5.12}
\end{aligned}$$

The contractions for π^- with down quark current insertion, i.e. $\bar{\psi} = \bar{d}$ and $\psi = d$ in eq. (5.10), read

$$\begin{aligned}
C_{3\text{pt}}^{\pi^-, d}(P_z, t_{\text{ins}}, t_{\text{sep}}, z, b_\perp, L) &= -a^6 \sum_{\vec{x}_{\text{snk}}, \vec{x}_{\text{ins}}} e^{-i\vec{p}\cdot(\vec{x}_{\text{snk}} - \vec{x}_{\text{src}})} \\
&\times \left\{ \text{tr} \left[\gamma_5 U(x_{\text{src}}, x_{\text{snk}}) \gamma_5 D(x_{\text{snk}}, x_{\text{ins}} + b_\perp \hat{n}_\perp) \gamma_1 \gamma_3 \mathcal{W}_z(x_{\text{ins}} + b_\perp \hat{n}_\perp, x_{\text{ins}} + z \hat{n}_z) \right. \right. \\
&\quad \left. \left. D(x_{\text{ins}} + z \hat{n}_z, x_{\text{src}}) \right] \right. \\
&\quad \left. - \text{tr} \left[\gamma_5 U(x_{\text{src}}, x_{\text{snk}}) \gamma_5 D(x_{\text{snk}}, x_{\text{src}}) \gamma_1 \gamma_3 \mathcal{W}_z(x_{\text{ins}} + b_\perp \hat{n}_\perp, x_{\text{ins}} + z \hat{n}_z) \right. \right. \\
&\quad \left. \left. D(x_{\text{ins}} + z \hat{n}_z, x_{\text{ins}} + b_\perp \hat{n}_\perp) \right] \right\}. \tag{5.13}
\end{aligned}$$

The second contraction in eq. (5.12) as well as in eq. (5.13) contains a propagator which starts and ends at the same time coordinate t_{ins} . This

Ensemble	t_{sep}/a	z_{max}/a	$b_{\perp,\text{max}}/a$	L/a
X650	{6,7,8,9,10}	18	7	{8,10}
H102	{7,8,9,10,11,12}	22	8	{8,10}
N203	{9,11,13,15,17}	28	9	{10,12}

Table 5.4: Source-sink separations t_{sep}/a , maximum longitudinal separation z_{max}/a and transverse separation $b_{\perp,\text{max}}/a$ of the inserted quark fields, and extent L/a of the staple-shaped Wilson link connecting the inserted quark fields in the calculation of the pion Boer-Mulders function.

contribution is equivalent for up and down quark insertion in the case of exact isospin symmetry where $U = D$. Again, as for the contractions of the pion two-point function, the pion contractions in eq. (5.12) and eq. (5.13) each contain one quark propagator pointing in opposite direction compared to the other propagators.

The source-sink separations, maximum longitudinal and transverse separation of the inserted quark fields as well as the extent of the staple-shaped Wilson link connecting the inserted quark fields in the calculation of $C_{3\text{pt}}^\pi(P_z, t_{\text{ins}}, t_{\text{sep}}, z, b_\perp, L)$ are listed in tab. 5.4. The momenta and gauge configurations used in the calculation were already shown in tab. 5.1. A smaller subset of configurations was used to calculate the three-point function for a larger variety of L and examine the L -dependence of the subtracted quasi-Boer-Mulders function, which will be discussed in section 5.4.2.

Spectral decomposition As described for the nucleon transversity PDF in section 4.2.2, a spectral decomposition of the pion three-point correlator $C_{3\text{pt}}^\pi(P_z, t_{\text{ins}}, t_{\text{sep}}, z, b_\perp, L)$ given by eq. (5.11) is performed in order to identify a fit function for extracting the bare matrix element $\tilde{h}_1^{\perp,0}(z, b_\perp, P_z, a, L)$ defined in eq. (5.9). As the decomposition is analogous to the nucleon case, it is not repeated here.

5.3 Extraction of the ground state matrix element

To obtain the pion Boer-Mulders function from the correlators calculated on the lattice, the bare ground state matrix element $\tilde{h}_1^{\perp,0}(z, b_\perp, P_z, a, L)$ defined

in eq. (5.9) is necessary. As was done for the transversity PDF in section 4.3, a ratio of three-point and two-point correlation functions is fitted in combination with the two-point function in order to extract the desired matrix element. Compared to the PDF case, the ratio

$$R_\Gamma(P_z, t_{\text{ins}}, t_{\text{sep}}, z, b_\perp, L) = \frac{C_{3\text{pt}}^\pi(P_z, t_{\text{ins}}, t_{\text{sep}}, z, b_\perp, L)}{C_{2\text{pt}}^\pi(P_z, t_{\text{sep}})} \quad (5.14)$$

for the determination of the pion Boer-Mulders function additionally depends on the transverse separation b_\perp of the inserted quark fields, and on the extent L of the staple-shaped gauge link connecting them. Therefore, a larger number of individual fits has to be performed and the fit parameters show an additional dependence on b_\perp and L . The ratio defined in eq. (5.14) is fitted with

$$R_\Gamma(P_z, t_{\text{ins}}, t_{\text{sep}}, z, b_\perp, L) = \frac{c_0 + c_1 \left[e^{-\Delta E(t_{\text{sep}} - t_{\text{ins}})} + e^{-\Delta E t_{\text{ins}}} \right] + c_3 e^{-\Delta E t_{\text{sep}}}}{1 + c_5 e^{-\Delta E t_{\text{sep}}}}, \quad (5.15)$$

where the dependence of the fit parameters c_0, c_1, c_3, c_5 and ΔE on a, P_z and z is not made explicit. As for the transversity PDF extraction, see section 4.3, c_5 and ΔE are mainly fixed from the two-point function. The parameters c_0, c_1 and c_3 additionally depend on b_\perp and L , with the dependence being omitted in eq. (5.15) for better readability. The fit parameter $c_0(z, b_\perp, P_z, a, L) \equiv \tilde{h}_1^{\perp,0}(z, b_\perp, P_z, a, L)$ is the desired bare ground state matrix element.

The fit ranges of the two-point function in the combined fit are the same as given in tab. 5.2. For all ensembles, the contact points $t_{\text{ins}} = 0$ and $t_{\text{ins}} = t_{\text{sep}}$ of the ratios are excluded from the fit, while for N203 the points $t_{\text{ins}} = 1$ and $t_{\text{ins}} = t_{\text{sep}} - 1$ are also excluded. Correlated fits, which minimize χ^2 as defined in eq. (2.40), are used to extract the bare ground state matrix element $\tilde{h}_1^{\perp,0}(z, b_\perp, P_z, a, L)$, and the correlations are kept during the entire analysis. Examples for fits of the ratio $R_\Gamma(P_z, t_{\text{ins}}, t_{\text{sep}}, z, b_\perp, L)$ are shown in fig. 5.3, fig. 5.4, and fig. 5.5 for X650, H102 and N203, respectively. In order to portray the quality of the data realistically, the largest momentum used in the analysis is shown in addition to a smaller value of P_z for each ensemble. For each largest momentum, not all available source-sink separations are used in the fits. The data points with large t_{sep} have larger uncertainties, and including them in the fits does not significantly alter the results.

For X650, the real parts of the ratio R_Γ for the combinations $(P_z, b_\perp) = (0.79\text{GeV}, 1a)$, $(P_z, b_\perp) = (1.58\text{GeV}, 3a)$ as well as the real and imaginary parts for $(P_z, b_\perp) = (0.79\text{GeV}, 3a)$ are depicted. For all cases, $z = (1, 3, 5)a$

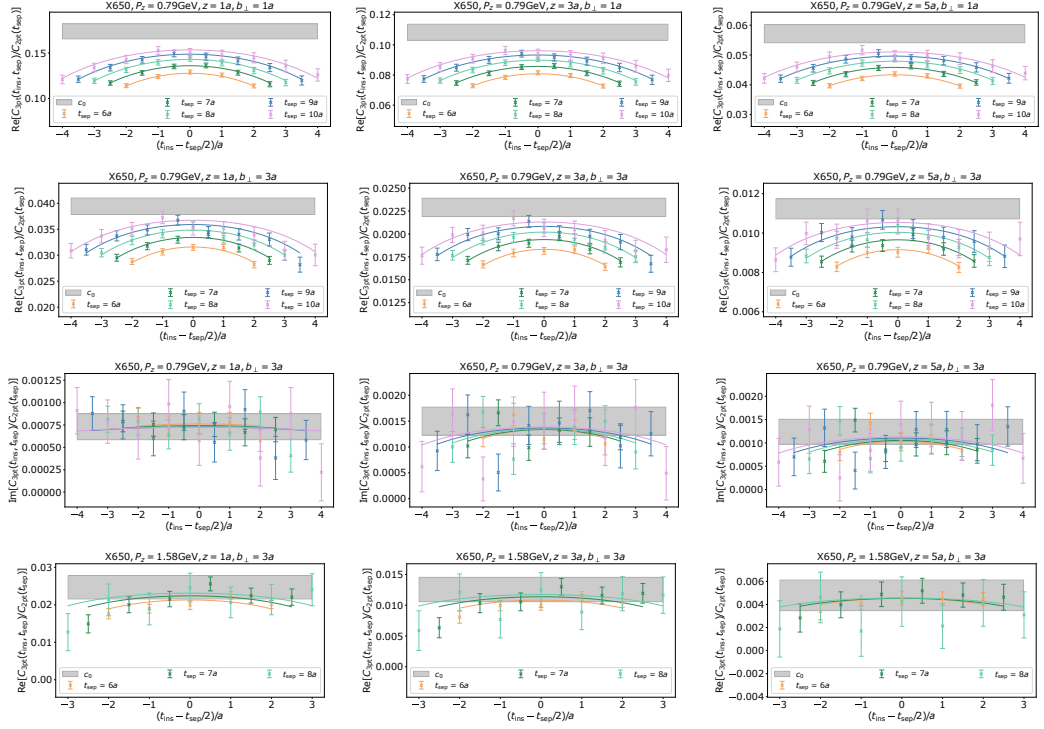


Figure 5.3: Examples for fits of the ratio $R_\Gamma(P_z, t_{\text{ins}}, t_{\text{sep}}, z, b_\perp, L)$ with eq. (5.15) to extract the bare ground state matrix element $\tilde{h}_1^{\perp,0}(z, b_\perp, P_z, a, L)$ for X650. The real parts of $(P_z, b_\perp) = (0.79\text{GeV}, 1a)$ (first row), $(P_z, b_\perp) = (1.58\text{GeV}, 3a)$ (fourth row), as well as the real (second row) and imaginary (third row) parts of $(P_z, b_\perp) = (0.79\text{GeV}, 3a)$ are depicted. For all cases, $z = (1, 3, 5)a$ and $L = 8a$ are shown.

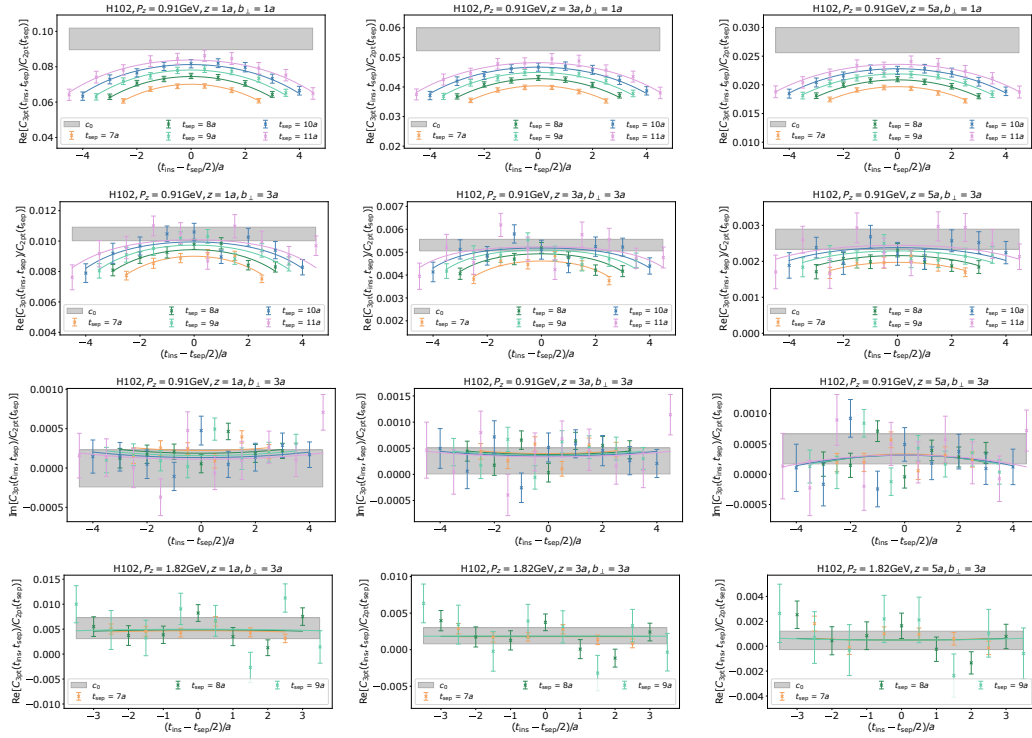


Figure 5.4: Examples for fits of the ratio $R_\Gamma(P_z, t_{\text{ins}}, t_{\text{sep}}, z, b_\perp, L)$ with eq. (5.15) to extract the bare ground state matrix element $\tilde{h}_1^{\perp,0}(z, b_\perp, P_z, a, L)$ for H102. The real parts of $(P_z, b_\perp) = (0.91\text{GeV}, 1a)$ (first row), $(P_z, b_\perp) = (1.82\text{GeV}, 3a)$ (fourth row), as well as the real (second row) and imaginary (third row) parts of $(P_z, b_\perp) = (0.91\text{GeV}, 3a)$ are depicted. For all cases, $z = (1, 3, 5)a$ and $L = 8a$ are shown.

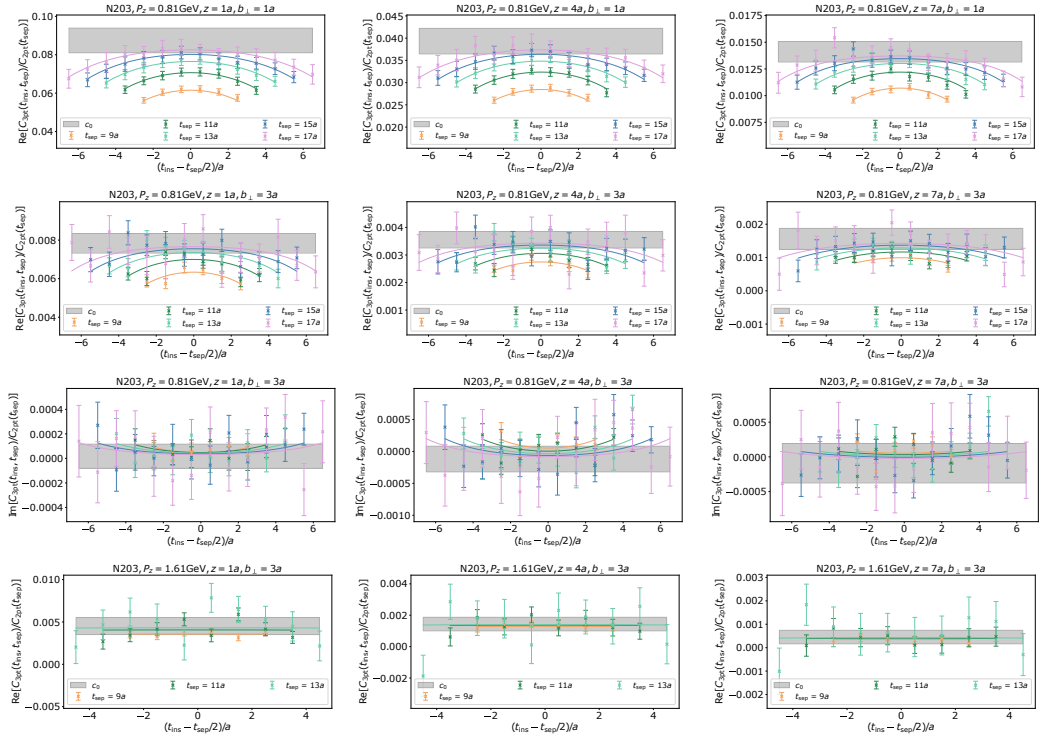


Figure 5.5: Examples for fits of the ratio $R_\Gamma(P_z, t_{\text{ins}}, t_{\text{sep}}, z, b_\perp, L)$ with eq. (5.15) to extract the bare ground state matrix element $\tilde{h}_1^{\perp,0}(z, b_\perp, P_z, a, L)$ for N203. The real parts of $(P_z, b_\perp) = (0.81\text{GeV}, 1a)$ (first row), $(P_z, b_\perp) = (1.61\text{GeV}, 3a)$ (fourth row), as well as the real (second row) and imaginary (third row) parts of $(P_z, b_\perp) = (0.81\text{GeV}, 3a)$ are depicted. For all cases, $z = (1, 4, 7)a$ and $L = 10a$ are shown.

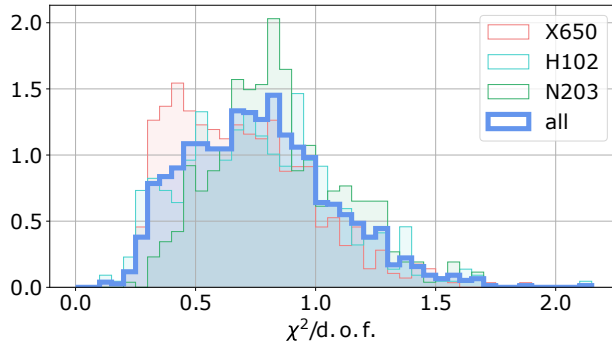


Figure 5.6: Histograms of $\chi^2/\text{d.o.f.}$ of all two-state fits of the ratio combined with the two-point function to extract the bare ground state matrix elements $\tilde{h}_1^{\perp,0}(z, b_\perp, P_z, a, L)$. The distributions are also shown for the ensembles individually and are normalized to 1.

and $L = 8a$ are shown. The depicted imaginary parts are at least an order of magnitude smaller than the real parts.

In the case of H102, the real parts of R_Γ for $(P_z, b_\perp) = (0.91\text{GeV}, 1a)$, $(P_z, b_\perp) = (1.82\text{GeV}, 3a)$, and the real and imaginary parts of $(P_z, b_\perp) = (0.91\text{GeV}, 3a)$ are depicted. For all cases mentioned, $z = (1, 3, 5)a$ and $L = 8a$ are shown. The imaginaries part in fig. 5.4 are consistent with zero in 2σ .

Examples for fits of the ratio for N203 are shown in fig. 5.5. The real parts for $(P_z, b_\perp) = (0.81\text{GeV}, 1a)$, $(P_z, b_\perp) = (1.61\text{GeV}, 3a)$ as well as the real and imaginary parts for $(P_z, b_\perp) = (0.81\text{GeV}, 3a)$ are depicted. For all cases, $z = (1, 4, 7)a$ and $L = 10a$ are shown.

To inspect the fit quality of the combined two-state fits of the ratio $R_\Gamma(P_z, t_{\text{ins}}, t_{\text{sep}}, z, b_\perp, L)$ and two-point function $C_{2\text{pt}}^\pi(P_z, t_{\text{sep}})$, fig. 5.6 shows the histogram of $\chi^2/\text{d.o.f.}$ (normalized to 1) for all ensembles combined, as well as individually. The values of $\chi^2/\text{d.o.f.}$ lie in a reasonable range.

5.4 Renormalization in the short distance ratio scheme

The bare ground state matrix elements $\tilde{h}_1^{\perp,0}(z, b_\perp, P_z, a, L)$ are renormalized in the short distance ratio scheme, as described in section 3.5.2. For obtaining the renormalized matrix elements, it is necessary to construct the subtracted quasi-Boer-Mulders function $\check{h}_1^\perp(z, b_\perp, P_z, a)$, which was defined in eq. (3.34), to eliminate the linear divergence and pinch-pole singularity.

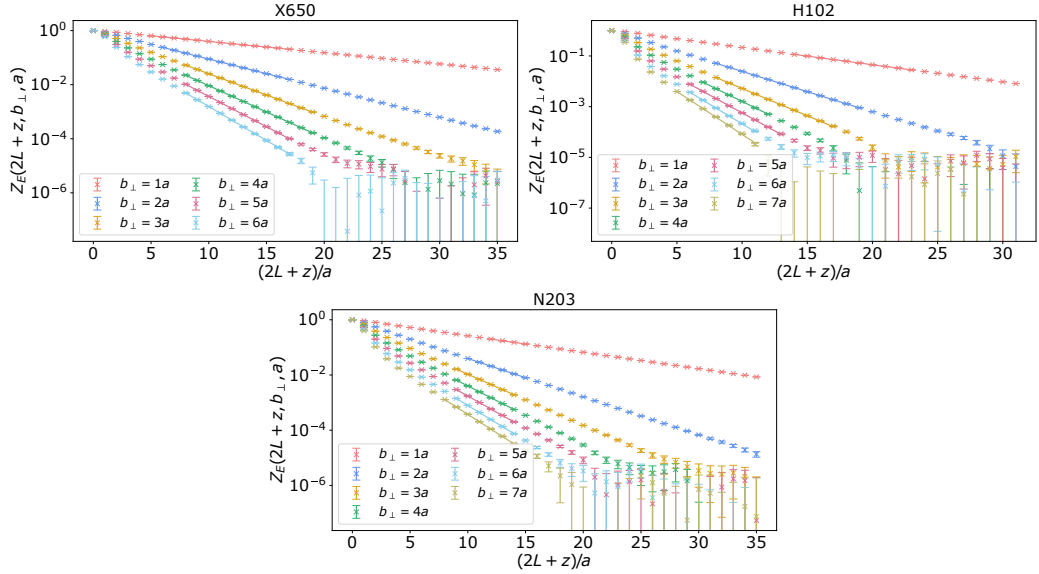


Figure 5.7: Fit of the rectangular Euclidean Wilson loop $Z_E(2L+z, b_\perp, a)$ with eq. (5.16) for X650, H102 and N203, and various values of b_\perp . The fitted results and fit ranges are indicated by solid lines.

5.4.1 Fit of the rectangular Wilson loop

A rectangular Euclidean Wilson loop $Z_E(2L+z, b_\perp, a)$ with length $2L+z$ and width b_\perp is included in the definition of the subtracted quasi-Boer-Mulders function. The loop is calculated on the lattice for all gauge configurations available for X650, H102 and N203, see tab. 5.1. The signal-to-noise ratio of $Z_E(2L+z, b_\perp, a)$ decays rapidly with increasing $2L+z$ and b_\perp , possibly even leading to negative central values, which make the square root in eq. (3.34) ill-defined. To solve this problem, the Wilson loop is fitted with [138]

$$Z_E(2L+z, b_\perp, a) = c(b_\perp, a) e^{-V(b_\perp, a)(2L+z)} \quad (5.16)$$

for various values of b_\perp for each ensemble and extrapolated to large $2L+z$. The fit parameter $V(b_\perp, a)$ in eq. (5.16) is the static QCD potential. Fig. 5.7 illustrates the fit of Z_E for X650, H102 and N203 for different values of b_\perp .

5.4.2 Dependence of the subtracted quasi-TMDPDF on the staple-link length

The subtracted quasi-TMDPDF $\tilde{h}_1^\perp(z, b_\perp, P_z, a)$ defined in eq. (3.34) is determined by dividing the bare matrix elements by the square root of the

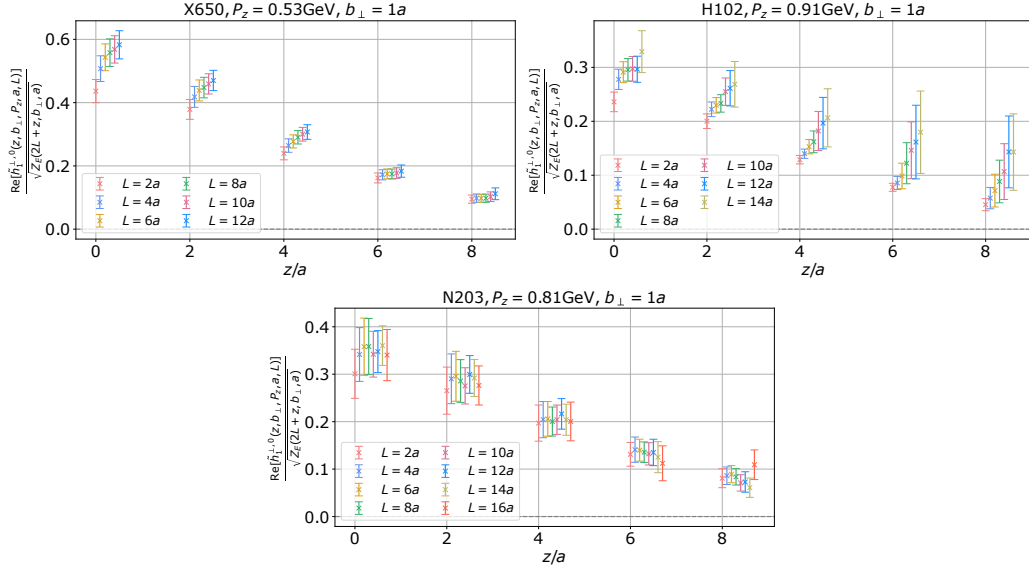


Figure 5.8: Real parts $\text{Re}[\tilde{h}_1^{\perp,0}(z, b_{\perp}, P_z, a, L)]$ of the bare matrix elements divided by the square root of the rectangular Wilson loop for X650, H102 and N203 with limited statistics for various values of L . Momenta of $P_z = 0.53 \text{ GeV}$, $P_z = 0.91 \text{ GeV}$ and $P_z = 0.81 \text{ GeV}$ are chosen for X650, H102 and N203, respectively, while $b_{\perp} = 1a$ and $z = \{0, 2, 4, 6, 8\}a$ are shown for all ensembles. The data points are shifted in horizontal direction for better visibility.

extrapolated rectangular Wilson loop. In order for the subtracted quasi-TMDPDF to be well-defined, it should not depend on the length L of the staple-shaped Wilson link. A plateau of $\tilde{h}_1^{\perp}(z, b_{\perp}, P_z, a)$ is expected for increasing values of L , where it is ensured that the staple link extends outside the hadron.

To investigate the L -dependence of the subtracted quasi-Boer-Mulders function, three-point correlation functions are calculated for various values of L on smaller subsets of configurations for each ensemble. For H102, 100 configurations with eight measurements per configuration were analyzed, while for N203, 25 configurations with eight measurements per configuration were used. All available configurations were used for X650, with one measurement for each configuration. In order to find a signal with limited statistics, small momenta of $P_z = 0.53 \text{ GeV}$, $P_z = 0.91 \text{ GeV}$ and $P_z = 0.81 \text{ GeV}$ were utilized in the calculations for X650, H102 and N203, respectively.

The results for the subtracted matrix elements obtained with limited statistics for different link lengths, $z = \{0, 2, 4, 6, 8\}a$ and $b_{\perp} = 1a$ are shown

in fig. 5.8. Only the real parts are depicted, since the imaginary parts are consistent with zero. The minimum value of $L_{\min} = 2a$ and the step size of $2a$ are the same for each ensemble, while the maximum value of L is chosen as $L_{\max} = 12a$ for X650, $L_{\max} = 14a$ for H102 and $L_{\max} = 16a$ for N203. As is apparent from the figure, the L -dependence of the subtracted matrix elements is weak, a plateau is found for all ensembles and values of z . Since the signal becomes worse with increasing L , values of $L = 8a$ for X650 and H102, as well as $L = 10a$ for N203 are chosen for the calculation with full statistics.

5.4.3 Calculation of renormalization factors

After obtaining the subtracted matrix elements $\tilde{h}_1^\perp(z, b_\perp, P_z, a)$ for all ensembles, and verifying that they are not dependent on L , the matrix elements need to be renormalized to eliminate logarithmic UV divergences. As described in section 3.5.2, the renormalization factors $Z_O(z_0, b_{\perp,0}, a)$ are extracted in the short distance ratio scheme at next-to-leading order using the continuum perturbative zero-momentum matrix element $\tilde{h}_{1,\text{pert.}}^{\perp, \text{MS}}(z_0, b_{\perp,0}, P_z = 0, \mu)$ given in eq. (3.39) at renormalization scale $\mu = 2 \text{ GeV}$.

The NLO renormalization factors for various values of z_0 and $b_{\perp,0}$ for X650, H102 and N203 are shown in the left panel of fig. 5.9. For X650 and H102 there is no window in which $Z_O(z_0, b_{\perp,0}, a, \mu)$ is independent of z_0 and $b_{\perp,0}$. For N203, a window is found for $b_{\perp,0} = \{2, 3\}a$ and $z_0 = \{0, 1\}a$. The renormalization factor for N203 and $b_{\perp,0} = 1a$ does not lie inside this window, indicating the presence of discretization effects.

When applying renormalization group resummation, which was introduced in section 3.5.2, in the determination of the factors $Z_O(z_0, b_{\perp,0}, a, \mu)$, a window in which Z_O is independent of $b_{\perp,0}$ and z_0 can be identified for X650, H102, as well as for N203. The right panel of fig. 5.9 shows the renormalization factors calculated with the zero-momentum perturbative continuum matrix element resummed at NLO according to eq. (3.42) for X650, H102 and N203. The physical scale is chosen as $\mu_0 = r \cdot 2e^{-\gamma_E} / \sqrt{b_{\perp,0}^2 + z_0^2}$ with prefactor $r = 1$. To estimate the uncertainty from RGR, r is varied from 0.8 to 1.2, leading to a systematic uncertainty that is included in the errorbars in the right panel of fig. 5.9, in addition to the statistical uncertainty.

Windows of constant $Z_O(z_0, b_{\perp,0}, a, \mu)$ are found at $b_{\perp,0} = \{2, 3\}a$, $z_0 = \{0, 1, 2\}a$ for X650, at $b_{\perp,0} = \{2, 3\}a$, $z_0 = \{0, 1\}a$ for H102, and at $b_{\perp,0} = \{2, 3\}a$, $z_0 = \{0, 1, 2\}a$ for N203. The renormalization factors for $b_{\perp,0} = 1a$ do not lie in the windows of constant Z_O , again indicating the presence of discretization effects.

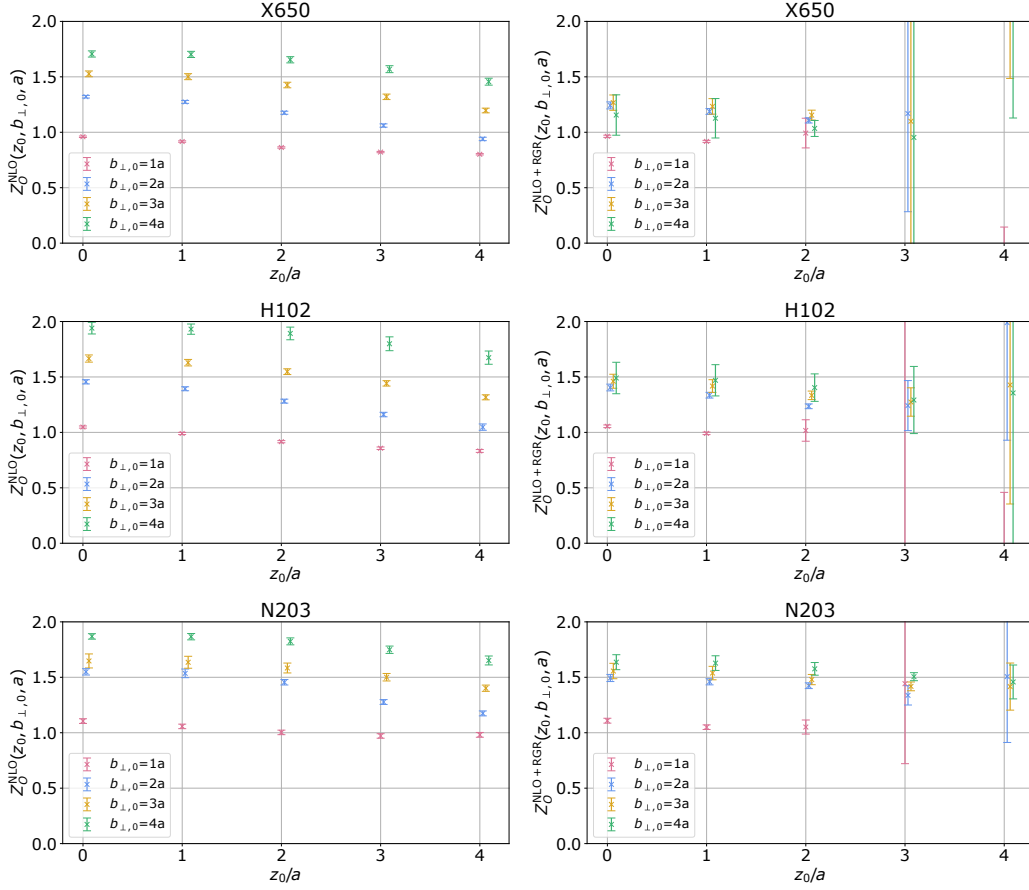


Figure 5.9: NLO renormalization factors $Z_O(z_0, b_{\perp,0}, a, \mu)$ at scale $\mu = 2$ GeV for X650, H102 and N203 with various values of $b_{\perp,0}$ and z_0 . The left panel shows Z_O determined without RGR as in eq. (3.38), while the right panel shows the results for Z_O obtained with RGR according to eq. (3.42), where the error includes the statistical uncertainty as well as the systematic uncertainty from varying the prefactor r of μ_0 in the resummation between 0.8 and 1.2. The data points are shifted in horizontal direction for better visibility.

The final renormalization factors used for the analysis in this thesis are obtained by averaging Z_O over the regions that were just mentioned. The resulting values for each ensemble are

$$\begin{aligned} Z_{O,X650}^{\text{NLO+RGR}} &= 1.199(16)(43), \\ Z_{O,H102}^{\text{NLO+RGR}} &= 1.405(20)(38), \\ Z_{O,N203}^{\text{NLO+RGR}} &= 1.469(32)(17), \end{aligned} \tag{5.17}$$

with the first error being the statistical uncertainty estimated with bootstrap resampling and the second error arising from the scale variation in RGR.

5.5 Extrapolation for large quasi-LF distances

With the renormalization factors calculated in the short distance ratio scheme for each ensemble, the renormalized quasi-TMDPDF $\tilde{h}_1^{\perp,\overline{\text{MS}}}(z, b_\perp, P_z, \mu)$ in coordinate space defined in eq. (3.37) is obtained for various momenta P_z , transverse distances b_\perp and $\lambda = zP_z$. For large values of λ , the renormalized quasi-TMDPDF decays to zero, but uncertainties are substantial, especially for large b_\perp and P_z . Truncating the data in the Fourier transformation would lead to unphysical oscillations of the distributions in momentum space. Thus, as was done for the transversity PDF in section 4.6, an extrapolation is used for large values of λ . The extrapolation form of the quasi-PDF, given in eq. (4.26), is adopted for quasi-TMDPDFs by allowing all parameters to depend on b_\perp . The fits for different P_z and b_\perp are performed individually.

Examples for the extrapolation of the renormalized matrix elements for large λ are given in fig. 5.10. The upper panel shows the real (left) and imaginary (right) parts of $\tilde{h}_1^{\perp,\overline{\text{MS}}}(z, b_\perp, P_z, \mu)$ for N203 with $P_z = 0.81$ GeV and $b_\perp = 2a$ together with the result after extrapolation in green and the fit region shaded in gray. The fit result is shown for all λ where the data is substituted with the extrapolation in the further steps of the analysis. The extrapolation gives a smooth curve with reduced errors for large λ , and it was verified that it reproduces the original data in the region of smaller λ . The lower panel of fig. 5.10 depicts the extrapolation of the real part of the renormalized matrix elements for N203 and $b_\perp = 2a$ for the larger momenta of $P_z = 1.21$ GeV (left) and $P_z = 1.61$ GeV (right). The uncertainties of $\tilde{h}_1^{\perp,\overline{\text{MS}}}(z, b_\perp, P_z, \mu)$ get larger with increasing P_z , making the use of an extrapolation even more crucial.

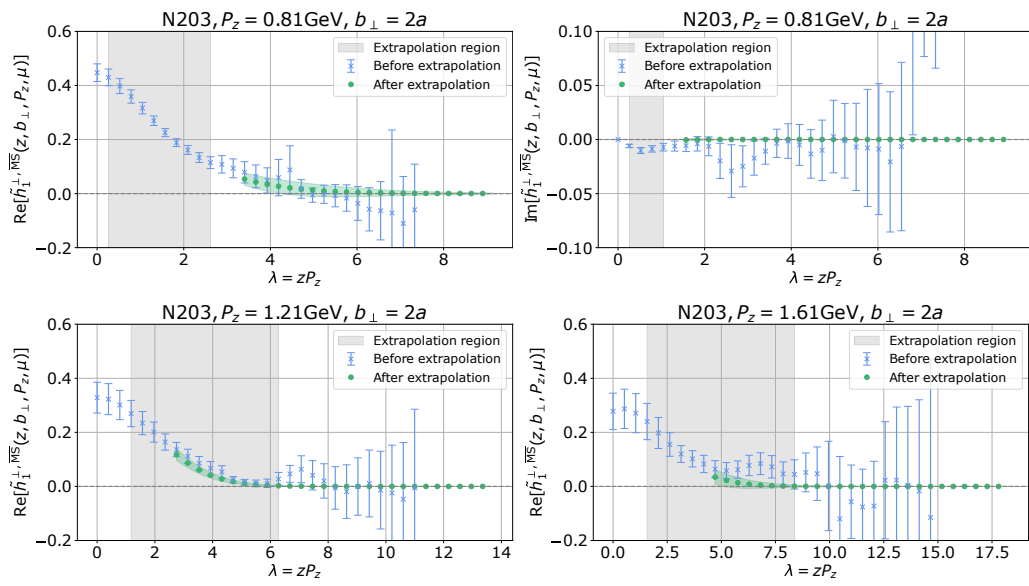


Figure 5.10: Extrapolation of $\tilde{h}_1^{\perp, \overline{\text{MS}}}(z, b_{\perp}, P_z, \mu)$ with eq. (4.26) for large $\lambda = zP_z$. The original data is depicted in blue, the fit regions are shaded in gray, and the results of the extrapolation are shown in green. The extrapolated results are used for the further analysis in the region where they are depicted in the figure. Upper panel: Real (left) and imaginary (right) parts of $\tilde{h}_1^{\perp, \overline{\text{MS}}}$ for N203, $b_{\perp} = 2a$, $P_z = 0.81$ GeV. Lower panel: Real part of $\tilde{h}_1^{\perp, \overline{\text{MS}}}$ for N203, $b_{\perp} = 2a$ with momentum $P_z = 1.21$ GeV (left) and $P_z = 1.61$ GeV (right).

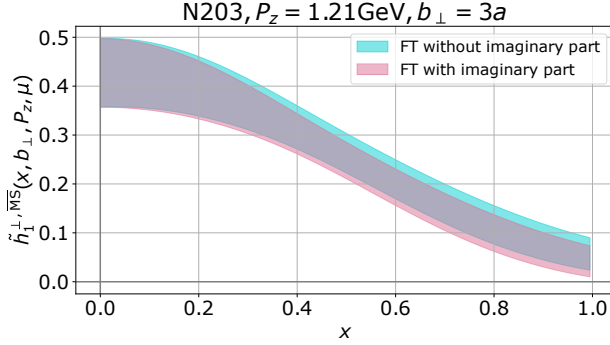


Figure 5.11: Renormalized quasi-TMDPDF $\tilde{h}_1^{\perp, \overline{\text{MS}}}(x, b_{\perp}, P_z, \mu)$ in momentum space for N203, $P_z = 1.21$ GeV and $b_{\perp} = 3a$. The case where only the real part of the coordinate space distribution is used in the Fourier transformation is shown in turquoise, the case including both the real and imaginary part in the Fourier transformation is shown in pink.

5.6 Fourier transformation to x -space

Before matching the renormalized quasi-Boer-Mulders function to the light-cone, the results are Fourier transformed to momentum space, yielding distributions $\tilde{h}_1^{\perp, \overline{\text{MS}}}(x, b_{\perp}, P_z, \mu)$ for various ensembles, P_z and values of b_{\perp} . Since the mean value of the imaginary part of the coordinate space distributions is at least an order of magnitude smaller than the corresponding real part, and zero within errors in most cases, a proper treatment of the imaginary part has to be found. In this thesis, the imaginary part is treated as systematic uncertainty. In the cases where $\text{Im}[\tilde{h}_1^{\perp, \overline{\text{MS}}}(z, b_{\perp}, P_z, \mu)]$ is not compatible with zero within errors, the Fourier transformation is performed twice, omitting and including the imaginary part. The result from the transformation without $\text{Im}[\tilde{h}_1^{\perp, \overline{\text{MS}}}(z, b_{\perp}, P_z, \mu)]$ is used as mean value for the following analysis, while the difference between both cases is viewed as systematic uncertainty.

As an example, fig. 5.11 shows the renormalized quasi-Boer-Mulders function $\tilde{h}_1^{\perp, \overline{\text{MS}}}(x, b_{\perp}, P_z, \mu)$ in momentum space for N203, $P_z = 1.21$ GeV and $b_{\perp} = 3a$. The resulting momentum space distribution after Fourier transforming without and with the imaginary part are shown in turquoise and pink, respectively. The difference between both cases is largest for large x .

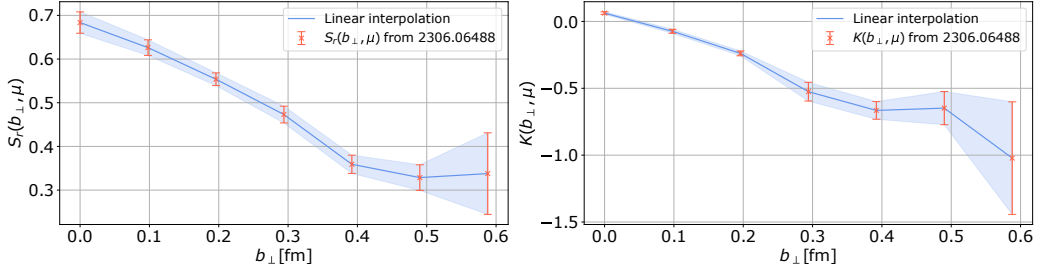


Figure 5.12: Reduced soft function $S_r(b_\perp, \mu)$ (left) and Collins-Soper Kernel $K(b_\perp, \mu)$ (right) from [40] calculated for X650 at one-loop and scale $\mu = 2 \text{ GeV}$. Statistical errors are used for both quantities. The results from linear interpolation are shown in blue.

5.7 Light-cone quark Boer-Mulders function of the pion

The final results for the pion Boer-Mulders function on the light-cone are attained by matching the renormalized quasi-distributions $\tilde{h}_1^{\perp, \overline{\text{MS}}}(z, b_\perp, \mu, \xi_z)$ in momentum space to the light-cone distributions according to eq. (3.47) and dividing by b_\perp and by the pion mass m_π . Note that the dependence of the renormalized quasi-distributions on the momentum P_z has been substituted with a dependence on the Collins-Soper scale $\zeta_z = (2xP_z)^2$.

5.7.1 Reduced soft function and Collins-Soper kernel

The matching to the light-cone involves the Collins-Soper kernel $K(b_\perp, \mu)$ and reduced soft function $S_r(b_\perp, \mu)$ that were introduced in sections 3.5.3 and 3.5.4, respectively. In this work, the results for both quantities are taken from the one-loop calculation on X650 with scale $\mu = 2 \text{ GeV}$ in [40]. The data with statistical errors from [40] is shown in fig. 5.12 in red. Since CLS ensembles with three different lattice spacings are used in the calculation of the Boer-Mulders function of the pion in this thesis, a linear interpolation of $S_r(b_\perp, \mu)$ and $K(b_\perp, \mu)$ is performed to access those quantities at all values of b_\perp that are needed to match the quasi-distributions to the light-cone. The results of the linear interpolation are shown in blue in fig. 5.12. Systematic uncertainties of $K(b_\perp, \mu)$ that are quoted in [40] are not included here.

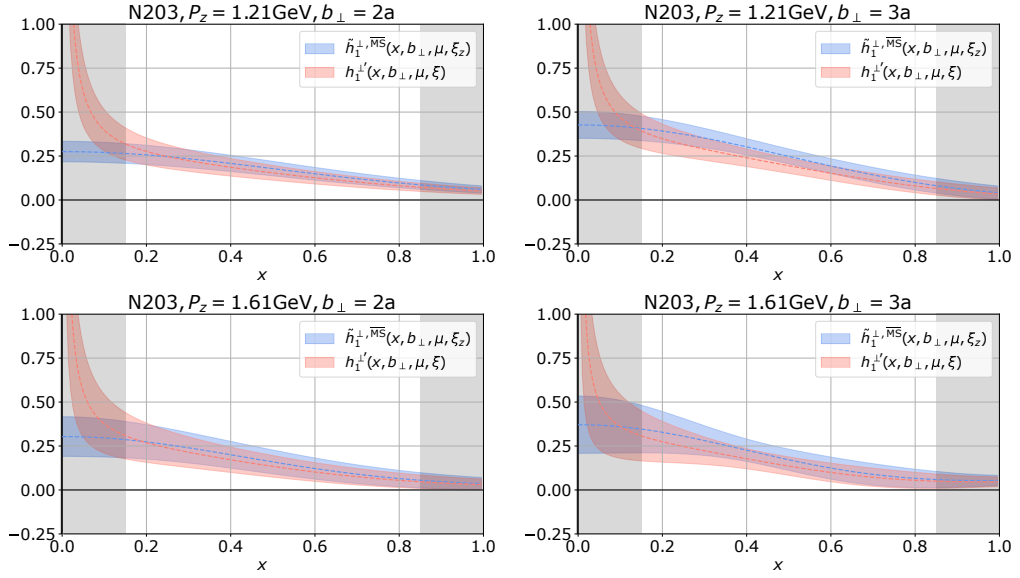


Figure 5.13: Comparison of the quasi-TMDPDF $\tilde{h}_1^{\perp, \overline{\text{MS}}}(x, b_{\perp}, \mu, \zeta_z)$ before matching and the light-cone distribution $h_1^{\perp'}(x, b_{\perp}, \mu, \zeta)$ after matching according to eq. (3.47). The quantity $h_1^{\perp'}(x, b_{\perp}, \mu, \zeta)$ is not yet divided by $b_{\perp} m_{\pi}$. Shown are N203, $P_z = 1.21$ GeV, $b_{\perp} = 2a$ (upper left) and $b_{\perp} = 3a$ (upper right) as well as $P_z = 1.61$ GeV, $b_{\perp} = 2a$ (lower left) and $b_{\perp} = 3a$ (lower right). The regions $x \in [0, 0.15]$ and $x \in [0.85, 1]$ are shaded in gray to indicate the range where the LaMET factorization becomes unreliable due to power corrections.

5.7.2 Comparison of results before and after matching to the light-cone

The comparison of the quasi-TMDPDF $\tilde{h}_1^{\perp, \overline{\text{MS}}}(x, b_{\perp}, \mu, \zeta_z)$ and the light-cone quantity $h_1^{\perp'}(x, b_{\perp}, \mu, \zeta)$ is shown in fig. 5.13 for N203, $P_z = 1.21$ GeV, $b_{\perp} = 2a$ (upper left) and $b_{\perp} = 3a$ (upper right) as well as $P_z = 1.61$ GeV, $b_{\perp} = 2a$ (lower left) and $b_{\perp} = 3a$ (lower right). The result $h_1^{\perp'}(x, b_{\perp}, \mu, \zeta)$ after matching is obtained using eq. (3.47) with rapidity scale $\zeta = 4 \text{ GeV}^2$ and is not yet divided by $b_{\perp} m_{\pi}$. The errors of the quasi-distribution in the figure contain statistical errors as well as the uncertainty from the scale variation in the renormalization group resummation for determining the renormalization factor. The errors of the light-cone results $h_1^{\perp'}(x, b_{\perp}, \mu, \zeta)$ additionally contain uncertainties from the reduced soft function and Collins-Soper kernel. In the case of $P_z = 1.61$ GeV, $b_{\perp} = 3a$, the systematic uncertainty from including the imaginary part of the renormalized matrix element in the Fourier transformation to momentum space is also incorporated. The regions $x \in [0, 0.15]$ and $x \in [0.85, 1]$ are shaded in gray to indicate the range where the LaMET factorization becomes unreliable, see section 3.3.1. The maximum momentum $P_z = 1.84$ GeV was inserted in eq. (3.9) and through rounding conservatively, the range of valid x was estimated.

As can be seen from fig. 5.13, the matching mainly affects the results in the small- x region, while results before and after matching are compatible within errors in the region where the LaMET factorization is reliable.

5.7.3 Momentum dependence of the light-cone Boer-Mulders function

In LaMET calculations, convergence of the results with increasing P_z is crucial to ensure that the momenta used in the calculations are large enough for the LaMET factorization to be valid. The momentum dependence of the Boer-Mulders function $h_1^{\perp}(x, b_{\perp}, \mu, \zeta)$ at renormalization scale $\mu = 2$ GeV and rapidity scale $\zeta = 4 \text{ GeV}^2$ after matching according to eq. (3.47) and dividing by $b_{\perp} m_{\pi}$ is shown in fig. 5.14, fig. 5.15 and fig. 5.16 for X650, H102 and N203, respectively. The errors include statistical as well as systematic uncertainties, which will be discussed in 5.7.4.

For better visibility, the largest momentum $P_z = 1.84$ GeV for X650 is not included in fig. 5.14 due to its significant errors. The data at $P_z = 1.84$ GeV is fully compatible with the results for $P_z = 1.58$ GeV, thus no information would be gained by displaying the data for the largest momentum.

Also note that the smallest momentum $P_z = 0.81$ GeV for N203 is calcu-

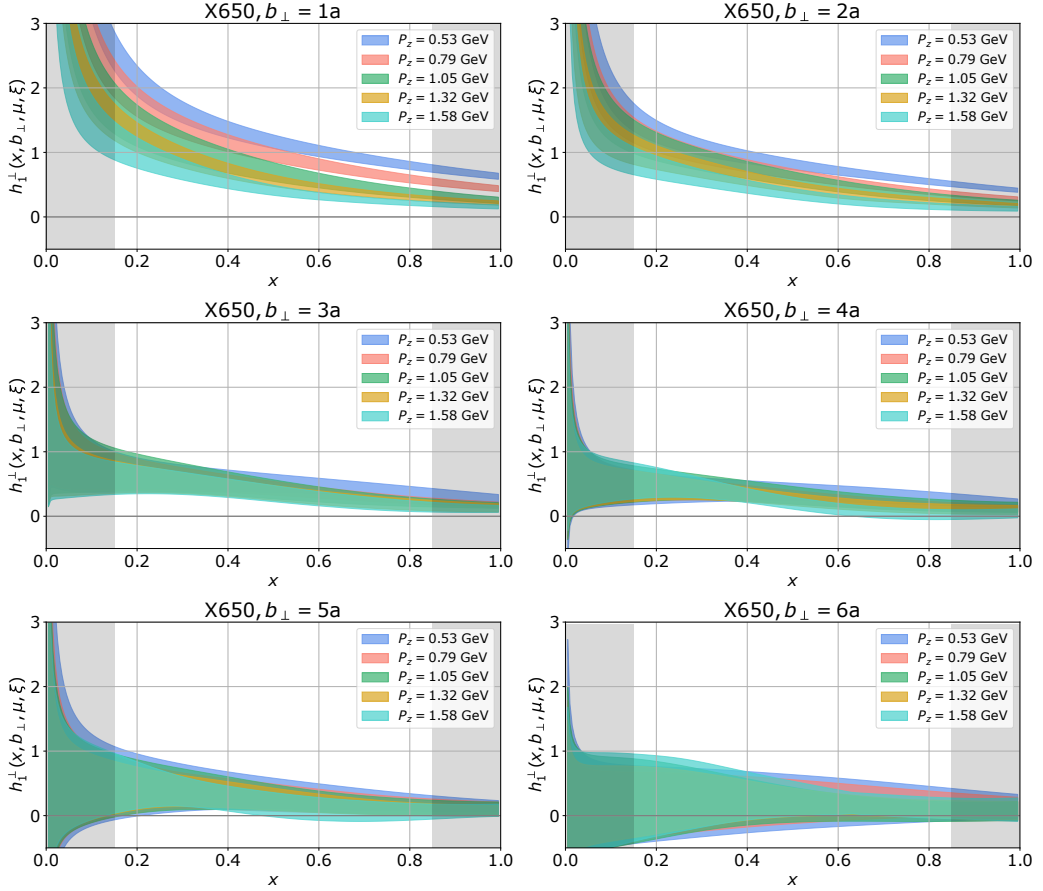


Figure 5.14: The momentum dependence of the extracted light-cone Boer-Mulders function $h_1^\perp(x, b_\perp, \mu, \zeta)$ at scales $\mu = 2 \text{ GeV}$ and $\zeta = 4 \text{ GeV}^2$ on X650 for $b_\perp = \{1, 2, 3, 4, 5, 6\}a$. The regions $x \in [0, 0.15]$ and $x \in [0.85, 1]$ are shaded in gray to indicate the range where the LaMET factorization becomes unreliable. Statistical and systematic uncertainties are included in the errors.

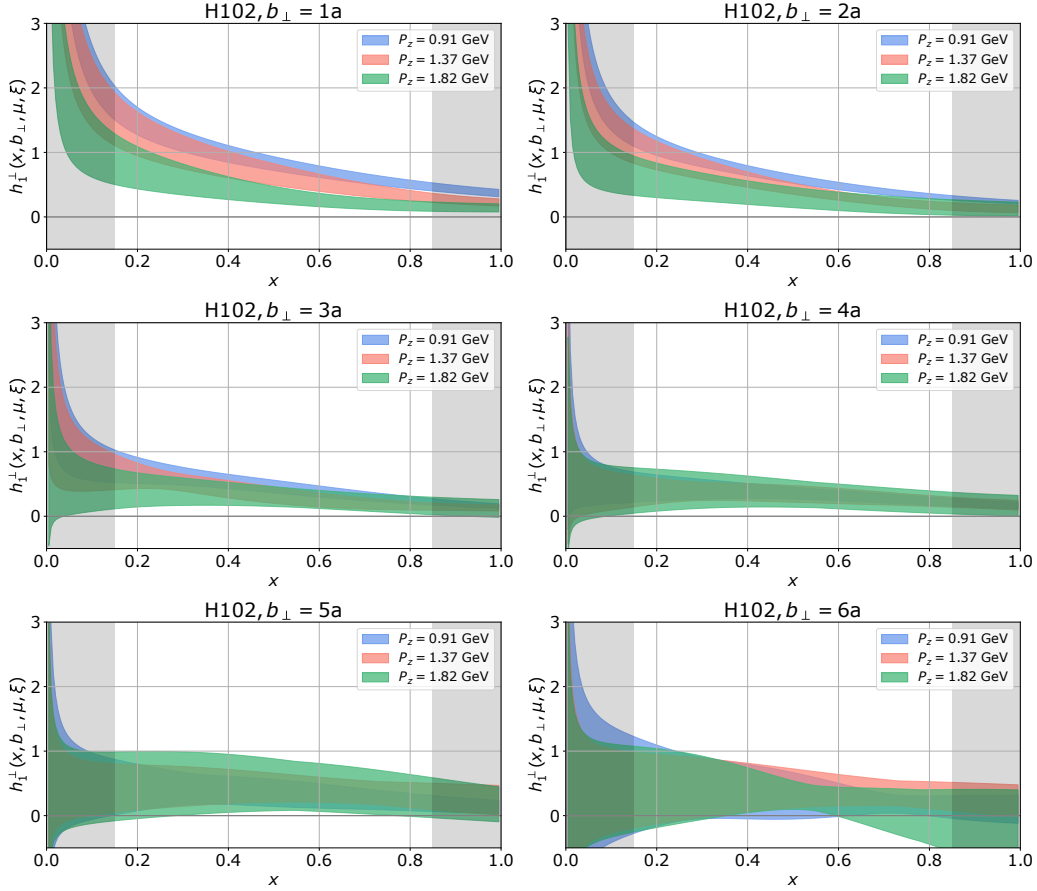


Figure 5.15: The momentum dependence of the extracted light-cone Boer-Mulders function $h_1^\perp(x, b_\perp, \mu, \zeta)$ at scales $\mu = 2 \text{ GeV}$ and $\zeta = 4 \text{ GeV}^2$ on H102 for $b_\perp = \{1, 2, 3, 4, 5, 6\}a$. The regions $x \in [0, 0.15]$ and $x \in [0.85, 1]$ are shaded in gray to indicate the range where the LaMET factorization becomes unreliable. Statistical and systematic uncertainties are included in the errors.

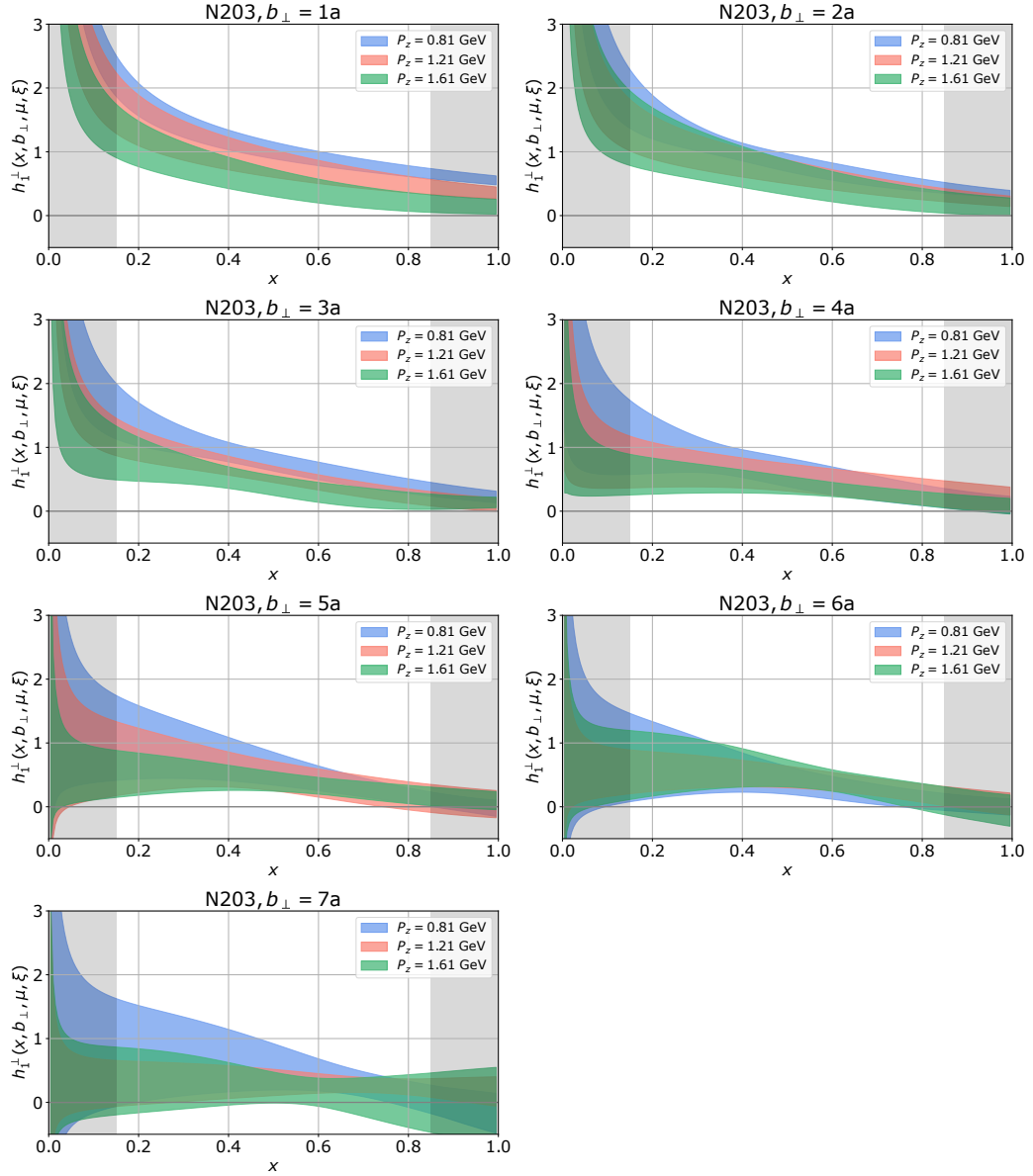


Figure 5.16: The momentum dependence of the extracted light-cone Boer-Mulders function $h_1^\perp(x, b_\perp, \mu, \zeta)$ at scales $\mu = 2$ GeV and $\zeta = 4$ GeV² on N203 for $b_\perp = \{1, 2, 3, 4, 5, 6, 7\}a$. The regions $x \in [0, 0.15]$ and $x \in [0.85, 1]$ are shaded in gray to indicate the range where the LaMET factorization becomes unreliable. Statistical and systematic uncertainties are included in the errors.

lated with limited statistics (see tab. 5.1) compared to the other momenta of N203 to save computing resources. This explains the increased errors for $P_z = 0.81$ GeV that are especially prominent in the results for $b_\perp \geq 3a$ in fig. 5.16.

Overall, good convergence of the pion Boer-Mulders function with increasing P_z is found. Some cases with small b_\perp are exceptions, with X650, $b_\perp = 1a$ being the most notable occurrence of not fully convergent behavior. Discretization effects become important for this coarse lattice and small b_\perp , explaining the lack of convergence. Generally, the errors increase rapidly with larger P_z , while the case of N203 with $P_z = 0.81$ GeV is an exception to this trend due to the already mentioned smaller statistics. For most cases, $h_1^\perp(x, b_\perp, \mu, \zeta)$ is compatible with zero at $x = 1$ within errors for the largest momenta displayed in fig. 5.14, fig. 5.15, and fig. 5.16 for each ensemble. Exceptions are the case of $b_\perp = 1a$ for all ensembles and $b_\perp = \{2, 3\}a$ for X650. That is again attributed to discretization effects, which are especially large for the coarse lattice of X650. Overall, the Boer-Mulders function decays to zero with increasing b_\perp , which is the expected behavior (see the discussion about the b_\perp -dependence of the Boer-Mulders function in section 5.7.5).

5.7.4 Estimation of systematic uncertainties

As already mentioned in section 5.7.2, the determination of the pion Boer-Mulders function $h_1^\perp(x, b_\perp, \mu, \zeta)$ does not only consider statistical errors, but also systematic uncertainties from different sources, including

- the propagation of the error of the reduced soft function from [40] (section 5.7.1),
- the propagation of the error of the Collins-Soper kernel from [40] (section 5.7.1),
- varying the scale in the renormalization group resummation for the determination of the renormalization factors (section 5.4.3),
- including the non-zero imaginary part of the renormalized matrix elements in the Fourier transformation (section 5.6).

As an example for comparing the statistical and systematic errors, fig. 5.17 shows the ratios of different uncertainties and the central value of the light-cone Boer-Mulders function for N203 at $b_\perp = 3a$ and $P_z = 1.21$ GeV. The statistical error is the dominating one, and both the statistical uncertainty as well as the uncertainty from including $\text{Im}[\tilde{h}_1^{\perp, \overline{\text{MS}}}]$ in the Fourier transformation increase for large x .

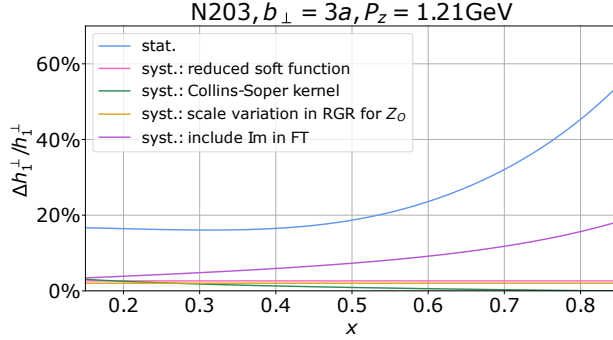


Figure 5.17: Ratios of various uncertainties and central value of the light-cone Boer-Mulders function for N203 at $b_{\perp} = 3a$ and $P_z = 1.21$ GeV. Included are the statistical error as well as systematic uncertainties from: (1) reduced soft function [40], (2) Collins-Soper kernel [40], (3) scale variation in the RGR for determining Z_O , and (4) including $\text{Im}[\tilde{h}_1^{\perp, \overline{\text{MS}}}]$ in the Fourier transformation.

5.7.5 Fit of the b_{\perp} -dependence

One goal of this project is the comparison of the Boer-Mulders function for CLS ensembles with $m_{\pi} \approx 340 - 350$ GeV and different lattice spacings. However, comparing $h_1^{\perp}(x, b_{\perp}, \mu, \zeta)$ calculated at different a is not straightforward, as the values of b_{\perp} available for different gauge ensembles are not equal in physical units. To fit the b_{\perp} -dependence of the Boer-Mulders function and interpolate it, two different fit forms are selected:

$$h_1^{\perp}(x, b_{\perp}) = c_1(x, P_z, a) e^{-c_2(x, P_z, a) \cdot b_{\perp}^2} \quad (5.18)$$

$$h_1^{\perp}(x, b_{\perp}) = \frac{c_1(x, P_z, a)}{\cosh[c_2(x, P_z, a) \cdot b_{\perp}]} \quad (5.19)$$

Eq. (5.18), which is guided by the global fits of the Pavia group e.g. in [156], will be referred to as 'gauß' and eq. (5.19), which is inspired by [132], will be referred to as 'cosh' in the following. The chosen fit forms are simplified compared to the ones in [156] and [132], since the quality of the data and the number of different b_{\perp} in this work do not allow for a fit with more parameters. The fit is performed for each ensemble and momentum individually, as well as for various values of x with step size 0.005. This leads to the parameters c_1 and c_2 being dependent on a , P_z and x , while the remaining dependence of the Boer-Mulders function on P_z and a is not made explicit on the l.h.s. of eqs. (5.18) and (5.19).

Fig. 5.18 shows the fit of the b_{\perp} -dependence of the Boer-Mulders function calculated on X650 with $P_z = 1.58$ GeV and $x = \{0.2, 0.3, 0.4, 0.5, 0.6, 0.7\}$

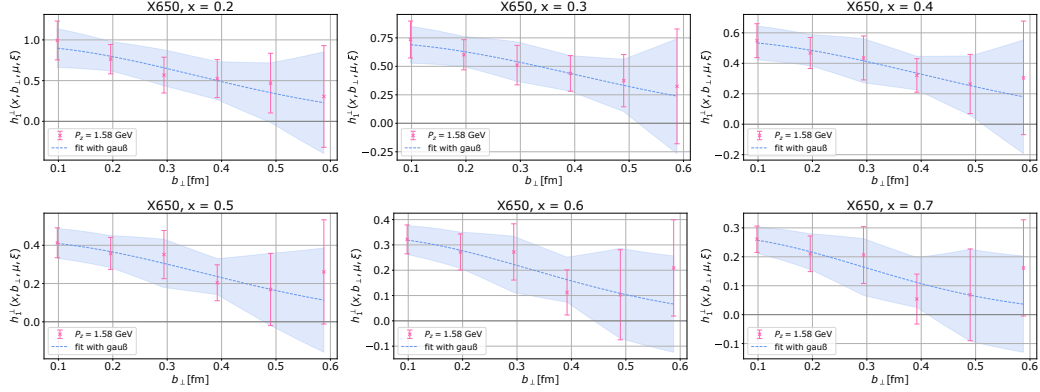


Figure 5.18: Fits of the b_{\perp} -dependence of the Boer-Mulders function calculated on X650 with $P_z = 1.58$ GeV and $x = \{0.2, 0.3, 0.4, 0.5, 0.6, 0.7\}$. Eq. (5.18) is used to fit the lattice data shown in pink. The fit results are shown as dashed blue lines, while the shaded blue regions depict a linear interpolation of the errors from the lattice determination of $h_1^{\perp}(x, b_{\perp}, \mu, \zeta)$. Statistical and systematic uncertainties are included in the errors.

using eq. (5.18). Since the error bars of $h_1^{\perp}(x, b_{\perp}, \mu, \zeta)$ include both statistical and systematic errors, an uncorrelated fit of the b_{\perp} -dependence is performed. In order to not artificially reduce the errors of the Boer-Mulders function, the uncertainties of $h_1^{\perp}(x, b_{\perp}, \mu, \zeta)$ are linearly interpolated instead of using the error from the fit. As seen from the figure, the Boer-Mulders function calculated on X650 with $P_z = 1.58$ GeV is consistent with zero within errors for $b_{\perp} \gtrsim 0.5$ fm. The fit parameters c_1 and c_2 obtained from the fits shown in fig. 5.16 are given in tab. 5.5. The parameter c_1 is clearly x -dependent, which is expected since the Boer-Mulders function overall decays with $x \rightarrow 1$. The parameter c_2 exhibits larger relative errors compared to c_1 , especially for larger x , and agrees within errors across the different values of x shown in fig. 5.18.

The choice of the fit form does not have a large impact on the results. As an example, fig. 5.19 shows the fit of the b_{\perp} -dependence of $h_1^{\perp}(x, b_{\perp}, \mu, \zeta)$ for X650, $P_z = 1.58$ GeV and $x = 0.2$, comparing the fit results using eq. (5.18) ('gauß') and eq. (5.19) ('cosh'). Since, as mentioned above, the error bands result from linear interpolation of the uncertainties of the lattice Boer-Mulders function, they are identical for both fits. The difference in the fit result is negligible and fits with eq. (5.18) ('gauß') are used to compare the Boer-Mulders function of different ensembles in section 5.7.6.

x	c_1	c_2
0.2	0.93(15)	4.06(77)
0.3	0.71(11)	3.16(63)
0.4	0.55(8)	3.22(82)
0.5	0.42(6)	3.82 ± 1.24
0.6	0.33(5)	4.68 ± 1.73
0.7	0.27(4)	5.82 ± 2.06

Table 5.5: Results for the fit parameters c_1 and c_2 from fitting the b_\perp -dependence of the Boer-Mulders function for X650 and $P_z = 1.58$ GeV for various values of x with eq. (5.18). The corresponding fits are shown in fig. 5.18

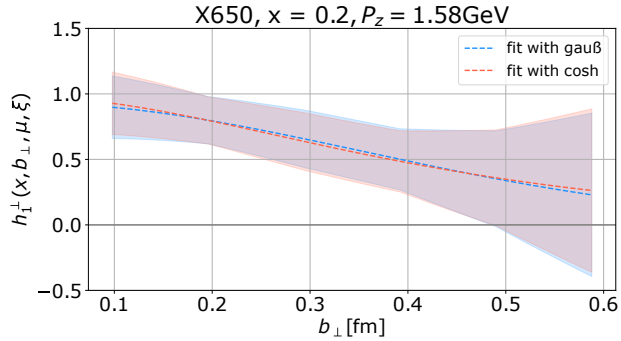


Figure 5.19: Fit of the b_\perp -dependence of $h_1^\perp(x, b_\perp, \mu, \zeta)$ for X650, $P_z = 1.58$ GeV and $x = 0.2$, comparing the fit results using eq. (5.18) ('gauß', shown in blue) and eq. (5.19) ('cosh', shown in orange). The error bands result from linear interpolation of the uncertainties of the lattice Boer-Mulders function, thus being equal for both fits. Statistical and systematic uncertainties are included in the errors.

5.7.6 Lattice spacing dependence of the light-cone Boer-Mulders function

After fitting the b_{\perp} -dependence of the light-cone Boer-Mulders function with eq. (5.18) as described in section 5.7.5, the results of $h_{\perp}^{\perp}(x, b_{\perp}, \mu, \zeta)$ can be compared for different ensembles.

Fig. 5.20 shows $h_{\perp}^{\perp}(x, b_{\perp}, \mu, \zeta)$ at scales $\mu = 2 \text{ GeV}$ and $\zeta = 4 \text{ GeV}^2$ for X650 with $P_z = 1.58 \text{ GeV}$, for H102 with $P_z = 1.37 \text{ GeV}$ and for N203 with $P_z = 1.21 \text{ GeV}$. Values of $b_{\perp} = \{0.1, 0.2, 0.3, 0.4, 0.5\} \text{ fm}$ are chosen for display. The regions $x \in [0, 0.15]$ and $x \in [0.85, 1]$ are shaded in gray to indicate the range where the LaMET factorization becomes unreliable due to power corrections. Statistical and systematic uncertainties are included in the errors, see section 5.7.4 for sources of systematic uncertainties. For better visibility, the second largest momentum is chosen for display for each ensemble. The data for the larger momenta of $P_z = 1.84 \text{ GeV}$ for X650, $P_z = 1.82 \text{ GeV}$ for H102 and $P_z = 1.61 \text{ GeV}$ for N203 exhibit large uncertainties, while overall being compatible with the data for smaller momenta, see section 5.7.3. As seen from fig. 5.20, the results for different ensembles agree with each other within uncertainties. The Boer-Mulders function $h_{\perp}^{\perp}(x, b_{\perp}, \mu, \zeta)$ for different ensembles decays to zero for $b_{\perp} \approx 0.4 - 0.5 \text{ fm}$

5.7.7 Combined infinite momentum and continuum extrapolation

The different lattice spacings and pion momenta used in the calculation of the light-cone Boer-Mulders function $h_{\perp}^{\perp}(x, b_{\perp}, \mu, \zeta)$ of the pion enable an extrapolation to infinite momentum as well as to the continuum, ensuring the validity of the LaMET factorization formula and removing lattice artifacts. As for the extrapolation of the isovector quark transversity PDF of the proton described in section 4.7.2, disentangling the P_z -dependence and a -dependence is not directly possible. Therefore, a combined extrapolation with the following form is used

$$h_{\perp}^{\perp}(x, b_{\perp}, P_z, a) = h_{\perp,0}^{\perp}(x, b_{\perp}) + a^2 f(x, b_{\perp}) + a^2 P_z^2 h(x, b_{\perp}) + \frac{g(x, b_{\perp}, a)}{P_z^2}, \quad (5.20)$$

where $h_{\perp}^{\perp}(x, b_{\perp}, P_z, a)$ on the l.h.s. is the light-cone Boer-Mulders function for different lattice spacings and pion momenta, obtained for specific values of b_{\perp} by fitting the b_{\perp} -dependence as described in section 5.7.5 with eq. (5.18). Discretization effects are accounted for by the terms $a^2 f(x, b_{\perp})$ and

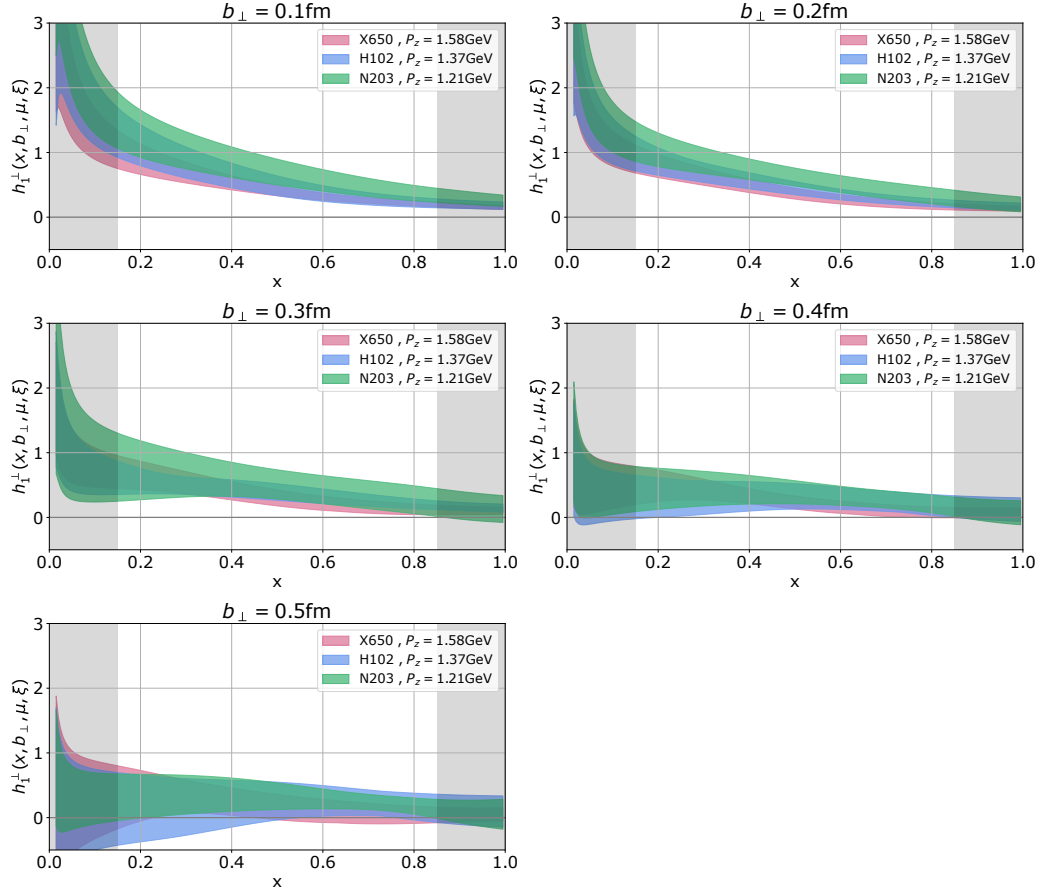


Figure 5.20: Comparison of the extracted light-cone Boer-Mulders function for different ensembles. $h_1^\perp(x, b_\perp, \mu, \zeta)$ at scales $\mu = 2 \text{ GeV}$ and $\zeta = 4 \text{ GeV}^2$ is shown for X650 with $P_z = 1.58 \text{ GeV}$, for H102 with $P_z = 1.37 \text{ GeV}$ and for N203 with $P_z = 1.21 \text{ GeV}$. The results are obtained by fitting the b_\perp -dependence of $h_1^\perp(x, b_\perp, \mu, \zeta)$ with eq. (5.18), and values of $b_\perp = \{0.1, 0.2, 0.3, 0.4, 0.5\} \text{ fm}$ are chosen for display. The regions $x \in [0, 0.15]$ and $x \in [0.85, 1]$ are shaded in gray to indicate the range where the LaMET factorization becomes unreliable due to power corrections. Statistical and systematic uncertainties are included in the errors.

$a^2 P_z^2 h(x, b_\perp)$, while $g(x, b_\perp, a)/P_z^2$ specifies the dependence of the power correction on P_z . An explicit a -dependence is kept in the parameter $g(x, b_\perp, a)$. The final result for the Boer-Mulders function after extrapolation is given by $h_{1,0}^\perp(x, b_\perp)$.

The extrapolation form in eq. (5.20) is the same as in the case of extrapolating the transversity PDF to the infinite momentum, physical pion mass and continuum limit using eq. (4.27), except that in eq. (5.20) all parameters also depend on b_\perp and the pion mass dependence is not considered for the Boer-Mulders function. Including the dependence on m_π is not necessary in the case of the ensembles X650, H102 and N203 with almost equal pion masses. Extrapolating to the physical pion mass would require a calculation of the Boer-Mulders function for at least two additional gauge ensembles with significantly different pion masses, which goes beyond the scope of the present study. Also, when considering the mild pion mass dependence of the transversity PDF as shown in section 4.7.1, an extrapolation to the physical pion mass is not expected to substantially alter the final results of the Boer-Mulders function.

The fit of the Boer-Mulders function with eq. (5.20) is performed for 200 values of x between 0 and 1, and for all bootstrap samples. All pion momenta (except the zero momentum data) and lattice spacings that are given in tab. 5.1 are used for the extrapolation. Fig. 5.21 shows the resulting fit parameters with bootstrap errors for $b_\perp = 0.2$ fm (left) and $b_\perp = 0.4$ fm (right). Since the parameter $g(x, b_\perp, a)$ explicitly depends on a , different parameters $g_1(x, b_\perp)$, $g_2(x, b_\perp)$ and $g_3(x, b_\perp)$ are depicted in the figure, corresponding to $a = \{0.098, 0.085, 0.064\}$ fm, respectively. As seen in fig. 5.21, the parameter $f(x, b_\perp)$ is the smallest compared to the other parameters. For $b_\perp = 0.2$ fm, the parameters $h(x, b_\perp)$ and $g_{1,2,3}(x, b_\perp)$ are of notable size with significant errors, while for $b_\perp = 0.4$ fm their values and uncertainties decrease considerably. This might indicate discretization effects being present for smaller values of b_\perp .

Fig. 5.22 shows the uncertainty from the combined infinite momentum and continuum extrapolation of the light-cone Boer-Mulders function $h_1^\perp(x, b_\perp, \mu, \zeta)$ with eq. (5.20), which is calculated by subtracting the extrapolated result from the result for N203, $P_z = 1.61$ GeV, for $b_\perp = 0.2$ fm (left) and $b_\perp = 0.4$ fm (right). The uncertainty from the extrapolation is compared to the statistical error obtained from the bootstrap samples, and the systematic error composed as described in section 5.7.4. The systematic uncertainty of the extrapolated result, which is shown in blue in fig. 5.22, is calculated as the difference between the extrapolated result and the fit result with the systematic error being added to the data before fitting. All uncertainties are shown as non-overlapping bands. As seen from the figure,

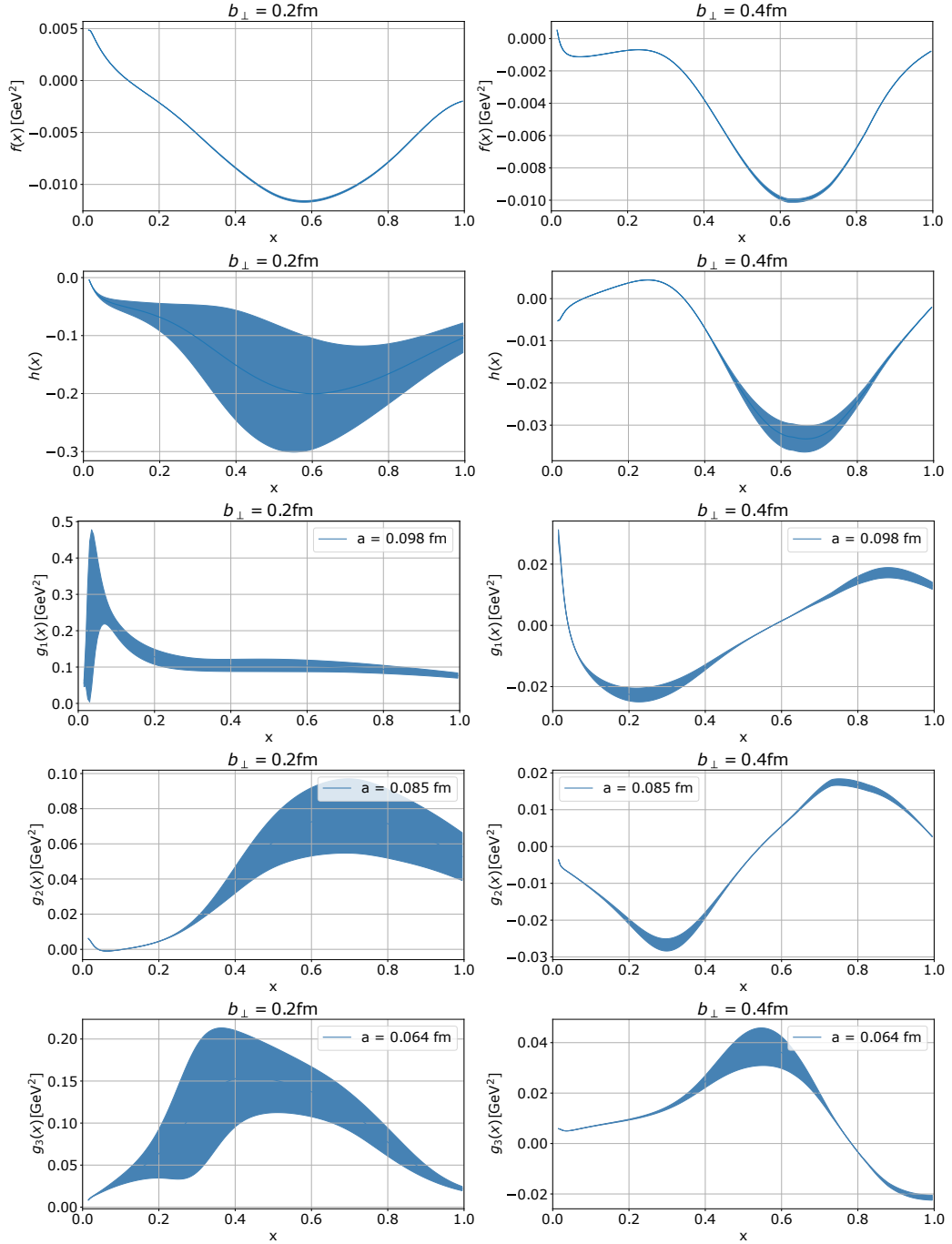


Figure 5.21: Fit parameters $f(x, b_\perp)$, $h(x, b_\perp)$, $g_1(x, b_\perp)$, $g_2(x, b_\perp)$ and $g_3(x, b_\perp)$ for $b_\perp = 0.2$ fm (left) and $b_\perp = 0.4$ fm (right) resulting from fitting the light-cone Boer-Mulders function with eq. (5.20). The fit allows for the parameter $g(x, b_\perp, a)$ to depend on a , yielding the parameters $g_1(x, b_\perp)$, $g_2(x, b_\perp)$ and $g_3(x, b_\perp)$ for $a = \{0.098, 0.085, 0.064\}$ fm, respectively.

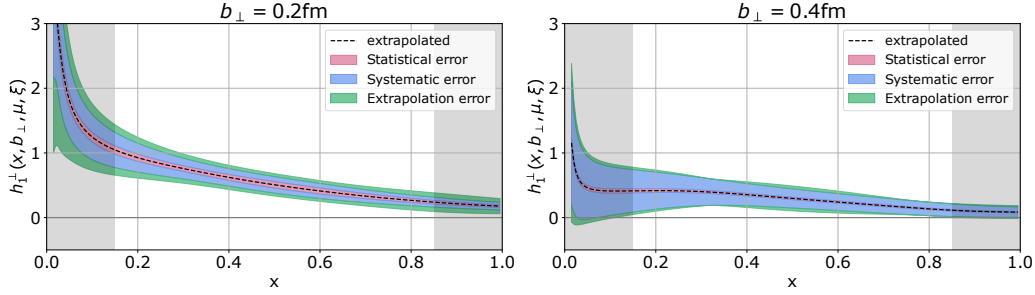


Figure 5.22: Demonstration of the uncertainty resulting from the combined infinite momentum and continuum extrapolation of the light-cone Boer-Mulders function $h_1^\perp(x, b_\perp, \mu, \zeta)$ with eq. (5.20) for $b_\perp = 0.2$ fm (left) and $b_\perp = 0.4$ fm (right). The uncertainty from the extrapolation is obtained as the difference between the extrapolated result and the light-cone Boer-Mulders function for N203, $P_z = 1.61$ GeV, and put in relation to the statistical error and the systematic error, which includes the different sources of uncertainties listed in section 5.7.4. All uncertainties are depicted as non-overlapping bands. The regions $x \in [0, 0.15]$ and $x \in [0.85, 1]$ are shaded in gray to indicate the range where the LaMET factorization becomes unreliable due to power corrections.

the error from extrapolating to the infinite momentum and continuum limit is larger for smaller values of b_\perp .

The final results for the light-cone Boer-Mulders function $h_1^\perp(x, b_\perp, \mu, \zeta)$ at scales $\mu = 2$ GeV and $\zeta = 4$ GeV² after extrapolation to infinite momentum and to the continuum are shown in fig. 5.23 for $b_\perp = \{0.1, 0.2, 0.3, 0.4, 0.5\}$ fm, together with the results for $h_1^\perp(x, b_\perp, \mu, \zeta)$ that were shown in fig. 5.20. The uncertainties of the extrapolated results are obtained by adding the statistical (bootstrap) error, the error from extrapolating, and the combined systematic error, all of which are shown in fig. 5.22 for $b_\perp = \{0.2, 0.4\}$ fm, in quadrature.

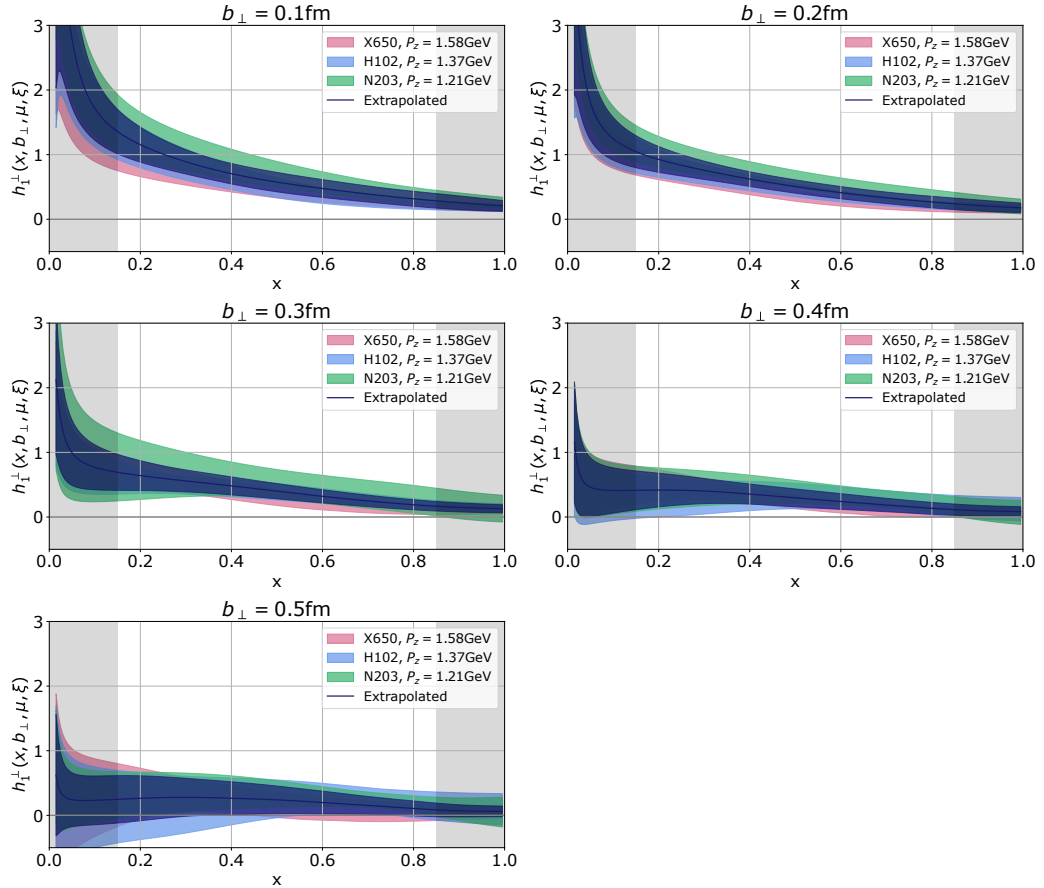


Figure 5.23: Final results for the light-cone Boer-Mulders function at scales $\mu = 2 \text{ GeV}$ and $\zeta = 4 \text{ GeV}^2$ after infinite momentum and continuum extrapolation with eq. (5.20), together with $h_1^\perp(x, b_\perp, \mu, \zeta)$ for different ensembles as already shown in fig. 5.20. The errors include the statistical uncertainty, the systematic errors as listed in section 5.7.4, and the uncertainty from extrapolating, obtained as the difference from the extrapolated result and the light-cone Boer-Mulders function for N203, $P_z = 1.61 \text{ GeV}$. The regions $x \in [0, 0.15]$ and $x \in [0.85, 1]$ are shaded in gray to indicate the range where the LaMET factorization becomes unreliable due to power corrections.

Chapter 6

Conclusion and Outlook

In this thesis, the author has presented two independent projects both aiming for a better understanding of the internal transverse spin structure of hadrons. Two different distribution functions which are relatively unknown from experiments were calculated in the framework of large-momentum effective theory [43, 44, 66].

As presented in chapter 4, the isovector quark transversity distribution $\delta u(x) - \delta d(x)$ in the proton was calculated for CLS ensembles with four different lattice spacings $a = \{0.098, 0.085, 0.064, 0.049\}$ fm and pion masses between 220 MeV and 350 MeV with proton momenta up to 2.8 GeV. The bare matrix elements were fitted using a two-state combined fit of the two-point function and ratio of three-point and two-point function. Renormalization was performed in the hybrid scheme, and an extrapolation for large quasi-light-front distances was used to avoid unphysical oscillations in the momentum space. After Fourier transforming the data, the light-cone transversity PDF was obtained with NLO matching for various different lattice spacings, pion masses and proton momenta P_z , allowing to study dependencies of the data on those parameters. Good convergence of the results with increasing P_z is found, which is crucial for the LaMET factorization to be valid. The pion mass dependence is only very mild. Discretization effects are found to be important for the coarsest lattice of X650, while the other ensembles show convergent behavior with decreasing values of the lattice spacing a . Since it is not possible to completely disentangle the dependence on a and P_z , a combined infinite momentum, physical pion mass and continuum extrapolation was performed as described in section 4.7.2. The final result for the isovector quark transversity PDF, which includes various sources of statistical and systematic uncertainties, lies between the global fits of experimental data from JAM20 [81] and JAM22 [70], agreeing within 2σ with both results, thus constituting a reliable prediction of the transversity PDF from lattice

QCD.

The nucleon isovector tensor charge (first Mellin moment) was extracted as a consistency check from the local matrix elements. The result of $g_T = 1.018(68)$ given in section 4.23 was obtained by extrapolating to the continuum and physical pion mass and agrees well with the Mainz19 [82], FLAG21 [85] and other recent results [86, 84, 83].

This extraction of the isovector quark transversity distribution in the proton was published in [42]. The author of this thesis is one of the main authors of the publication and the project was done in close collaboration with the co-authors.

The second project presented in this thesis is a natural extension of the transversity PDF calculation and is also using the LaMET framework. The work described in chapter 5 is the first lattice QCD extraction of the quark Boer-Mulders function $h_1^\perp(x, b_\perp)$ of the pion, which is one of the eight leading twist transverse momentum dependent PDFs, and thus additionally depends on the Fourier conjugate b_\perp of the transverse momentum k_\perp . The calculations were performed for CLS ensembles with three different lattice spacings $a = \{0.098, 0.085, 0.064\}$ fm and almost constant pion mass $m_\pi \approx \{340 - 350\}$ MeV with pion momenta up to 1.84 GeV. Two-point and three-point functions were calculated, where the latter involve a staple-shaped gauge link with width b_\perp and longitudinal extent L , see section 5.2. The bare matrix elements were extracted by fitting the two-point function and ratio of three-point and two-point function with the same functional form as in the PDF case, however the number of fits performed is larger due to the additional parameter b_\perp . As described in section 5.4, the square root of a rectangular Euclidean Wilson loop was used to eliminate the linear divergence and pinch-pole singularity. A plateau in L was found in the data after division by this square root, see section 5.4.2. Additional renormalization was performed in the short distance ratio scheme, and renormalization group resummation was used when calculating the renormalization factors. The renormalized matrix elements were extrapolated for large quasi-light-front distances and Fourier-transformed to momentum space. The reduced soft function and Collins-Soper kernel from [40] and NLO matching kernel [151, 152, 66] were used to obtain the results for $h_1^\perp(x, b_\perp)$ on the light-cone, see section 5.7. The data is convergent with increasing momentum P_z , except for small values of b_\perp where discretization effects become important. To compare the different ensembles, the b_\perp -dependence of $h_1^\perp(x, b_\perp)$ was fitted as described in section 5.7.5. A controlled extrapolation to infinite momentum and to the continuum was performed as described in section 5.7.7. The Boer-Mulders function decays to zero for $b_\perp \approx 0.4 - 0.5$ fm.

Even though the calculation was performed with up to 790,016 measure-

ments (for N203, $P_z = \{1.21, 1.61\}$ GeV), the uncertainties of the resulting Boer-Mulders function are rather large. However, the determination in this project is of high relevance since the Boer-Mulders function is basically unknown so far, and much more difficult to calculate compared to PDFs, which is why we analyzed the quark Boer-Mulders function in the pion for which the signal-to-noise ratio is expected to be better than for the nucleon. (In fact, ours is the first really successful lattice calculation of this type.). Obviously, a more detailed study of $h_1^\perp(x, b_\perp)$ with larger statistics, higher values of P_z , finer lattices and different pion masses is highly desirable. Currently, work is performed within the Regensburg group of high energy physics¹ for adapting the code to run efficiently on GPUs, which would allow for the required larger scale computer time applications in the future.

¹primarily by Tobias Sizmann and Prof. Dr. Christoph Lehner

Bibliography

- [1] Murray Gell-Mann. “A Schematic Model of Baryons and Mesons”. In: *Phys. Lett.* 8 (1964), pp. 214–215.
- [2] G. Zweig. “An SU(3) model for strong interaction symmetry and its breaking. Version 1”. In: (1964).
- [3] *Proceedings, 14th International Conference on High-Energy Physics (ICHEP 68): Vienna, Austria, 28 Aug-5 Sep, 1968*. Geneva: CERN, 1968.
- [4] Richard P. Feynman. “Very high-energy collisions of hadrons”. In: *Phys. Rev. Lett.* 23 (1969), pp. 1415–1417.
- [5] J. D. Bjorken and Emmanuel A. Paschos. “Inelastic Electron Proton and gamma Proton Scattering, and the Structure of the Nucleon”. In: *Phys. Rev.* 185 (1969), pp. 1975–1982.
- [6] H. Fritzsch, Murray Gell-Mann, and H. Leutwyler. “Advantages of the Color Octet Gluon Picture”. In: *Phys. Lett. B* 47 (1973), pp. 365–368.
- [7] Kenneth G. Wilson. “Confinement of quarks”. In: *Phys. Rev. D* 10 (8 1974), pp. 2445–2459.
- [8] A. Accardi et al. “Electron Ion Collider: The Next QCD Frontier - Understanding the glue that binds us all”. In: *The European Physical Journal A* 52 (2012).
- [9] John C. Collins and Davison E. Soper. “Back-to-back jets in QCD”. In: *Nuclear Physics B* 193.2 (1981), pp. 381–443.
- [10] John C. Collins and Davison E. Soper. “Back-To-Back Jets: Fourier Transform from B to K-Transverse”. In: *Nucl. Phys. B* 197 (1982), pp. 446–476.
- [11] John C. Collins, Davison E. Soper, and George F. Sterman. “Factorization for One Loop Corrections in the Drell-Yan Process”. In: *Nucl. Phys. B* 223 (1983), pp. 381–421.

- [12] Geoffrey T. Bodwin. “Factorization of the Drell-Yan cross section in perturbation theory”. In: *Phys. Rev. D* 31 (10 1985), pp. 2616–2642.
- [13] John C. Collins, Davison E. Soper, and George Sterman. “Factorization for short distance hadron-hadron scattering”. In: *Nuclear Physics B* 261 (1985), pp. 104–142.
- [14] J.C. Collins, Davison E. Soper, and George Sterman. “Transverse momentum distribution in Drell-Yan pair and W and Z boson production”. In: *Nuclear Physics B* 250.1 (1985), pp. 199–224.
- [15] Stanley J. Brodsky. *QCD Phenomenology and Light-Front Wavefunctions*. 2001. arXiv: hep-ph/0111340 [hep-ph].
- [16] Matthias Burkardt, Xiangdong Ji, and Feng Yuan. “Scale dependence of hadronic wave functions and parton densities”. In: *Physics Letters B* 545.3 (2002), pp. 345–351.
- [17] J.P. Ma and Q. Wang. “Transverse momentum dependent light-cone wave function of B-meson and relation to the momentum integrated one”. In: *Physics Letters B* 613.1 (2005), pp. 39–44.
- [18] John Collins. “Fragmentation of transversely polarized quarks probed in transverse momentum distributions”. In: *Nuclear Physics B* 396.1 (1993), pp. 161–182.
- [19] S. Mert Aybat and Ted C. Rogers. “Transverse momentum dependent parton distribution and fragmentation functions with QCD evolution”. In: *Phys. Rev. D* 83 (11 2011), p. 114042.
- [20] R. Abdul Khalek et al. “Science Requirements and Detector Concepts for the Electron-Ion Collider”. In: *Nuclear Physics A* 1026 (2022), p. 122447.
- [21] R. Abdul Khalek et al. *Snowmass 2021 White Paper: Electron Ion Collider for High Energy Physics*. 2022. arXiv: 2203.13199 [hep-ph].
- [22] E. D. Bloom et al. “High-Energy Inelastic $e - p$ Scattering at 6° and 10° ”. In: *Phys. Rev. Lett.* 23 (16 1969), pp. 930–934.
- [23] L. Adamczyk et al. “Single spin asymmetry A_N in polarized proton-proton elastic scattering at $\sqrt{s}=200$ GeV”. In: *Physics Letters B* 719.1 (2013), pp. 62–69.
- [24] R. L. Jaffe and Xiangdong Ji. “Chiral-odd parton distributions and polarized Drell-Yan process”. In: *Phys. Rev. Lett.* 67 (5 1991), pp. 552–555.
- [25] R. L. Jaffe and Xiang-Dong Ji. “Chiral odd parton distributions and Drell-Yan processes”. In: *Nucl. Phys. B* 375 (1992), pp. 527–560.

- [26] D. Boer and P. J. Mulders. “Time-reversal odd distribution functions in leptonproduction”. In: *Phys. Rev. D* 57 (9 1998), pp. 5780–5786.
- [27] Yan-Qing Ma and Jian-Wei Qiu. “Exploring Partonic Structure of Hadrons Using ab initio Lattice QCD Calculations”. In: *Phys. Rev. Lett.* 120 (2 2018), p. 022003.
- [28] Constantia Alexandrou et al. “Mellin moments $\langle x \rangle$ and $\langle x^2 \rangle$ for the pion and kaon from lattice QCD”. In: *Physical Review D* 103.1 (2021).
- [29] Marius Löffler et al. “Mellin moments of spin dependent and independent PDFs of the pion and rho meson”. In: *Physical Review D* 105.1 (2022).
- [30] Marcel Rodekamp et al. “Moments of nucleon unpolarized, polarized, and transversity parton distribution functions from lattice QCD at the physical point”. In: *Phys. Rev. D* 109 (7 2024), p. 074508.
- [31] Ph. Hägler et al. “Intrinsic quark transverse momentum in the nucleon from lattice QCD”. In: *EPL (Europhysics Letters)* 88.6 (2009), p. 61001.
- [32] B. U. Musch et al. “Sivers and Boer-Mulders observables from lattice QCD”. In: *Phys. Rev. D* 85 (9 2012), p. 094510.
- [33] M. Engelhardt et al. “Lattice QCD study of the Boer-Mulders effect in a pion”. In: *Physical Review D* 93.5 (2016).
- [34] Boram Yoon et al. “Nucleon transverse momentum-dependent parton distributions in lattice QCD: Renormalization patterns and discretization effects”. In: *Physical Review D* 96.9 (2017).
- [35] Maximilian Schlemmer et al. “Determination of the Collins-Soper Kernel from Lattice QCD”. In: *Journal of High Energy Physics* 2021.8 (2021).
- [36] Qi-An Zhang et al. “Lattice QCD Calculations of Transverse-Momentum-Dependent Soft Function through Large-Momentum Effective Theory”. In: *Physical Review Letters* 125.19 (2020).
- [37] Constantia Alexandrou et al. “Unpolarized and Helicity Generalized Parton Distributions of the Proton within Lattice QCD”. In: *Phys. Rev. Lett.* 125 (26 2020), p. 262001.
- [38] Constantia Alexandrou et al. “Transversity GPDs of the proton from lattice QCD”. In: *Physical Review D* 105.3 (2022).
- [39] He Jinchun et al. “Unpolarized transverse momentum dependent parton distributions of the nucleon from lattice QCD”. In: *Physical Review D* 109 (2024).

- [40] Min-Huan Chu et al. “Lattice calculation of the intrinsic soft function and the Collins-Soper kernel”. In: *Journal of High Energy Physics* 2023.8 (2023).
- [41] Min-Huan Chu et al. “Transverse-momentum-dependent wave functions of the pion from lattice QCD”. In: *Physical Review D* 109 (2024).
- [42] Fei Yao et al. “Nucleon Transversity Distribution in the Continuum and Physical Mass Limit from Lattice QCD”. In: *Phys. Rev. Lett.* 131.26 (2023), p. 261901. arXiv: 2208.08008 [hep-lat].
- [43] Xiangdong Ji. “Parton Physics on a Euclidean Lattice”. In: *Physical Review Letters* 110.26 (2013).
- [44] Xiangdong Ji. “Parton Physics from Large-Momentum Effective Field Theory”. In: *Sci. China Phys. Mech. Astron.* 57 (2014), pp. 1407–1412. arXiv: 1404.6680 [hep-ph].
- [45] L.D. Faddeev and V.N. Popov. “Feynman diagrams for the Yang-Mills field”. In: *Physics Letters B* 25.1 (1967), pp. 29–30.
- [46] William A. Bardeen et al. “Deep-inelastic scattering beyond the leading order in asymptotically free gauge theories”. In: *Phys. Rev. D* 18 (11 1978), pp. 3998–4017.
- [47] Christof Gattringer and Christian B. Lang. *Quantum Chromodynamics on the Lattice: An Inductory Presentation*. Lecture Notes in Physics 788. Springer Berlin Heidelberg, 2010.
- [48] K. Symanzik. “Continuum limit and improved action in lattice theories: (I). Principles and φ^4 theory”. In: *Nuclear Physics B* 226.1 (1983), pp. 187–204.
- [49] K. Symanzik. “Continuum limit and improved action in lattice theories: (II). O(N) non-linear sigma model in perturbation theory”. In: *Nuclear Physics B* 226.1 (1983), pp. 205–227.
- [50] M. Lüscher and P. Weisz. “On-shell improved lattice gauge theories”. In: *Communications in Mathematical Physics* 97.1 (1985), pp. 59–77.
- [51] G. Curci, P. Menotti, and G. Paffuti. “Symanzik’s Improved Lagrangian For Lattice Gauge Theory”. In: *Phys. Lett. B* 103.205 (1983), p. 217.
- [52] B. Sheikholeslami and R. Wohlert. “Improved Continuum Limit Lattice Action for QCD with Wilson Fermions”. In: *Nucl. Phys. B* 259 (1985), p. 572.
- [53] Simon Duane et al. “Hybrid Monte Carlo”. In: *Physics Letters B* 195.2 (1987), pp. 216–222.

- [54] Martin Lüscher and Filippo Palombi. “Fluctuations and reweighting of the quark determinant on large lattices”. In: *PoS LATTICE2008* (2008), p. 049. arXiv: 0810.0946 [hep-lat].
- [55] Martin Lüscher and Stefan Schaefer. “Lattice QCD without topology barriers”. In: *JHEP* 07 (2011), p. 036. arXiv: 1105.4749 [hep-lat].
- [56] Mattia Bruno et al. “Simulation of QCD with $N_f=2+1$ flavors of non-perturbatively improved Wilson fermions”. In: *Journal of High Energy Physics* 02.043 (2015). eprint: 1411.3982.
- [57] R. Babich et al. “Adaptive Multigrid Algorithm for the Lattice Wilson-Dirac Operator”. In: *Physical Review Letters* 105.20 (2010).
- [58] J. C. Osborn et al. “Multigrid solver for clover fermions”. In: *PoS LATTICE2010* (2010), p. 037. arXiv: 1011.2775 [hep-lat].
- [59] G. Martinelli and C.T. Sachrajda. “A lattice study of nucleon structure”. In: *Nuclear Physics B* 316.2 (1989), pp. 355–372.
- [60] S. Güsken et al. “Non-singlet axial vector couplings of the baryon octet in lattice QCD”. In: *Physics Letters B* 227.2 (1989), pp. 266–269.
- [61] Stephan Güsken. “A study of smearing techniques for hadron correlation functions”. In: *Nuclear Physics B - Proceedings Supplements* 17 (1990), pp. 361–364.
- [62] Gunnar S. Bali et al. “Novel quark smearing for hadrons with high momenta in lattice QCD”. In: *Phys. Rev. D* 93 (9 2016), p. 094515.
- [63] M. Falcioni et al. “Again on SU(3) glueball mass”. In: *Nuclear Physics B* 251 (1985), pp. 624–632.
- [64] Anna Hasenfratz and Francesco Knechtli. “Flavor symmetry and the static potential with hypercubic blocking”. In: *Phys. Rev. D* 64 (3 2001), p. 034504.
- [65] Michael Schmelling. “Averaging correlated data”. In: *Phys. Scripta* 51 (1995), pp. 676–679.
- [66] Xiangdong Ji et al. “Large-momentum effective theory”. In: *Reviews of Modern Physics* 93.3 (2021).
- [67] R. P. Feynman. *Photon-hadron interactions*. CRC Press. 1972.
- [68] J. L. Cortes, B. Pire, and J. P. Ralston. “Measuring the transverse polarization of quarks in the proton”. In: *Zeitschrift für Physik C Particles and Fields* 55.3 (1992), pp. 409–416.

- [69] R. L. Jaffe and Xiangdong Ji. “Novel quark fragmentation functions and the nucleon’s transversity distribution”. In: *Phys. Rev. Lett.* 71 (16 1993), pp. 2547–2550.
- [70] Leonard Gamberg et al. “Updated QCD global analysis of single transverse-spin asymmetries: Extracting \tilde{H} , and the role of the Soffer bound and lattice QCD”. In: *Physical Review D* 106.3 (2022).
- [71] M. Anselmino et al. “Transversity and Collins functions from SIDIS and e^+e^- data”. In: *Phys. Rev. D* 75 (5 2007), p. 054032.
- [72] M. Anselmino et al. “Update on transversity and Collins functions from SIDIS and e^+e^- data”. In: *Nuclear Physics B - Proceedings Supplements* 191 (2009). Proceedings of the Ringberg Workshop, pp. 98–107.
- [73] Alessandro Bacchetta, Aurore Courtoy, and Marco Radici. “First Glances at the Transversity Parton Distribution through Dihadron Fragmentation Functions”. In: *Phys. Rev. Lett.* 107 (1 2011), p. 012001.
- [74] Alessandro Bacchetta, A. Courtoy, and Marco Radici. “First extraction of valence transversities in a collinear framework”. In: *Journal of High Energy Physics* 2013.3 (2013), p. 119.
- [75] M. Anselmino et al. “Simultaneous extraction of transversity and Collins functions from new semi-inclusive deep inelastic scattering and e^+e^- data”. In: *Phys. Rev. D* 87 (9 2013), p. 094019.
- [76] Zhong-Bo Kang et al. “Nucleon tensor charge from Collins azimuthal asymmetry measurements”. In: *Phys. Rev. D* 91 (7 2015), p. 071501.
- [77] Marco Radici et al. “Improved extraction of valence transversity distributions from inclusive dihadron production”. In: *Journal of High Energy Physics* 2015.5 (2015), p. 123.
- [78] Zhong-Bo Kang et al. “Extraction of quark transversity distribution and Collins fragmentation functions with QCD evolution”. In: *Physical Review D* 93.1 (2016).
- [79] H.-W. Lin et al. “First Monte Carlo Global Analysis of Nucleon Transversity with Lattice QCD Constraints”. In: *Phys. Rev. Lett.* 120 (15 2018), p. 152502.
- [80] Marco Radici and Alessandro Bacchetta. “First Extraction of Transversity from a Global Analysis of Electron-Proton and Proton-Proton Data”. In: *Phys. Rev. Lett.* 120 (19 2018), p. 192001.
- [81] Justin Cammarota et al. “Origin of single transverse-spin asymmetries in high-energy collisions”. In: *Physical Review D* 102.5 (2020).

- [82] Tim Harris et al. “Nucleon isovector charges and twist-2 matrix elements with $N_f=2+1$ dynamical Wilson quarks”. In: *Physical Review D* 100.3 (2019).
- [83] Nesreen Hasan et al. “Nucleon axial, scalar, and tensor charges using lattice QCD at the physical pion mass”. In: *Physical Review D* 99.11 (2019).
- [84] Michael Abramczyk et al. “Nucleon mass and isovector couplings in 2+1-flavor dynamical domain-wall lattice QCD near physical mass”. In: *Physical Review D* 101.3 (2020).
- [85] Y. Aoki et al. “FLAG Review 2021”. In: *The European Physical Journal C* 82.10 (2022).
- [86] Sungwoo Park et al. “Precision nucleon charges and form factors using (2+1)-flavor lattice QCD”. In: *Physical Review D* 105.5 (2022).
- [87] A. V. Radyushkin. “Quasi-parton distribution functions, momentum distributions, and pseudo-parton distribution functions”. In: *Physical Review D* 96.3 (2017).
- [88] A.V. Radyushkin. “Quark pseudodistributions at short distances”. In: *Physics Letters B* 781 (2018), 433–442.
- [89] Jiunn-Wei Chen, Xiangdong Ji, and Jian-Hui Zhang. “Improved quasi parton distribution through Wilson line renormalization”. In: *Nuclear Physics B* 915 (2017), 1–9.
- [90] A. V. Radyushkin. “Quasi-parton distribution functions, momentum distributions, and pseudo-parton distribution functions”. In: *Physical Review D* 96.3 (2017).
- [91] Constantia Alexandrou et al. “A complete non-perturbative renormalization prescription for quasi-PDFs”. In: *Nuclear Physics B* 923 (2017), 394–415.
- [92] Xiangdong Ji et al. “A hybrid renormalization scheme for quasi light-front correlations in large-momentum effective theory”. In: *Nuclear Physics B* 964 (2021), p. 115311.
- [93] Kostas Orginos et al. “Lattice QCD exploration of parton pseudo-distribution functions”. In: *Phys. Rev. D* 96 (9 2017), p. 094503.
- [94] Anatoly Radyushkin. “One-loop evolution of parton pseudo-distribution functions on the lattice”. In: *Physical Review D* 98.1 (2018).
- [95] Yi-Kai Huo et al. “Self-renormalization of quasi-light-front correlators on the lattice”. In: *Nuclear Physics B* 969 (2021), p. 115443.

- [96] Vladimir M. Braun, Yao Ji, and Alexey Vladimirov. “QCD factorization for chiral-odd parton quasi- and pseudo-distributions”. In: *Journal of High Energy Physics* 2021.10 (2021).
- [97] Chien-Yu Chou and Jiunn-Wei Chen. “One-loop hybrid renormalization matching kernels for quasiparton distributions”. In: *Physical Review D* 106.1 (2022).
- [98] Xiangdong Ji, Jian-Ping Ma, and Feng Yuan. “QCD factorization for spin-dependent cross sections in DIS and Drell–Yan processes at low transverse momentum”. In: *Physics Letters B* 597.3–4 (2004), 299–308.
- [99] Xiangdong Ji, Jian-Ping Ma, and Feng Yuan. “QCD factorization for semi-inclusive deep-inelastic scattering at low transverse momentum”. In: *Physical Review D* 71.3 (2005).
- [100] Thomas Becher and Matthias Neubert. “Drell–Yan production at small q_T , transverse parton distributions and the collinear anomaly”. In: *The European Physical Journal C* 71.6 (2011).
- [101] Jui-Yu Chiu et al. “A formalism for the systematic treatment of rapidity logarithms in Quantum Field Theory”. In: *Journal of High Energy Physics* 2012.5 (2012).
- [102] Miguel G. Echevarria, Ignazio Scimemi, and Alexey Vladimirov. “Transverse momentum dependent fragmentation function at next-to-next-to-leading order”. In: *Physical Review D* 93.1 (2016).
- [103] Miguel G. Echevarria, Ignazio Scimemi, and Alexey Vladimirov. “Universal transverse momentum dependent soft function at NNLO”. In: *Physical Review D* 93.5 (2016).
- [104] Ye Li, Duff Neill, and Hua Xing Zhu. *An Exponential Regulator for Rapidity Divergences*. 2016. arXiv: 1604.00392 [hep-ph].
- [105] Alexey Vladimirov. *Structure of rapidity divergences in soft factors*. 2017. arXiv: 1707.07606 [hep-ph].
- [106] John C. Collins, Davison E. Soper, and George Sterman. “Soft gluons and factorization”. In: *Nuclear Physics B* 308.4 (1988), pp. 833–856.
- [107] Xiangdong Ji, Jian-Ping Ma, and Feng Yuan. “QCD factorization for spin-dependent cross sections in DIS and Drell–Yan processes at low transverse momentum”. In: *Physics Letters B* 597.3–4 (2004), 299–308.
- [108] John Collins. “New definition of TMD parton densities”. In: *International Journal of Modern Physics: Conference Series* 04 (2011), 85–96.

- [109] Miguel G. Echevarria, Ignazio Scimemi, and Alexey Vladimirov. “Universal transverse momentum dependent soft function at NNLO”. In: *Physical Review D* 93.5 (2016).
- [110] G.P. Korchemsky and A.V. Radyushkin. “Renormalization of the Wilson loops beyond the leading order”. In: *Nuclear Physics B* 283 (1987), pp. 342–364.
- [111] I.A. Korchemskaya and G.P. Korchemsky. “On light-like Wilson loops”. In: *Physics Letters B* 287.1 (1992), pp. 169–175.
- [112] John Collins and Ted Rogers. “Equality of two definitions for transverse momentum dependent parton distribution functions”. In: *Phys. Rev. D* 87 (3 2013), p. 034018.
- [113] Miguel G. Echevarría, Ahmad Idilbi, and Ignazio Scimemi. “Soft and collinear factorization and transverse momentum dependent parton distribution functions”. In: *Physics Letters B* 726.4 (2013), pp. 795–801.
- [114] John P. Ralston and Davidson E. Soper. “Production of dimuons from high-energy polarized proton-proton collisions”. In: *Nuclear Physics B* 152.1 (1979), pp. 109–124.
- [115] R. D. Tangerman and P. J. Mulders. “Intrinsic transverse momentum and the polarized Drell-Yan process”. In: *Phys. Rev. D* 51 (7 1995), pp. 3357–3372.
- [116] P.J Mulders and R.D Tangerman. “The complete tree-level result up to order $1/Q$ for polarized deep-inelastic lepton production”. In: *Nuclear Physics B* 461.1 (1996), pp. 197–237.
- [117] K. Goeke, A. Metz, and M. Schlegel. “Parameterization of the quark-quark correlator of a spin-1/2 hadron”. In: *Physics Letters B* 618.1 (2005), pp. 90–96.
- [118] Dennis Sivers. “Single-spin production asymmetries from the hard scattering of pointlike constituents”. In: *Phys. Rev. D* 41 (1 1990), pp. 83–90.
- [119] J.C. Collins et al. “Sivers effect in semi-inclusive deeply inelastic scattering and Drell-Yan”. In: *Transversity 2005*. World Scientific, 2006, 212–219.
- [120] J. C. Collins et al. “Sivers effect in semi-inclusive deeply inelastic scattering”. In: *Phys. Rev. D* 73 (1 2006), p. 014021.
- [121] A.V. Efremov et al. “Sivers effect in semi-inclusive DIS and in the Drell-Yan process”. In: *Physics Letters B* 612.3 (2005), pp. 233–244.

- [122] Renaud Boussarie et al. “TMD Handbook”. In: (2023). arXiv: 2304.03302 [hep-ph].
- [123] Felix Rein et al. “Sivers, Boer-Mulders and worm-gear distributions at next-to-leading order”. In: *Journal of High Energy Physics* 2023.1 (2023).
- [124] Miguel G. Echevarria et al. “QCD evolution of the Sivers asymmetry”. In: *Physical Review D* 89.7 (2014).
- [125] Peng Sun et al. “Universal Non-perturbative Functions for SIDIS and Drell-Yan Processes”. In: *International Journal of Modern Physics A* 33 (2014).
- [126] Valerio Bertone, Ignazio Scimemi, and Alexey Vladimirov. “Extraction of unpolarized quark transverse momentum dependent parton distributions from Drell-Yan/Z-boson production”. In: *Journal of High Energy Physics* 2019.6 (2019).
- [127] Alessandro Bacchetta et al. “Transverse-momentum-dependent parton distributions up to N³LL from Drell-Yan data”. In: *Journal of High Energy Physics* 2020.7 (2020).
- [128] Ignazio Scimemi and Alexey Vladimirov. “Non-perturbative structure of semi-inclusive deep-inelastic and Drell-Yan scattering at small transverse momentum”. In: *Journal of High Energy Physics* 2020.6 (2020).
- [129] Valentin Moos et al. “Extraction of unpolarized transverse momentum distributions from the fit of Drell-Yan data at N⁴LL”. In: *JHEP* 05 (2024), p. 036. arXiv: 2305.07473 [hep-ph].
- [130] Matthias Burkardt and Brian Hannafous. “Are all Boer–Mulders functions alike?” In: *Physics Letters B* 658.4 (2008), 130–137.
- [131] D. Brömmel et al. “Spin Structure of the Pion”. In: *Physical Review Letters* 101.12 (2008).
- [132] Sara Piloneta and Alexey Vladimirov. *Angular distributions of Drell-Yan leptons in the TMD factorization approach*. 2024. arXiv: 2407.06277 [hep-ph].
- [133] Xiangdong Ji, Jian-Hui Zhang, and Yong Zhao. “Renormalization in Large Momentum Effective Theory of Parton Physics”. In: *Physical Review Letters* 120.11 (2018).
- [134] Tomomi Ishikawa et al. “Renormalizability of quasiparton distribution functions”. In: *Physical Review D* 96.9 (2017).

- [135] Jeremy Green, Karl Jansen, and Fernanda Steffens. “Nonperturbative Renormalization of Nonlocal Quark Bilinears for Parton Quasidistribution Functions on the Lattice Using an Auxiliary Field”. In: *Physical Review Letters* 121.2 (2018).
- [136] Phiala Shanahan, Michael L. Wagman, and Yong Zhao. “Nonperturbative renormalization of staple-shaped Wilson line operators in lattice QCD”. In: *Physical Review D* 101.7 (2020).
- [137] Markus A. Ebert, Iain W. Stewart, and Yong Zhao. “Renormalization and matching for the Collins-Soper kernel from lattice QCD”. In: *Journal of High Energy Physics* 2020.3 (2020).
- [138] Kuan Zhang et al. “Renormalization of Transverse-Momentum-Dependent Parton Distribution on the Lattice”. In: *Physical Review Letters* 129.8 (2022).
- [139] Xiangdong Ji et al. “Soft factor subtraction and transverse momentum dependent parton distributions on the lattice”. In: *Physical Review D* 91.7 (2015).
- [140] Xiangdong Ji, Yizhuang Liu, and Yu-Sheng Liu. “Transverse-momentum-dependent parton distribution functions from large-momentum effective theory”. In: *Physics Letters B* 811 (2020), p. 135946.
- [141] Adam F. Falk et al. “Heavy meson form factors from QCD”. In: *Nuclear Physics B* 343.1 (1990), pp. 1–13.
- [142] Xiangdong Ji and M.J. Musolf. “Sub-leading logarithmic mass-dependence in heavy-meson form-factors”. In: *Physics Letters B* 257.3 (1991), pp. 409–413.
- [143] V. M. Braun, K. G. Chetyrkin, and B. A. Kniehl. “Renormalization of parton quasi-distributions beyond the leading order: spacelike vs. timelike”. In: *Journal of High Energy Physics* 2020.7 (2020).
- [144] Andrey Grozin. “Anomalous dimension of the heavy-light quark current in HQET up to four loops”. In: *JHEP* 02 (2024), p. 198. arXiv: 2311.09894 [hep-ph].
- [145] P.A. Zyla et al. “Review of Particle Physics”. In: *PTEP* 2020.8 (2020), p. 083C01.
- [146] Markus A. Ebert, Iain W. Stewart, and Yong Zhao. “Determining the nonperturbative Collins-Soper kernel from lattice QCD”. In: *Physical Review D* 99.3 (2019).
- [147] Hai-Tao Shu et al. “Universality of the Collins-Soper kernel in lattice calculations”. In: *Phys. Rev. D* 108 (7 2023), p. 074519.

- [148] Ignazio Scimemi and Alexey Vladimirov. “Non-perturbative structure of semi-inclusive deep-inelastic and Drell-Yan scattering at small transverse momentum”. In: *Journal of High Energy Physics* 2020.6 (2020).
- [149] Alessandro Bacchetta et al. “Unpolarized transverse momentum distributions from a global fit of Drell-Yan and semi-inclusive deep-inelastic scattering data”. In: *Journal of High Energy Physics* 2022.10 (2022).
- [150] Xiangdong Ji, Yizhuang Liu, and Yu-Sheng Liu. “TMD soft function from large-momentum effective theory”. In: *Nuclear Physics B* 955 (2020), p. 115054.
- [151] Markus A. Ebert, Iain W. Stewart, and Yong Zhao. “Towards quasi-transverse momentum dependent PDFs computable on the lattice”. In: *Journal of High Energy Physics* 2019.9 (2019).
- [152] Xiangdong Ji et al. “Transverse momentum dependent parton quasidistributions”. In: *Physical Review D* 99.11 (2019).
- [153] Robert G. Edwards and Bálint Joó. “The Chroma Software System for Lattice QCD”. In: *Nuclear Physics B - Proceedings Supplements* 140 (2005), 832–834.
- [154] Jiunn-Wei Chen and Xiangdong Ji. “Is the Sullivan process compatible with QCD chiral dynamics?” In: *Physics Letters B* 523.1–2 (2001), 107–110.
- [155] Gunnar S. Bali et al. “Light-cone distribution amplitudes of octet baryons from lattice QCD”. In: *The European Physical Journal A* 55.7 (2019).
- [156] Filippo Delcarro et al. “Extraction of Transverse Momentum Distributions from semi-inclusive DIS and Drell-Yan data.” In: 2018, p. 219.

Acknowledgements

There are many people I want to thank for helping me on my way to writing this thesis. I am especially grateful to my supervisor Andreas Schäfer for offering helpful guidance and advice throughout all the years of my PhD and always having an open ear for my questions and concerns. I want to thank Christoph Lehner as the second referee of this thesis and the other members of the PhD committee, John Lupton and Juan Diego Urbina, for their time and efforts. My gratitude also goes to Lingquan Ma, Xiangdong Ji, Yushan Su, Peng Sun, Xiaonu Xiong, Yi-Bo Yang, Fei Yao, Jianhui Zhang, Qi-An Zhang and the other members of LPC for the close collaboration. I thank Hai-Tao Shu for providing the data for the Collins-Soper kernel and intrinsic soft function and Valentin Moos, Maximilian Schlemmer and Alexey Vladimirov for fruitful discussions that improved my understanding of TMDPDFs. I give my thanks to Daniel Reitering for helping to cross-check the implementation of RGR. I also want to thank Gunnar Bali, Sara Collins and Wolfgang Söldner for helpful discussions throughout the years. My thanks go to Fabian Hutzler, Andreas Rabenstein, Thomas Wurm, Simon Bürger, Daniel Jenkins, Lorenzo Barca and Marius Löffler for their support of my lattice QCD projects even before my PhD thesis. Thanks also to Monika Maschek and Heidi Decock for their help with paperwork and all sorts of concerns. I want to thank Sebastian Spiegel, Andreas Hackl, Daniel Knüttel, Valentin Moos and Tobias Sizmann for many enjoyable lunch and coffee breaks. Last but not least, I would like to thank my parents, friends and my boyfriend for supporting me during stressful times by providing warm meals, snacks, hugs, and always being there for me.